Emanuele Murgano

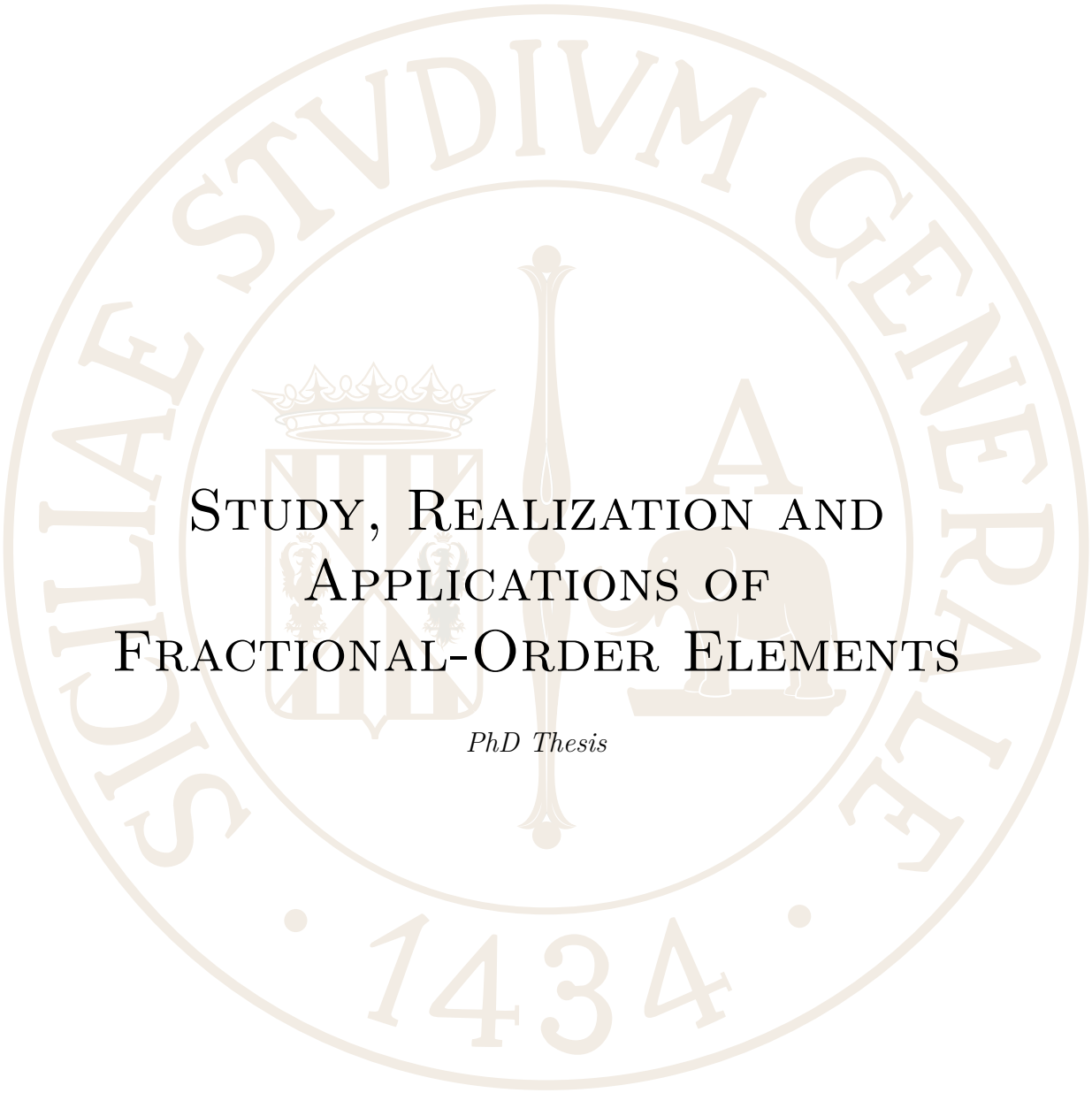

Study, Realization and Applications of Fractional-Order Elements

PhD Thesis

UNIVERSITY OF CATANIA

October 2021

University of Catania

Department of Electrical Electronics and Computer Science Engineering

Systems, Energy, Computer and Telecommunications Engineering - XXXIV Cycle

PhD Thesis

Study, Realization and Applications of Fractional-Order Elements

---

Author
Emanuele Murgano

Supervisor
Prof. R. Caponetto
PhD Coordinator
Prof. P. Arena

ACADEMIC YEAR 2020/2021

UNIVERSITY OF CATANIA

Department of Electrical Electronics and Computer Science Engineering

Systems, Energy, Computer and Telecommunications Engineering - XXXIV Cycle

Study, Realization and Applications of Fractional-Order Elements

by Emanuele Murgano

ABSTRACT

Nowadays, Fractional Calculus is widely used for describing and modeling complex behaviours such as viscoelasticity, thermal systems, economy and finance, and so on, thanks to its extra degree of freedoms and long memory effects. Additionally, one of its application that involves several researchers is related to the electronics and automatic control fields. The possibility of having more degree of freedoms, given by the non-integer-order operator, leads to achieve better and more robust performances compared to the traditional compensators. These controllers can be implemented both in a digital or in an analog way. Related to this latter class, it is required that such electronics components must have a different behaviour from the common standard electronics. Researchers are developing several technologies to build components whose behaviour is intrinsically of fractional order and such devices are defined as "Fractional-Order Elements".

The proposed work acts in the described framework: the possibility of realizing new electronics components is investigated with the aim of employing them for the development of fractional-order robust controllers. More specifically, two different technologies have been deeply investigated for obtaining fractional-order capacitors: the first one is based on diffusing Carbon Black particles inside a polymeric matrix, while the second approach on employing Bacterial Cellulose-based compounds as dielectrics in a parallel-plates configuration. The modeling of the physical phenomena that occur inside the components, the evidence of their fractional-order nature and their application are provided and analyzed in details.

Contents

List of Figures

List of Tables

List of Abbreviations

FOE	**F**ractional **O**rder **E**lement
IO	**I**nteger **O**rder
FC	**F**ractional **C**alculus
FO	**F**ractional **O**rder
FOS	**F**ractional **O**rder **S**ystem
RL	**R**iemann **L**iouville
CP	**Ca**puto
GL	**G**ründwald **L**etnikov
LTI	**L**inear **T**ime **I**nvariant
MIMO	**M**ulti **I**nput **M**ulti **O**utput
SISO	**S**ingle **I**nput **S**ingle **O**utput
BIBO	**B**ounded **I**nput **B**ounded **O**utput
LCM	**L**east **C**ommon **M**ultiplier
PID	**P**roportional **I**ntegral **D**erivative
CRONE	**C**ommande **R**obuste d'**O**rdre **N**on **E**ntier
TF	**T**ransfer **F**unction
PD	**P**roportional **D**erivative
PI	**P**roportional **I**ntegral
CPE	**C**onstant **P**hase **E**lement
EIS	**E**lectrochemical **I**mpedance **S**pectroscopy
DLC	**D**ouble **L**ayer **C**apacitor
CMOS	**C**omplementary **M**etal-**O**xide **S**emiconductor
OTA	**O**perational **T**ransconductance **A**mplifier
MOS	**M**etal-**O**xide **S**emiconductor
PMMA	**P**oly **M**ethyl **M**eth**A**crylate
CB	**C**arbon **B**lack
CNT	**C**arbon **N**ano-**T**ube
MWCNT	**M**ulti-**W**alled **C**arbon **N**ano-**T**ube
PDMS	**P**oly**D**i**M**ethyl**S**iloxane
CT	**C**uring **T**emperature
SP	**S**tabilization **P**eriod
GA	**G**enetic **A**lgorithm
CF	**C**ost **F**unction

IFBW	**I**ntermediate **F**requency **B**and **W**idth
EECM	**E**quivalent **E**lectric **C**ircuit **M**odel
FOLC	**F**ractional **O**rder **L**ead **C**ompensator
BC	**B**acterial **C**ellulose
EAP	**E**lectro **A**ctive **P**olymer
IL	**I**onic **L**iquid
SEM	**S**canning **E**lectrone **M**icroscope
XPS	**X**-ray **P**hotoelectron **S**pectroscopy
EMIM	1-**E**thyl-3-**M**ethyl**IM**idazolium
TFMS	**T**ri**F**luoro**M**ethane**S**ulfonate
NRMSE	**N**ormalized **R**oot **M**ean **S**quared **E**rror

List of Symbols

$\mathbb{N}$	natural set number	
$\mathbb{N}_0$	natural set number without 0	
$\mathbb{Z}+$	positive integer set number	
$\mathbb{Q}$	rational set number	
$\mathbb{R}$	real set number	
n	natural number	
j	imaginary unit	
s	Laplace complex variable	
M_G	gain margin	[dB]
M_φ	phase margin	[deg]
S_{max}	maximum acceptable sensitivity function value	
T_{max}	maximum acceptable noise rejection function value	
C_α	fractional capacitance	$[\mathrm{F/s^{1-\alpha}}]$
C_i	integer capacitance	[F]
C_n	nominal capacitance	[F]
$\mathcal{J}$	cost function value	
e_M	magnitude error between real and simulated impedance	[dB]
e_φ	phase angle error between real and simulated impedance	[deg]
$\mathcal{F}$	goodness of fit	
$\mathcal{F}_M$	magnitude goodness of fit	
$\mathcal{F}_\varphi$	phase angle goodness of fit	
α	real number	
λ	pseudo-rational variable	
ω	angular pulsation	$[\mathrm{rad\,s^{-1}}]$
ω_c	gain crossover pulsation	$[\mathrm{rad\,s^{-1}}]$
ω_π	phase margin pulsation	$[\mathrm{rad\,s^{-1}}]$
ω_s	maximum pulsation band	$[\mathrm{rad\,s^{-1}}]$
ω_t	minimum noise rejection pulsation	$[\mathrm{rad\,s^{-1}}]$
ω_r	resonance pulsation	$[\mathrm{rad\,s^{-1}}]$
ε	dielectric constant	$[\mathrm{F\,m^{-1}}]$
ε_0	vacuum dielectric constant	$[\mathrm{F\,m^{-1}}]$
ε_r	relative dielectric constant	$[\mathrm{F\,m^{-1}}]$
$\varepsilon_{r,w}$	water relative dielectric constant	$[\mathrm{F\,m^{-1}}]$

$\varepsilon_{r,c}$	cellulose relative dielectric constant	$[\mathrm{F\,m^{-1}}]$
$\varepsilon_{r,BC}$	Bacterial Cellulose relative dielectric constant	$[\mathrm{F\,m^{-1}}]$
σ_M	magnitude standard deviation between real and simulated impedance	[dB]
σ_φ	phase standard deviation between real and simulated impedance	[deg]
$\Gamma(\cdot)$	Euler Gamma function	
${}_a\mathcal{D}_t^\alpha(\cdot)$	integral-differential operator of α-order in the interval $[a;t]$	
$\mathcal{D}^\alpha(\cdot)$	integral-differential operator of α-order	
$\angle(\cdot)$	angle function	
$\Re(\cdot)$	real part function	
$\Im(\cdot)$	imaginary part function	
$\mathcal{L}(\cdot)$	Laplace transform	
$\mathcal{L}^{-1}(\cdot)$	inverse Laplace transform	
$\mathcal{E}_\alpha(\cdot)$	Mittag-Leffler function in one parameter	
$\mathcal{E}_{\alpha,\alpha}(\cdot)$	Mittag-Leffler function in two parameters	
$S(\cdot)$	sensitivity function	
$T(\cdot)$	complementary sensitivity function	

Introduction

In the 1695, de L'Hopital asked to Leibniz what would happen if the n-derivative of a function was of non-integer order, like $n = 1/2$, instead of an integer value. The Leibniz's answer was the following: "[...] This is an apparent paradox from which, one day, useful consequences will be drawn [...]".
It might say that the Fractional Calculus was born in that century.
Generally, n-derivative or n-integral calculus are commonly based on integer numbers, i.e., $n \in \mathbb{N}_0$, but what do happen if n is not integer, i.e., $n \in \mathbb{R}$? Taking into account the standard algebraic set theory, the Integer Calculus can be considered as a particular case of the fractional one. Since decades, Fractional Calculus is widely used in several and different fields: model and control of natural physical systems such as the human brain and its nervous system, diffusive phenomena in chemical reactions, economy, finance and so on. Furthermore, one of its most proficient research field is related to the realization of the so-called "Fractional-Order Elements"(FOEs), i.e., components whose behaviour can be described only by means of fractional-order differential equations. Their realization gives the chance to exploit more parameters and, hence, more degrees of freedom for achieving better performances.
With this aim, the first proposed technology makes use of Carbon Black-based polymeric dielectrics in order to obtain an intrinsically capacitive fractional-order behaviour.

Concurrently with the aforementioned control benefits, it is also fundamental to analyze the drawbacks of such a technological progress and demand for new electronics components. Several studies have demonstrated that more than one thousand of electronics wastes (e-wastes) are produced every year. They are difficult to dispose and this will lead to severe damages for the natural ecosystem and human health. For such reasons, a new research field is becoming more and more relevant for overcoming this issue: green electronics. Natural compounds are studied and exploited with the aim to obtain new sensors or devices easy to dispose and with good performances compared to the already available electronics. Taking into account these aspects, the second technological procedures that has been investigated in this work employs a natural compound, the Bacterial Cellulose, as possible main material for a new and greener class of electronics.

In details, the proposed work is divided as follows:

- **Chapter 1: Fractional Calculus**
  Fractional Calculus is presented and its main properties are defined. Fractional-Order lead compensators will be also presented, showing their advantages compared to the common integer-order counterpart;

- **Chapter 2: Fractional-Order Elements**
  The state of art for FOEs will be drawn and explanation of the physical phenomena which occur inside them will be provided;

- **Chapter 3: Carbon Black-based FOEs**
  The electronics components realized by means of Carbon Black are presented in this chapter. The overall technological procedure will be described in details and the realized components will be tested in real applications, starting from simple electronic circuits to a real implementation of fractional-order lead compensator;

- **Chapter 4: Bacterial Cellulose-based FOEs**
  Bacterial Cellulose is used as dielectrics for a new class of electronics devices. Evidence of its fractional-order nature is provided and its behaviour is modelled by means of Equivalent Electric Circuit Model. Furthermore, its frequency response is investigated by changing its molecular structures by means of Ionic Liquids;

- **Chapter 5: Conclusions**
  In the final chapter, conclusions and possible future developments are depicted.

Chapter 1

Fractional Calculus

The Integer Calculus, established as *golden standard* method in every scientific field since centuries, allows to evaluate the $n-th$-order derivative (or integral) of a continuous function. Mathematical rules have been defined for computing more easily the derivative of a polynomial functions, or the integral of trigonometric ones. Obviously, these formulas and, more in general, the Integer Calculus takes into account derivatives (or integrals) of Integer-Order (IO), i.e., $n \in \mathbb{N}_0$: it is easy to think at a first-order derivative of a function or a second-order integral. Unfortunately, such mathematical concepts become more complex if the assumption $n \in \mathbb{R}$ holds. In this scenario, the Fractional Calculus (FC) can be defined as a new mathematical framework able to deal with a generic (and non integer) order of a derivative or integral. Besides, from the algebraic set laws, it is well known that $\mathbb{N}_0 \subset \mathbb{R}$: from this assumption, and as it will be demonstrated in the next sections, it can be said that the Fractional Calculus includes and generalizes the Integer Calculus.

The chapter will be organized as follows: firstly, a formal definition of the Fractional-Order (FO) integrodifferential operator will be given, describing this framework by a mathematical point-of-view. Subsequently, the main properties of Fractional-Order Systems (FOSs), such as stability, system representation and step response, will be presented and, in conclusion, FO-controllers will be discussed.

1.1 Fractional-order integrodifferential operator

As already said, the FC framework allows to compute the n-th-order derivative (or integral) of a function, with $n \in \mathbb{R}$. To easily distinguish between an integer-order and a fractional-order derivative, the n variable will represent an integer number, i.e., $n \in \mathbb{N}$, while the α variable will represent a real number, i.e., $\alpha \in \mathbb{R}$ and it will be defined as *fractional-order*.

The operator ${}_a\mathcal{D}_t^\alpha$, where $a, t \in \mathbb{R}$ represent its operation limits, defines in a compact way the possibility of computing the fractional-order derivative (if

$\alpha > 0$) or integral (if $\alpha < 0$) of its argument. It can be noticed that if $\alpha = \pm 1$ the canonical first-order derivative or integral are evaluated, respectively.

Formally, the fractional-order differential operator ${}_a\mathcal{D}_t^\alpha$ is defined as follows:

$$ {}_a\mathcal{D}_t^\alpha = \begin{cases} \dfrac{d^\alpha}{dt^\alpha} & : \quad \alpha > 0 \\ 1 & : \quad \alpha = 0 \\ \int_a^t (d\tau)^{-\alpha} & : \quad \alpha < 0 \end{cases} \tag{1.1} $$

The operator in (1.1) has been defined in several ways from different scientists [1]–[3]. According to the performed numerical analysis, i.e., for continuous-time or discrete-time domain, the operator can be properly formulated. For the continuous-time domain analysis, the two main definitions used are the Riemann-Liouville *(RL)* and the Caputo *(CP)* ones, while, for the discrete-time case, the most used definition is the Gründwald-Letnikov *(GL)* one.
Given a time-varying function $f(t)$, the *RL* and *CP* definitions can be computed as follows:

$$ \{{}_a\mathcal{D}_t^\alpha\}_{RL} = \frac{1}{\Gamma(n-\alpha)} \frac{d^n}{dt^n} \int_a^t \frac{f(\tau)}{(t-\tau)^{\alpha-n+1}} d\tau \tag{1.2} $$

and,

$$ \{{}_a\mathcal{D}_t^\alpha\}_{CP} = \frac{1}{\Gamma(n-\alpha)} \int_a^t \frac{f^{(n)}(\tau)}{(t-\tau)^{\alpha-n+1}} d\tau. \tag{1.3} $$

where $n \in \mathbb{N} : n-1 < \alpha \leq n$ and $\Gamma(\cdot)$ is the *Euler Gamma* function [4]. $\Gamma(\cdot)$ extends the concept of factorial number for the integer values, i.e., if $n \in \mathbb{N}$ then $\Gamma(n) = (n-1)!$. More in general, given $\alpha \in \mathbb{R}$, the Gamma function is defined as:

$$ \Gamma(\alpha) = \int_0^{+\infty} e^{-u} u^{\alpha-1} du. \tag{1.4} $$

Taking into account the consideration made for the Gamma function, a preliminary result can be detected: (1.2) is similar to the repeated integral formula established by Cauchy [5], if $\alpha \in \mathbb{N}$. This simple consideration demonstrates that FC can be thought as a generalization of the Integer Calculus.

The *GL* definition is provided by the following equation:

$$ \{{}_a\mathcal{D}_t^\alpha\}_{GL} = \lim_{h \to 0} h^{-r} \sum_{j=0}^{\left[\frac{t-a}{h}\right]} (-1)^j \binom{\alpha}{j} f(t-jh) \tag{1.5} $$

where $[\cdot]$ evaluates the integer part of its argument. Also in this case, if the well-known definition of integer-order derivative is computed and iteratively derived α-times (with $\alpha \in \mathbb{N}$), the same definition of (1.5) is obtained [6].

For each definition, it can be observed that the fractional-order operator ${}_a\mathcal{D}_t^\alpha$ differs from its integer-order counterpart because it is a non-local operator with infinity memory, i.e., the future states depends on all the past state, [6], [7].

Looking at the *RL* and *CP* definitions, even if they appear quite similar, some important differences arise. As it will be demonstrated in the following section, the initial conditions for the *CP* definition still maintain a physical meaning, while this does not occur with the *RL* formulation. Furthermore, most of the derivation rules (holding for integer-order derivatives) can be extended to the fractional-order case. However, the following exceptions, respectively called *Leibniz* and *Chain* rules, must be underlined in order to avoid mistakes.

$$\frac{d^\alpha(f(t)g(t)}{dt^\alpha} \neq \frac{d^\alpha f(t)}{dt^\alpha}g(t) + \frac{d^\alpha g(t)}{dt^\alpha}f(t)$$
$$\frac{d^\alpha(f(g(t))}{dt^\alpha} \neq \frac{d^\alpha f}{dg^\alpha} \cdot \frac{d^\alpha g(t)}{dt^\alpha}$$

1.1.1 Laplace transform

Considering $\alpha \in \mathbb{R}$, $n \in \mathbb{N} : \; n-1 < \alpha < n$ and a time-varying function $f(t)$, the Laplace transform for the *RL* [1] is defined as:

$$\mathcal{L}\left\{\frac{d^\alpha}{dt^\alpha}_{RL} f(t)\right\} = s^\alpha \mathcal{L}\{f(t)\} - \sum_{k=0}^{n-1} s^k \left[\frac{d^{\alpha-1-k}}{dt^{\alpha-1-k}} f(t)\right]_{t=0} \tag{1.6}$$

while for the *CP* definition, the Laplace transform can be evaluates as:

$$\mathcal{L}\left\{\frac{d^\alpha}{dt^\alpha}_{CP} f(t)\right\} = s^\alpha \mathcal{L}\{f(t)\} - \sum_{k=0}^{n-1} s^{\alpha-k-1} f^{(k)}(0) \tag{1.7}$$

Analysing (1.6) and (1.7), it can be noticed, as stated previously, that only the Caputo definition still maintains a physical meaning for the system initial conditions. For such a reason, generally, the Caputo definition is the most used operator for continuous-time system.
Equations (1.6) and (1.7) can be easily simplified if all the $n-1$ derivatives are equal to zero. This leads to a simpler definition, represented by (1.8):

$$\mathcal{L}\left\{\frac{d^\alpha}{dt^\alpha} f(t)\right\} = s^\alpha \mathcal{L}\{f(t)\}. \tag{1.8}$$

This last expression allows to evaluate the inverse Laplace transform of elementary functions, like the fractional-order integrator $1/s^\alpha$.
Applying the *CP* operator, the impulse response of a non-integer-order integrator is given by the following equation,

$$\mathcal{L}\left\{\frac{t^{\alpha-1}}{\Gamma(\alpha)}\right\} = \frac{1}{s^\alpha}; \quad \mathcal{L}^{-1}\left\{\frac{1}{s^\alpha}\right\} = \frac{t^{\alpha-1}}{\Gamma(\alpha)} \tag{1.9}$$

if the following assumptions are true:

1. $f(t) = \delta(t)$, where $\delta(t)$ is the Dirac impulse;
2. $\alpha = -\alpha$, i.e., the opposite of α is evaluated.

Considering the frequency translation operation, represented by $\mathcal{L}^{-1}\{F(s+a)\} = e^{-at}\mathcal{L}^{-1}\{F(s)\}$, the Laplace Transform of (1.9) can be applied:

$$\mathcal{L}^{-1}\left\{\frac{1}{(s+a)^{\alpha}}\right\} = \frac{t^{\alpha-1}e^{-at}}{\Gamma(\alpha)}. \tag{1.10}$$

The result of (1.10) gives the opportunity to evaluate the impulse response of a generic transfer function $F(s) = 1/(s+a)^{\alpha}$ and to derive a time domain representation with a finite number of terms.

1.2 General proprieties

In this section the following general proprieties and definitions of a FOS will be analysed.[1]

1. System representations;
2. Bode diagram;
3. Time domain response analysis;
4. Stability;

1.2.1 System representations

In general, a LTI dynamical system can be divided as follows:

- Integer
- Non integer
  - i. Commensurate
    - (a) Rational
    - (b) Irrational
  - ii. Non-commensurate

The equations for a generical MIMO dynamical fractional-order system can be written as:

$$H(\mathcal{D}^{\alpha_0\alpha_1\ldots\alpha_m})(y_1, y_2, ..., y_l) = G(\mathcal{D}^{\beta_0\beta_1\ldots\beta_n})(u_1, u_2, ..., u_k). \tag{1.11}$$

where y_i, u_i are function of time and $H(\cdot)$, $G(\cdot)$ are the fractional dynamical laws that represent, respectively, the evolution of outputs and inputs.

Frequency domain

Considering a LTI SISO fractional-order system, (1.11) is reduced to:

$$H(\mathcal{D}^{\alpha_0\alpha_1\ldots\alpha_n})y(t) = G(\mathcal{D}^{\beta_0\beta_1\ldots\beta_m})u(t) \tag{1.12}$$

[1] If not explicitally expressed, mathematical backgrounds are reported from [6] and [7].

where $H(\mathcal{D}^{\alpha_0\alpha_1\dots\alpha_n}) = \sum_{k=0}^{n} a_k \mathcal{D}^{\alpha_k}$ and $G(\mathcal{D}^{\beta_0\beta_1\dots\beta_m}) = \sum_{k=0}^{m} b_k \mathcal{D}^{\beta_k}$ with a_k, $b_k \in \mathbb{R}$. Rearrangement of (1.12) gives:

$$\begin{aligned} a_n \mathcal{D}^{\alpha_n} y(t) + a_{n-1} \mathcal{D}^{\alpha_{n-1}} y(t) + \dots + a_0 \mathcal{D}^{\alpha_0} y(t) = \\ b_m D^{\beta_m} u(t) + b_{m-1} D^{\beta_{m-1}} u(t) + \dots + b_0 D^{\beta_0} u(t) \end{aligned} \tag{1.13}$$

From (1.13), if α_k, $\beta_k = k\alpha$, $\alpha \in \mathbb{R}+$, i.e., if all the derivatives are integer multiple of a common base α, the system will be defined as *commensurate order*. In particular, if $\alpha = 1/q$ with $q \in \mathbb{Z}+$, the system will be defined as *rational-order*.

Under the assumption that all the derivatives have zero initial conditions, the Laplace transform can be applied to (1.13) and the related transfer function definition is obtained as follows:

$$G(s) = \frac{Y(s)}{U(s)} = \frac{b_m s^{\beta_m} + b_{m-1} s^{\beta_{m-1}} + \dots + b_0 s^{\beta_0}}{a_n s^{\alpha_n} + a_{n-1} s^{\alpha_{n-1}} + \dots + a_0 s^{\alpha_0}}. \tag{1.14}$$

Evaluating (1.13), as already noticed by the fractional-order derivative definitions, it can be observed that, except for the case $\alpha \in \mathbb{Z}+$, FOSs have *infinity memory*. Obviously, if the system is strictly proper ($n > m$), (1.14) can be expressed as the sum of partial fractions considering the solutions of the denominator of the transfer function (exactly like the integer-order case). The case of commensurate-order systems is focused on and its transfer function is reported as follows:

$$G(s) = \frac{\sum_{k=0}^{m} b_k s^{\alpha^k}}{\sum_{k=0}^{n} a_k s^{\alpha^k}}. \tag{1.15}$$

A pseudo-rational function from (1.15) can be obtained simply putting $\lambda = s^{\alpha}$:

$$H(\lambda) = \frac{\sum_{k=0}^{m} b_k \lambda^k}{\sum_{k=0}^{n} a_k \lambda^k}. \tag{1.16}$$

State-space domain

Considering a LTI MIMO fractional-order system, a state-space realization can be computed as follows,

$$\mathcal{D}^{\underline{\alpha}}\mathbf{x} = \mathbf{A}\mathbf{x} + \mathbf{B}\mathbf{u} \tag{1.17}$$

$$\mathbf{y} = \mathbf{C}\mathbf{x} + \mathbf{D}\mathbf{u} \tag{1.18}$$

where $\underline{\alpha} = [\alpha_1, \alpha_2, ..., \alpha_n]$, $\mathbf{A} \in \mathbb{R}^{n\times n}$ is the state matrix, $\mathbf{x} \in \mathbb{R}^{n\times 1}$ is the space state variables vector, $\mathbf{B} \in \mathbb{R}^{n\times l}$ is the input matrix, $\mathbf{u} \in \mathbb{R}^{l}$ is the input vector, $\mathbf{y} \in \mathbb{R}^{p\times 1}$ is the output variables vector, $\mathbf{C} \in \mathbb{R}^{p\times n}$ is the output matrix and $\mathbf{D} \in \mathbb{R}^{p\times l}$ is the direct transition matrix. Considering that $\underline{\alpha}$ is a vector, each state variable x_i is differentiated with the i-th element of $\underline{\alpha}$. If $\alpha_i = \alpha$, $\forall i \in [1; n]$ the space-state equations can be rearranged as:

$$\mathcal{D}^{\alpha}\mathbf{x} = \mathbf{A}\mathbf{x} + \mathbf{B}\mathbf{u} \tag{1.19}$$

where now all the x_i variables are differentiated by α, supposing $0 < \alpha \leq 1$. From the space-state equations, the transfer function can be evaluated by applying the Laplace transform to them and evaluating the Caputo definition (1.3):

$$s^{\alpha}\mathbf{X}(s) - s^{\alpha-1}\mathbf{x}(0) = \mathbf{A}\mathbf{X}(s) + \mathbf{B}\mathbf{U}(s) \rightarrow$$

$$\mathbf{X}(s) = (s^{\alpha}\mathbf{I} - \mathbf{a})^{-1}\mathbf{B}\mathbf{U}(s) + (s^{\alpha}\mathbf{I} - \mathbf{a})^{-1}s^{\alpha-1}\mathbf{x}(0), \tag{1.20}$$

$$\mathbf{Y}(s) = \mathbf{C}\mathbf{X}(s) + \mathbf{D}\mathbf{U}(s). \tag{1.21}$$

The *CP* definition is essential if the initial conditions have to be expressed directly as state values at $t = 0$. However, if the initial condition at $t = t_0$ is $x(t_0) = x_0$, the fractional-order operator looses its properties of non-locality and infinite memory. Therefore, some adjustments and considerations have to be done for the initial conditions of *CP* definition in the state-space representation. See [8] for further details.

Supposing to have zero initial conditions, the above equation becomes:

$$\mathbf{X}(s) = (s^{\alpha}\mathbf{I} - \mathbf{a})^{-1}\mathbf{B}\mathbf{U}(s) \tag{1.22}$$

The transfer function can be evaluated as: $\mathbf{G}(s) = \mathbf{Y}(s)/\mathbf{U}(s) \rightarrow \mathbf{Y}(s) = \mathbf{G}(s)\mathbf{U}(s)$, so:

$$\mathbf{G}(s) = \mathbf{C}(s^{\alpha}\mathbf{I} - \mathbf{A})^{-1}\mathbf{B} + \mathbf{D}. \tag{1.23}$$

Analysing (1.23), as a consequence of $\alpha_i = \alpha$, the system becomes a commensurate-order one.

1.2.2 Bode Diagram

The Bode Diagram is analysed due to its importance in systems and control theory. Considering a generic function $F(s) = k/(\tau s + 1)^{\alpha}$, with $\tau = 1/p$ and

putting $s = j\omega$, the frequency response can be evaluated as follows:

$$F(j\omega) = \left[\frac{k^{1/\alpha}}{(j\omega/p+1)}\right]^{\alpha} = \left[\left|\frac{k^{1/\alpha}}{(j\omega/p+1)}\right| e^{j\angle\left[\frac{k^{1/\alpha}}{(j\omega/p+1)}\right]}\right]^{\alpha} =$$

$$= \left|\frac{k^{1/\alpha}}{(j\omega/p+1)}\right|^{\alpha} e^{j\omega\angle\left[\frac{k^{1/\alpha}}{(j\omega/p+1)}\right]} \tag{1.24}$$

where $\angle(\cdot)$ evaluates the phase angle of its argument. From (1.24), the magnitude response, in dB, can be evaluated:

$$|F(j\omega)|_{dB} = 20\log_{10}\left[\frac{k^{1/\alpha}}{\sqrt{(\omega/p)^2+1}}\right]^{\alpha}$$

$$= 20\log_{10} k - 20\alpha\log_{10}\sqrt{(\omega/p)^2+1}. \tag{1.25}$$

If $\omega \to \infty$, the module is equal to $F(j\omega) \simeq -20\alpha\log_{10}(\omega/p)$ and evaluating in a semi-logarithmic plane, the slope is equal to -20α dB/dec: it may say that the difference in the Bode response between the integer-order system and a FOS lays on the α factor. Easily, it can be demonstrated that the asymptotic diagram error for a α-order fractional system is 3α dB, while in the integer case it is 3 dB.
The phase displacement can be also evaluated from (1.24):

$$\angle F(j\omega) = \alpha\angle\left[\frac{k^{1/\alpha}}{(j\omega/p+1)}\right] = -\alpha\arctan\left(\frac{\omega}{p}\right). \tag{1.26}$$

Even in this case, the limit $\omega \to \infty$ can be evaluated and the phase angle reaches the value of $-\alpha\dfrac{\pi}{2}$.

In particular, starting from the definition of $F(s)$, two different mathematical formulation can be provided:

$$F_1(s) = \frac{k}{(\tau s+1)^{\alpha}} \tag{1.27}$$

$$F_2(s) = \frac{k}{\tau s^{\alpha}+1} \tag{1.28}$$

Taking into account $F_1(s)$ and $F_2(s)$, their Bode diagrams are depicted in Fig. 1.1, imposing $k = 1000$, $\tau = 1 \times 10^{-2}$ s and $\alpha = 0.5$.

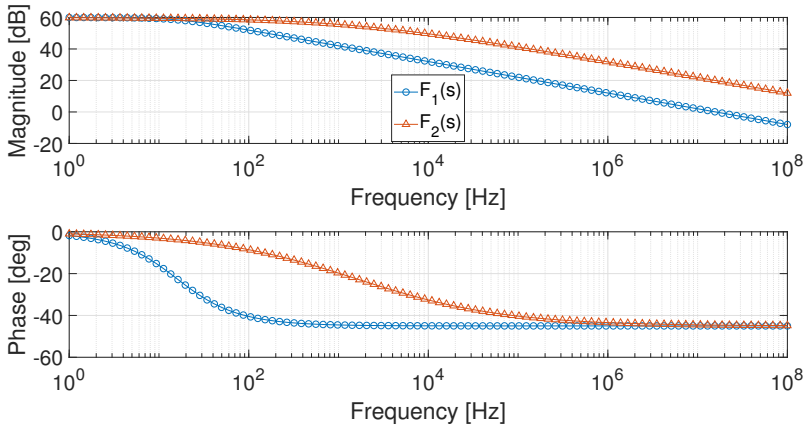

FIGURE 1.1: Bode diagrams for $F_1(s)$ and $F_2(s)$

As it can be observed, the two transfer functions have a very similar behaviour: the magnitude slope is the same (i.e., -10 dB/dec), while the phase responses achieve the same asymptotic value, i.e., -45 deg. The main difference relies on the pole position: $F_1(s)$ has the pole at $1/\tau$, while $F_2(s)$ at $(1/\tau)^{1/\alpha}$. In particular, the latter implementation can be obtained in analog electronic circuits by exploiting fractional-order capacitors (see Sec. 1.3).

Among all the systems, it is well-established that the integrator is widely investigated and exploited in the automatic control field. Therefore, its fractional-order generalization can be stated as follows:

$$Z(s) = \frac{k}{s^\alpha} \tag{1.29}$$

where k is the FO-integrator gain. It can be noticed that, if $\alpha = 1$ and imposing $k = 1/C$, the impedance of a standard capacitor with a capacitance C is obtained. Furthermore, if some different physical phenomena occur inside a device and its behaviour can be governed by (1.29) with $0 < \alpha < 1$, a new class of capacitors can be determined. This class of devices, also known as Fractional-Order Elements (FOEs), will be deeply analyzed in the next chapter.
A comparison between an integer-order integrator and its fractional-order counterpart (with $\alpha = 0.5$ and $k = 1$) is depicted in the next figure.

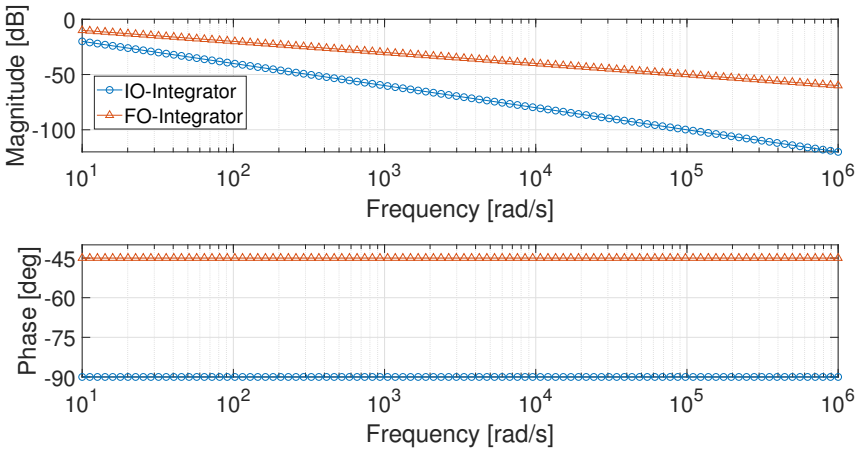

FIGURE 1.2: Bode diagrams of IO- and FO-Integrators with $\alpha = 0.5$ and $k = 1$

From Fig. 1.2, the magnitude and phase slopes of both the IO- and the FO-integrators can be measured: the former has a slope of $-20\,\text{db/dec}$ and a constant phase of $-90\,\text{deg}$, the latter has a slope of $-10\,\text{dB/dec}$ and a phase of $-45\,\text{deg}$. Such a versatility can be achieved by changing the α order will be further investigated in Sec. 1.3, showing the better performances of employing a FO-integrator in the control loop scheme.
Additionally, it must be pointed out that a FOS can be obtained as approximation of integer-order poles and zeros due to its infinity memory. Several approximation strategies have been developed, such as Charef [9], Oustaloup [10] or Matsuda [11] techniques.

Taking into account the results provided in this section, the asymptotic Bode Diagram of a generic transfer function with m zeros and n poles can be obtained by exploiting for each of them the laws defined above ad summing their slopes, as in the IO case.

1.2.3 Time domain response analysis

FOS response depends on the roots of the system characteristic polynomial and, hence, six different cases have to be studied according to the real and imaginary parts of the polynomial roots (e.g. damped oscillations response if $\Re(s) < 0$, $\Im(s) \neq 0$; monotonically decreasing response if $\Re(s) < 0$, $\Im(s) = 0$ and so on).

Given a transfer function $G(s)$, its impulse response (i.e., its inverse Laplace transform) can be computed by defining the so-called *Mittag-Leffler* function $\mathcal{E}_\alpha(\cdot)$ of (1.30), and its behaviour can be analysed by changing the value of α: anomalous relaxation for $\alpha < 1$, exponential for $\alpha = 1$, damped oscillation for $1 < \alpha < 2$, maintained oscillations for $\alpha = 2$.

$$\mathcal{E}_\alpha(x) = \sum_{n=0}^{\infty} \frac{x^n}{\Gamma(n\alpha + 1)} \tag{1.30}$$

A particular case of (1.30) is the *Mittag-Leffler in two parameters* $\mathcal{E}_{\alpha,\beta}(\cdot)$, expressed as:

$$\mathcal{E}_{\alpha,\beta}(x) = \sum_{k=0}^{\infty} \frac{x^n}{\Gamma(\alpha k + \beta)} \tag{1.31}$$

Taking into account these preliminary statements, the mathematical procedure to evaluate the fractional-order transfer function impulse response will be provided.
Considering a simple FOS, such as $G(s) = b/(s+a)^{\alpha}$, it can be rearranged in time domain as:

$$\frac{d^{\alpha}}{dt^{\alpha}} x(t) = -ax(t) + bu(t) \tag{1.32}$$

Equation (1.32) can be thought as a relaxation or oscillation law if $\alpha \in \mathbb{N}$: this parallelism allows to evaluate the response of a generic α-order fractional system. The inverse Laplace transform of (1.32) is not analytically derivable, but it does if $G(s)$ is expressed as series expansion:

$$G(s) = \frac{b}{s^{\alpha} + a} = \frac{b}{s^{\alpha}} \sum_{n=0}^{\infty} \frac{(-a)^n}{s^{\alpha n}} \tag{1.33}$$

Equation (1.33) recalls a fractional-order integrator expression, so using (1.10) for each term of the sum, the impulse response is obtained:

$$g(t) = \mathcal{L}^{-1} \left\{ \frac{b}{s^{\alpha}} \sum_{n=0}^{\infty} \frac{(-a)^n}{s^{\alpha n}} \right\} = bt^{\alpha-1} \sum_{n=0}^{\infty} \frac{(-a)^n t^{n\alpha}}{\Gamma(n\alpha + 1)} \tag{1.34}$$

Equation (1.34) can be rearranged using the Mittag-Leffler function in one parameter defined above:

$$g(t) = \frac{d^{1-\alpha}}{dt^{1-\alpha}} \mathcal{E}_{\alpha}(-at^{\alpha}) \tag{1.35}$$

This last equation is fundamental for FOS transient analysis because it allows to evaluate any kind of response like step or ramp response and so on.

In case of a commensurate-order system, starting from the pseudo-rational transfer function $H(\lambda)$ of (1.16), the impulse response can be evaluated as follows:

$$\mathcal{L}^{-1}\{H(\lambda)\} = \mathcal{L}^{-1} \left\{ \frac{\sum_{k=0}^{m} b_k \lambda^k}{\sum_{k=0}^{n} a_k \lambda^k} \right\} = \mathcal{L}^{-1} \left\{ \sum_{k=0}^{n} \frac{r_k}{\lambda - \lambda_k} \right\} \tag{1.36}$$

Equation (1.36) can be solved by evaluating the inverse Laplace transform of (1.37) and putting $\alpha = \beta$,

$$\mathcal{L}^{-1} \left\{ \frac{s^{\alpha-\beta}}{s^{\alpha} - \lambda_k} \right\} = t^{\beta-1} \mathcal{E}_{\alpha,\alpha}(\lambda_k t^{\alpha}), \tag{1.37}$$

Finally, the impulse response of the commensurate FOS is given by:

$$g(t) = \sum_{k=0}^{n} r_k t^{\alpha-1} \mathcal{E}_{\alpha,\alpha}(\lambda_k t^{\alpha}) \tag{1.38}$$

Evaluating (1.38) and the related step response, the latter can assume several forms according to $\angle(\lambda_k)$:

- monotonically decreasing if $|\angle(\lambda_k)| \geq \alpha\pi$;
- oscillatory with decreasing amplitude if $\alpha\pi/2 < |\angle(\lambda_k)| < \alpha\pi$
- oscillatory with constant amplitude if $|\angle(\lambda_k)| = \alpha\pi/2$;
- oscillatory with increasing amplitude if $|\angle(\lambda_k)| < \alpha\pi/2,\ |\angle(\lambda_k)| = 0$;
- monotonically increasing if $|\angle(\lambda_k)| = 0$.

Considering a SISO system expressed by (1.21),

$$\mathbf{X}(s) = (s^\alpha \mathbf{I} - \mathbf{A})^{-1}\mathbf{B}\mathbf{U}(s) + (s^\alpha \mathbf{I} - \mathbf{A})^{-1}s^{\alpha-1}\mathbf{x}(0),$$

the state evolution can be evaluated by computing the inverse Laplace transform of the above expression:

$$\begin{aligned} x(t) &= \mathcal{L}^{-1}\{\mathbf{X}(s)\} = \\ &= \mathcal{L}^{-1}\left\{(s^\alpha \mathbf{I} - \mathbf{A})^{-1}\mathbf{B}\mathbf{U}(s) + (s^\alpha \mathbf{I} - \mathbf{A})^{-1}s^{\alpha-1}\mathbf{x}(0)\right\} \end{aligned} \tag{1.39}$$

Defining $\hat{\Phi}(t) = \mathcal{L}^{-1}\left\{(s^\alpha \mathbf{I} - \mathbf{A})^{-1}\right\}$ and $\Phi(t) = \mathcal{L}^{-1}\left\{(s^\alpha \mathbf{I} - \mathbf{A})^{-1}s^{\alpha-1}\right\}$ both for $t \geq 0$ and applying the convolution Laplace property operator, the states $x(t)$ can be expressed as:

$$\begin{aligned} x(t) &= \Phi(t)x(0) + \hat{\Phi}(t) * [\mathbf{B}u(t)] = \\ &= \Phi(t)x(0) + \int_0^t \hat{\Phi}(t-\tau)\mathbf{B}u(\tau)d\tau \end{aligned} \tag{1.40}$$

From (1.40), it is easily deduced that $\Phi(t)$ can be defined as *transition matrix*. The following reported calculations define a new methodology for evaluating the transition matrix, according to the related expression used in the integer-order counterpart.

Considering an autonomous system like $\mathcal{D}^\alpha x(t) = \mathbf{A}x(t)$, $\mathbf{x}(0) = \mathbf{x}_0$, using the Caputo definition, according to the integer-order case, the states $x(t)$ can be rearranged as:

$$x(t) = \mathbf{A}_0 + \mathbf{A}_1 t^\alpha + \mathbf{A}_2 t^{2\alpha} + \cdots + \mathbf{A}_k t^{k\alpha} + \cdots \tag{1.41}$$

Obviously, for $t = 0 \rightarrow \mathbf{x}(0) = \mathbf{A}_0$. If the α-order derivative of (1.41) is evaluated, taking also into account the following propriety:

$$\mathcal{D}^\alpha t^\gamma = \frac{\Gamma(\gamma+1)}{\Gamma(\gamma+1-\alpha)}t^{\gamma-\alpha}, \tag{1.42}$$

the equation becomes:

$$\mathcal{D}^{\alpha}x(t) = \mathbf{0} + \mathbf{A}_1\Gamma(1+\alpha) + \mathbf{A}_2\frac{\Gamma(1+2\alpha)}{\Gamma(1+\alpha)}t^{\alpha} + \cdots + \\ + \mathbf{A}_k\frac{\Gamma(1+k\alpha)}{\Gamma(1+(k-1)\alpha)}t^{(k-1)\alpha} + \cdots = \mathbf{A}\mathbf{x}(t) \tag{1.43}$$

Setting $t = 0$ in the above equation, it follows that:

$$\mathbf{A}_1 = \mathbf{A}\frac{\mathbf{x}(0)}{\Gamma(1+\alpha)} \tag{1.44}$$

Applying this iterative procedure for successive α-order derivative, i.e., 2α, 3α, ..., matrices of coefficients A_k can be obtained and they are equal to:

$$\mathbf{A}_k = \mathbf{A}^k\frac{\mathbf{x}(0)}{\Gamma(1+k\alpha)} \tag{1.45}$$

Finally, the solution of (1.41) can be evaluated. Indeed, it is equal to the following relationship:

$$\mathbf{x}(t) = \mathbf{x}(0) + \mathbf{A}\frac{\mathbf{x}(0)}{\Gamma(1+\alpha)}t^{\alpha} + \mathbf{A}^2\frac{\mathbf{x}(0)}{\Gamma(1+2\alpha)}t^{2\alpha} + \cdots + \mathbf{A}^k\frac{\mathbf{x}(0)}{\Gamma(1+k\alpha)}t^{k\alpha} + \\ + \cdots = \left(\sum_{k=0}^{\infty}\mathbf{A}^k\frac{\mathbf{x}(0)}{\Gamma(1+k\alpha)}t^{k\alpha}\right)\mathbf{x}(0) = \mathcal{E}_{\alpha,1}(\mathbf{A}\mathbf{t}^{\alpha})\mathbf{x}(0) = \\ = \mathbf{\Phi}\mathbf{x}(0) \tag{1.46}$$

From (1.46) it is quite evident that the Mittag-Leffler function $\mathcal{E}_{\alpha,1}(\mathbf{A}\mathbf{t}^{\alpha})$ has the same role of the exponential matrix $e^{\mathbf{A}t}$: the integer-order transition matrix is a particular case of the Mittag-Leffler function $\mathcal{E}_{\alpha,1}(\mathbf{A}\mathbf{t}^{\alpha})$, also called *Mittag–Leffler matrix function* with $\alpha = 1$.

1.2.4 Stability

An important topic to deal with is the *stability* of a FOS. The study of this argument can be introduced by looking at a simple fractional-order polynomial with $\alpha \in \mathbb{R}$:

$$a_n s^{\alpha_n} + a_{n-1}s^{\alpha_{n-1}} + ... + a_0 s^{\alpha_0}. \tag{1.47}$$

The domain of the complex variable s can be seen as a Riemann surface with finite sheets only if $\alpha_i \in \mathbb{Q}+$, $\forall i$. In details, the *principal Riemann sheet* is the one where $-\pi < \angle(s) < \pi$.
Imposing $\alpha_i \in \mathbb{Q}+ : \alpha = 1/q$, $q \in \mathbb{N}+$ and the complex variable $s = |s|e^{j\phi}$, the Riemann sheets will be:

$$(2k+1)\pi < \phi < (2k+3)\pi \quad \text{with} \quad k \in [-1; q-2]. \tag{1.48}$$

From (1.48), the principal Riemann sheet is obtained for $k = -1$ and globally q sheets are found. Mapping $w = s^{\alpha} \rightarrow w = |w|e^{j\vartheta}$, the sheets will be:

$$\alpha(2k+1)\pi < \vartheta < \alpha(2k+3)\pi \quad \text{with} \quad k \in [-1; q-2], \tag{1.49}$$

where the w-plane region is defined by $-q\pi/2 < \angle(w) < q\pi/2$ and corresponds to the right half plane of the principal Riemann sheet.
It is important to analyse the Riemann sheets because a fractional-order polynomial, like (1.47), has infinity roots but, at the same time, only the ones which belong to the principal Riemann sheets determine several different dynamics (i.e., oscillations at constant amplitude, damped oscillations, increasing oscillations and so on) and, therefore, its related stability; on the contrary, roots belonging to secondary sheets are related to monotonically decreasing functions.

In the following, several stability definitions will be declared.

Definition 1.1. BIBO stability
A general irrational fractional-order system $G(s) = P(s)/Q(s)$ is BIBO stable if and only if the following condition is verified:

$$\exists M: \quad |G(s)| \leq M \quad \forall s \quad \Re(s) > 0 \tag{1.50}$$

The imposed condition implies that $Q(s)$ must have all the roots in the principal Riemann sheet.

Definition 1.2. Commensurate-order stability
Given a commensurate-order system $H(\lambda) = \dfrac{\sum_{k=0}^{m} b_k \lambda^k}{\sum_{k=0}^{n} a_k \lambda^k}$, where $\lambda = s^\alpha$, it will be stable if and only if:

$$\forall i: \quad |\angle(\lambda_i)| > \alpha\frac{\pi}{2} \tag{1.51}$$

where λ_i are the denominator roots of $H(\lambda)$.

Definition 1.3. State-space stability
Given a commensurate-FOS with state-space matrices $\{\mathbf{A}, \mathbf{B}, \mathbf{C}, \mathbf{D}\}$, it will be stable if and only if:

$$|\angle(\text{eig}(\mathbf{A}))| > \alpha\frac{\pi}{2}, \tag{1.52}$$

where $\text{eig}(\mathbf{A})$ are the solutions of the characteristic polynomial $\det(s^\alpha\mathbf{I} - \mathbf{A})$, i.e., the system poles.

A non-linear FOS is a incommensurate system represented with the following mathematical expression for a generic i-th space-state variable:

$$\mathcal{D}_{\mathrm{t}}^{\mathrm{q_i}} = f_i\left(x_1(t), x_2(t), \ldots, x_n(t), t\right), \tag{1.53}$$

$$x_i(0) = c_i, \quad \forall i: 1 < i < n, \tag{1.54}$$

where c_i are the initial conditions of the state variables. Considering $\mathbf{q} = [q_1\, q_2\, \ldots\, q_n]^T$, $q_i \in]0;2[\quad \forall i: 1 < i < n$, $\mathbf{x} \in \mathbb{R}^{n\times 1}$ and $\mathbf{f} = [f_1\, f_2\, \ldots\, f_n]^T$, (1.54) can be expressed in a vectorial form:

$$\mathcal{D}^{\mathbf{q}}\mathbf{x} = \mathbf{f}(\mathbf{x}) \tag{1.55}$$

Equilibrium points of equation (1.55) can be evaluated by imposing $f(x) = 0$. These equilibrium points are stable if the following definition is verified.

Definition 1.4. Non linear commensurate-FOS stability
Given a non linear FOS expressed by (1.55), supposing $q_1 = q_2 = \cdots = q_n \equiv q$ (i.e., the fractional-order is the same for all variables), the system linearisation represented by the *Jacobian matrix* $\mathbf{J} = \partial\mathbf{f}/\partial\mathbf{x}$ can be defined. Evaluating the system linearisation in its equilibrium points, they will be asymptotically stable if all the eigenvalues of $\mathbf{J}$ verify the following relationship:

$$|\angle(eig(\mathbf{J}))| = |\angle(\lambda_i)| > q\frac{\pi}{2} \quad \forall i : 1 < i < n \tag{1.56}$$

Definition 1.5. Non linear incommensurate-FOS stability
Given a non linear FOS expressed by (1.55), supposing $q_1 \neq q_2 \neq \ldots \neq q_n$ (i.e., the fractional-order is not the same for all variables) and furthermore $q_i = v_i/u_i,\ u_i \in \mathbb{Z}+\forall i : 1 < i < n$, the system linearisation represented by the *Jacobian matrix* $\mathbf{J} = \partial\mathbf{f}/\partial\mathbf{x}$ can be defined. Evaluating the system linearisation in its equilibrium points, they will be asymptotically stable if:

$$|\angle(\lambda)| > \gamma\frac{\pi}{2} \tag{1.57}$$

where:

- $\gamma = 1/m$, being m the LCM of the denominators of q_i;
- λ are the roots of the following equation:

$$\det\left(\mathrm{diag}\left(\begin{bmatrix}\lambda^{mq_i} & \lambda^{mq_2} & \ldots & \lambda^{mq_n}\end{bmatrix} - \mathbf{J}\right)\right) = 0. \tag{1.58}$$

1.3 Fractional-Order Controllers

FC is widely used in several fields from the reduction of the transfer function order of system [12] to the description of economic processes [13], from civil engineering application [14] to medical applications [15]. See [16] for a detailed state of art of FOS application.

Among its development fields, FC has been deeply investigated and studied for its employment in the automatic control domain. Indeed, it has been widely proved that Fractional-Order Controllers provide better performances compared to its integer-order counterpart, like the Fractional-Order Proportional-Integral-Derivative (FO-PID) controller proposed by Podlubny in 1999 [17] or the CRONE (Commande Robuste d'Ordre Non Entier) strategy established by Oustaloup [18]. Application of Fractional-Order Controllers can be found in [19]–[22]. In each of these works, the main advantage of the FC is given by the integral (or derivative) fractional-order: it provides one (or two) extra degree of freedoms, which can assure better and more robust performances.

In general, by tuning properly a controller is possible to fulfill several constraints related to the system performances [6]. Defining the controller Transfer Function (TF) as $C(s)$ and the plant to control as $P(s)$, the constraints to satisfy are:

Phase and Gain margins

Phase and gain margins for the crossover frequency of a plant are the most fulfilled constraints for every controlled system. The phase margin M_φ provides useful information about the robustness of the controlled plant, while the gain margin M_G establishes how much the gain can vary before destabilizing the closed-loop system. Formally, defining ω_c and ω_π as the crossover pulsation and the one when the open-loop TF reaches a phase of $-\pi$, the gain and phase margins can be computed as follows:

$$M_G = \left.\frac{1}{C(j\omega)P(j\omega)}\right|_{\omega=\omega_\pi} \tag{1.59}$$

$$M_\varphi = \pi + \angle\left(C(j\omega)P(j\omega)\right)|_{\omega=\omega_c} \tag{1.60}$$

As a consequence of (1.60) and by the definition itself of the ω_c, the magnitude of $C(s)P(s)|_{\omega=\omega_c}$ is equal to 0 dB.

Gain plant variation robustness

The gain variation condition can be expressed as follows:

$$\left.\frac{d}{d\omega}\left(C(j\omega)P(j\omega)\right)\right|_{\omega=\omega_c} = 0 \tag{1.61}$$

Defined $G(s) = C(s)P(s)$ as the system open-loop transfer function, (1.61) represents a particular condition where the phase of $G(s)$ has to be flat in a surrounding of ω_c. This result leads to two important properties for the closed-loop transfer function:

- robustness to gain variation;
- constant overshoot of step response with respect to gain variation.

For such reasons, this constraint is also defined as *isodamping property*.

Output disturbance rejection

Defining the sensitivity function $S(s)$ as:

$$S(s) = \frac{1}{1 + C(s)P(s)}, \tag{1.62}$$

its maximum acceptable value S_{max} [dB] and its maximum pulsation band ω_s, the output disturbance rejection constraint can be defined as:

$$|S(j\omega)| \leq S_{max}, \qquad \forall\omega \leq \omega_s \rightarrow |S(j\omega_s)| = S_{max} \tag{1.63}$$

High-frequency noise rejection

The high-frequency noise rejection constraint takes into account the complementary sensitivity function $T(s)$ as:

$$T(s) = \frac{C(s)P(s)}{1 + C(s)P(s)} \tag{1.64}$$

Defining the minimum pulsation ω_t starting from which the noise should be rejected and its maximum acceptable value T_{max} [dB], this constraint can be established as:

$$|T(j\omega)| \leq T_{max}, \qquad \forall \omega \geq \omega_t \rightarrow |T(j\omega_t)| = T_{max} \tag{1.65}$$

Steady-state error removal

It is well-known that the steady-state error in time-domain response can be removed by adding a proper realized integrator. Applying the Final-Value Theorem for a FOS, it is possible to demonstrate that it reaches a steady-state error equal to zero if $\alpha > 0$. Despite of it, a FOS requires more transient to cancel this error. Taking into account this drawback, as reported in [6], the fractional-order integrator (that is usually band-limited) should be implemented by exploiting also an integer-order one, i.e., $1/s^{\alpha} = s^{(1-\alpha)}/s$. Similarly, if a fractional-order zero is used, the same management should be taken into account.

Each of the discussed constraints can be fulfilled by exploiting one of the available controller's degree of freedom. Therefore, if the controller has more degree of freedom due to its fractional-order implementation, the overall closed-loop system can satisfy several constraints and be more robust compared to its integer-order counterpart. Furthermore, the robust performances can be achieved even if there are uncertainties on system parameters. Application of FO-PID and tuning procedures can be found in [23]–[25] even if they are still related to the academic field. In a recent study of 2021, Tepljakov et al. [26] give a survey of all the FO-PID design procedures (both in digital and analog implementations), describing their benefits and possible applications industrial processes. In particular, they have emphasized that FO-PID controllers are now mature to be integrated in the industrial environment.

Besides FO-PID implementation, other controllers, like lead or (lag) compensators, can be defined of fractional-order. In [6], chapter 8, Monje et al. show the possibility of implementing a fractional-order lead or lag compensator. Additionally, they demonstrate that a fractional-order lead compensator can be considered as a FO-PD controller, while a FO-lag compensator as a FO-PI realization. Such a statement allows to consider this other class of controller as robust and more performing compared to their standard implementation.

In particular, it is possible to describe two different type of FO-lead compensator (when $\alpha > 0$) transfer function:

$$C(s) = k \cdot \left(\frac{\tau s + 1}{x\tau s + 1}\right)^{\alpha}, \quad 0 < x < 1 \tag{1.66}$$

and

$$C(s) = k \cdot \frac{\tau s^{\alpha} + 1}{x\tau s^{\alpha} + 1}, \quad 0 < x < 1 \tag{1.67}$$

Taking into account the active electronics implementation of a general lead compensator, reported in Fig. 1.3, it is possible to notice that its fractional-order realization can be obtained by using a FO-capacitor, whose impedance is represented by (1.29). Therefore, the overall impedance of the circuit is described by (1.67). As a consequence, for analog realizations of FO-compensators, (1.66) should be avoided during the design procedure, even if no particular differences, except the zero and pole positions, can be detected.

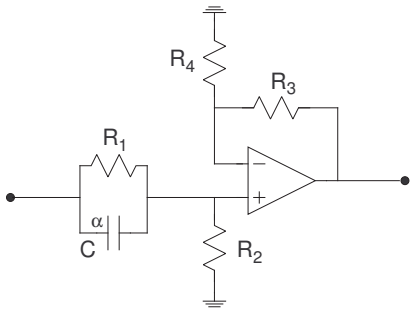

FIGURE 1.3: FO-lead compensator schematics

The time constants $\tau_p = x\tau$, $\tau_z = \tau$ and the gain of the circuit can be easily obtained as follows:

$$\begin{aligned} \tau_z &= (R_1 C)^{1/\alpha} \\ \tau_p &= \left(\frac{R_1 \cdot R_2}{R_1 + R_2} \cdot C \right)^{1/\alpha} \\ k &= \left(1 + \frac{R_3}{R_4} \right) \cdot \frac{R_2}{R_1 + R_2} \end{aligned}$$

Exploiting the frequency response of the FO-lead compensator as explained in Sec. 1.2.2, it is possible to notice the benefits of the α order: if α is small, the distance between the zero and pole is greater. This leads to an enhanced phase maintenance and, more in general, gives the opportunity of employing a more robust and versatile controller.
In this work, since the analog-implementation of the controller is realized, the standard design procedure of a lead compensator is developed. Furthermore, this choice allows to highlight the flexibility and robustness of the FO-controller, that includes by itself the *isodaming property* introduced before. For sake of brevity, results and discussion are directly reported in Sec. 3.3.2, where evidence of FO-controller benefits will be deeply provided.

In the next chapter, the study and different technological implementation of fractional-order capacitors, briefly introduced in Sec. 1.2.2, will be described.

Chapter 2

Fractional-Order Elements

As already mentioned in the previous chapter, one of the most proficient research field of FC is related to the physical realization of devices whose behaviour is intrinsically of fractional order, i.e., their governing differential equations cannot be described by means of the common Integer Calculus. Such devices are defined as *Fractional-Order Elements* (FOEs).

More specifically, among the class of FOEs, a lot of attention is paid to the implementation of FO-capacitor. It has been demonstrated in Sec 1.2.2 that the impedance of this class of device is equivalent to deal with a FO-integrator, giving, therefore, the possibility to realize more robust controllers, as discussed in Sec. 1.3. By looking at their frequency response, it can be observed that they, ideally, maintain a phase constant to a different value with respect to the common $-90\,\text{deg}$ of the standard capacitors. For this reason, FO-capacitors are also called *Constant-Phase Elements* (CPEs). In reality, due to parasitic effects and technological limits, it is no possible to have a constant phase in all the frequency domain and, hence, they act as CPEs only in a limited range: this drawback limits their application fields and their model cannot be generalized. On the other hand, such a disadvantage feeds the research to improve and enhance their performances. Indeed, new and promising technological realizations are spreading in literature.

The chapter of this work will cover the presented research field, starting from describing the physical phenomena that occur inside a CPE, moving towards an analysis of FO-capacitor and recalling the main technological implementation that have been exploited for realizing this new class of devices.

2.1 Constant-Phase Element: an overview

In electrochemistry, systems are subjected to impedance measurements by exploiting the so-called Electrochemical Impedance Spectroscopy (EIS) technique [27], where the dynamics of an electrochemical system is analyzed by

applying a difference of potential. This measurement allows to study which physical phenomena occur at the top of the surface of a metal, like corrosion [28], transport process [29] and so on. The need of CPE arises every time that an electrochemical system cannot be represented by the common equivalent electric component [30] like resistors, capacitors or inductors. The most used symbol for CPE is the following one:

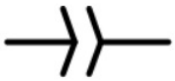

FIGURE 2.1: Electronic symbol of a CPE.
Credits to lacey.se

Defining the CPE impedance as $Z_c(s)$, and exploiting the FO-integrator impedance of (1.29) with $k = 10^{-6}$, a comparison of a standard capacitor and a CPE is reported in Fig. 2.2, where their Nyquist plots are depicted.

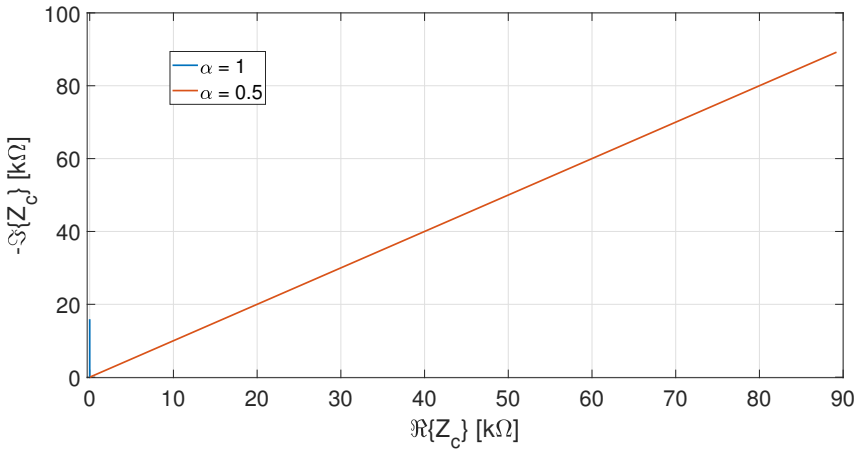

FIGURE 2.2: Nyquist plots of $Z_c(s)$ with $\alpha = 1$ and $\alpha = 0.5$, respectively

It can be observed that the CPE has a completely different shape with respect to the ideal capacitor: the Nyquist plot is a line whose angle with the real axis is equal to $\alpha\pi/2$. This result can be easily obtained by applying the Euler formulas [31]. Considering the aforementioned statement, and, furthermore, the frequency response depicted in Sec. 1.2.2, a device can be defined as CPE only if, at high frequencies, its phase response is equal to $-\alpha\pi/2$ [32].

Such an "imperfect" behaviour led Jean, in the 1997, to define the concept of *phasance* [33] that includes imperfect electronic components behaviour. Indeed, a CPE can be thought as a component that models a *double layer capacitor*, also defined as *imperfect capacitor*.

2.1.1 Double-layer capacitor

In [34], Sudhakar et al. give a detailed explanation about the principle of a Double-Layer Capacitor (DLC). Briefly, taking into account the electrochemical cell depicted in Fig. 2.3, if the switch is closed and, hence, the current flows inside the carbon rods, the charges starts to accumulate on the electrode/electrolyte interface, where positive and negative charges are balanced

according to the polarization of the carbon rod. When the switch is open, it is still possible to measure a voltage across the two carbon rods. The energy, indeed, is stored thanks to the series of the double-layer capacitor.

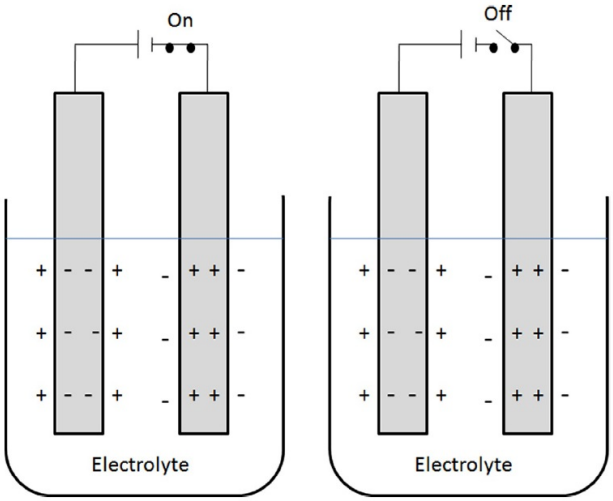

FIGURE 2.3: Working principle of a Double-Layer Capacitor.
Credits: Sudhakar et al. [34]

Two different charge layers arise:

- the first layer is made of absorbed charges (positive or negative) in the surface of the material due to chemical reactions;
- the second layer is made of ions that, due to the electric Coulomb forces, are attracted towards the polarized surface.

More specifically, the second layer of a DLC depends on attracted ions and, hence, they can move only if some further physical phenomena occur. For this reason, it is also called *diffuse layer* [34], [35]. Taking into account two parallel electrodes with a fluid dielectrics inside, the double-layer capacitor is schematized in Fig. 2.4.

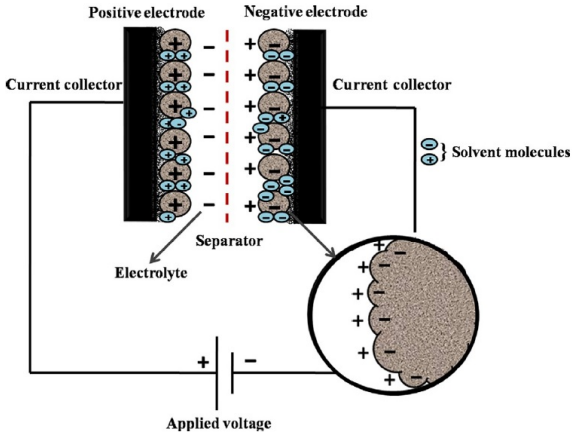

FIGURE 2.4: Parallel plate Double Layer Capacitor.
Credits: Sudhakar et al. [34]

Scientists have investigated the physical origin of the CPE, because an unique explanation is not sufficient. Among the most recognize theories,

a CPE can arise due to the roughness of the electrodes [36], [37], fractal dimension [38], anomalous diffusion [39], time-constant distribution [40] or porous electrodes [41]. In particular, this latter property has been widely studied and applied with the aim to realize CPEs.

2.2 State of Art about CPE realizations

The CPE behaviour is represented by a fractional-order power law [42] and its impedance can be formulated as follows:

$$Z(s)_{CPE} = \frac{1}{Fs^{\alpha}} = Qs^{-\alpha} \tag{2.1}$$

It is well-known that, for standard capacitors, their capacitance is measured in Farad [F], while some changes have to be done for CPEs. Indeed, their capacitance measurement unit is [$F/s^{1-\alpha}$] [43]. For such reason, in reality, the capacitance of CPEs is defined as *pseudo-capacitance*, in order to differentiate it from the standard one. In [44] a mathematical law that put in relationship a pseudo-capacitance C_α with the corresponding *real-capacitance* C_i has been defined, and it is equal to:

$$C_i = \frac{C_\alpha \cdot \omega^{(\alpha-1)}}{\sin\left(\alpha\frac{\pi}{2}\right)} \tag{2.2}$$

where ω is the pulsation at which the effective capacitance is computed.

Starting from the very first fractional-order capacitor realization by Cole et al. in 1941 [45], several strategies have been studied for obtaining these devices by changing the inner dielectrics, geometry, technological processes and so on.
Based on the survey conducted by Shah et al. in [46], three main classes of FOEs can be detected: multi-component, emulated fractional-order capacitors and single-component. Each of this class, based on the detailed work of Shah et al., will be described in the following.

2.2.1 Multi-component FOEs

The FOEs multi-component implementations are based on the work of Heaviside, in which he described the infinite RC networks the transmission line by means of a fractional-order impedance whose order was equal to 0.5 [47]. Starting from the Heaviside's work, several scientists have defined some strategies to obtain a constant phase shifting by connecting in series or in parallel RC groups, like Darlington [48], Douglas [49], Morrison [50] or Lerner [51]. However, none of the aforementioned works were focused on the implementation of fractional-order capacitor as components to exploit in electronic circuit.
The first work that explicitly defined a strategy for implementing a fractional-order integrator was of Carlson in the 1961 [52] while, he with Halijak in the 1964 defined a proper way to obtain a fractional-order capacitor by exploiting the Newton process [53] by a proper connection of cascaded series RC groups, with a final resistive load.

In 1966 Dutta Roy et al. realized an infinite cross RC ladder network [54] by using the Continued Fraction Expansion method for evaluating the impedance of the uniform distributed RC networks. Furthermore, they stated that a non-uniform RC network provides better results in approximating the order 0.5 at low frequencies.
In the 1973, Oldham realized a fractional-order capacitor of order 0.5 by implementing a non-infinite ladder network of parallel RC groups [55]. In particular, for obtaining fractional orders different from 0.5, resistance and capacitance values were computed with a geometric progression, removing the limit of random values of the previous methods.
Basing on this pioneering works, other strategies have been developed by exploiting RC ladder networks [56]–[59]. See Sec. 3.1 of Shah et al. work [46] for further details about these methods.

In conclusion, all the presented strategies for multi-components FOEs are restricted to academia because several components are required, making difficult their implementation in real circuits. Furthermore, all these works try to reproduce an order of 0.5, without the possibility of tuning the parameters in a different way.

2.2.2 Emulated fractional-order capacitors

Among the emulated fractional-order capacitors, the first proposed technology is based on supercapacitors [60], i.e., capacitors with a greater capacitance with respect to standard capacitor with a limit in the voltage applicable. Supercapacitors are also modelled by exploiting RC groups, such as the multi-component FOEs realizations [61], even if better modelling performances were obtained by applying FC, as Allagui et al. showed in [44], where fractional derivatives are used to avoid errors in their characterization, design and performance evaluation (such as energy stored or power analysis). Other FO-modelling of supercapacitors are reported in [62]–[64].

Another important strategy that arises a lot of interest in the realization of FO-capacitor is the CMOS (Complementary Metal-Oxide Semiconductor)-based emulation one. The first approach, proposed by Dimeas et al., makes use of passive and active elements, as the Current Feedback Operational Amplfiers, for realizing fractional-order inductors or capacitors [65]. A further possible realization is provided by Tsirimokou et al. in [66], [67] by exploiting Operational Transconductance Amplifiers (OTAs). They realized a second-order filter able to emulate a fractional-order capacitors or, more in general a fractional-order filter. In particular, they discovered a mathematical law between the FO-capacitor α order and the bias current that can be provided to the circuit thanks to two external capacitors: values between 0.3 and 0.7 were obtained in a bandwidth of 10 Hz to 1000 Hz with a 0.35 µm CMOS technology.

2.2.3 Single-component FOEs

Single-components FOEs are raising more and more interest in the academic world thanks to their compactness and ease of use: they can be easily exploited in implementation of fractional-order circuits, like the standard capacitors. In

this section, based on the survey of Shah et al. [46], the main technologies investigated in their fabrication are presented.

The first technology for single-component FOEs realization is based on fractal structures, that have interested mathematicians first and then engineers. Haba et al. in the 1997 [68] demonstrated, by exploiting fractal materials made of silicon opportunely treated in MOS (Metal-Oxide Semiconductor) technology, the possibility of obtaining a CPE with a phase angle of about -36 deg. Influences of inner parameters, such as the series or parallel resistors or the capacitor, and different pattern structures have been investigated [69]. Components have been also realized with Metal-Insulation-Semiconductors fractal structures [70].
Also based on fractal structures, Jesus et al. [71] developed a fractional-order capacitor in a electrolyte process, where: the electrodes exhibited a fractal pattern in their surface, a sodium chloride solution was used as electrolyte and sand has been used as porous material inside the solution. By varying the fractal surface, they obtained an α order between 0.2 and 0.6.

Another approach has been proposed by Biswas et al. in 2006 [72]. They realized electrochemical capacitors by exploiting Poly Methyl MethAcrylate (PMMA), a porous material, for coating a copper clading. The obtained device was immersed in water at room temperature. They measured a constant-phase between -15 deg and -60 deg in a wide frequency range and, above all, they tested the reliability of the CPE by implementing a fractional-order differentiator.
Subsequently, in the 2013 Mondal et al [61], using the same technology, implemented copper and platinized silicon electrodes, put inside an agarose powder (a bio-derived ionic gel). Exploiting several parameters, such as the ionic medium, electrodes, or the amount of ionic gel, they tested the stability of the realized CPEs, obtaining an α order between 0.1 and 0.9, with a maximum longevity of 6.5 months.
It can be observed that, the aforementioned technologies make use of electrolytes or ionic solutions.

Another important subset in the single-component FOEs realization is represented by the *solid-state implementation*. Generally, they exploit nanocomposite materials inside a polymeric matrix used as dielectrics, obtaining a constant-phase for about 3 - 4 decades.

The first proposed technology [73] uses graphene-polymer composites inside a polymeric matrix. Such a polymer is then used as dielectric in a parallel plate capacitor. The graphene particles create RC groups inside the dielectric and, then, their different time constants determine the fractional order of the entire device. These devices have an α order that varies from 0.3 to 0.7 by changing the percentage of graphene inside the polymer.

A different implementation process is described by Buscarino et al. [74], where particles of Carbon Black (CB) were diffused inside a polymeric matrix made of Sylgard_{184}, used as dielectrics in cylindrical capacitors. Several FOEs have been realized by changing some construction parameters, such as the percentage of CB or the curing temperature. An α order between 0.7 and 0.8 was obtained.

Exploiting also the carbon-based structures, Adhikary et. al developed a new type of FOE by realizing a dielectrics made of Carbon-NanoTubes (CNTs)

[75]. Nanotubes were used inside a polymeric composite coating and an averaged α order of 0.34 was obtained. Starting from these results, Adhikary in 2020 conducted a detailed study realizing a new type of FOE [76], where the electrodes had been coated with a composite of CNTs and polyimide gels. Some technological parameters (temperature and CNT variations) had been investigated in order to understand how its fractional-order was influenced: by varying the electrolyte's conductivity or the electrodes length was possible to achieve a phase lag between -11 deg and -42 deg. Therefore, the realized device had been employed in some circuit applications, such as a fractional-order parallel resonator and a fractional-order high pass filter, providing proof of stability.
Similarly, Multi-Wallet CNTs (MWCNTs) were exploited by Agambayev et al. [77] and John et al. [78] inside a polymeric composite without and with epoxy resin composite, respectively. Furthermore, John et al. have provided that the diffusion of charges carrier inside a dispersing medium is responsible for the fractional-order behaviour. Both proposed technologies showed good performances as CPEs in a wide frequency range: the former from -65 deg to -7 deg in the range 150 kHz to 2000 kHz, the latter from -85 deg to -45 deg in the ranges 110 Hz to 1100 Hz, 10 kHz to 118 kHz and 230 k Hz to 20 000 k Hz. Other technologies, such as ferro-electric-based FOEs, metal-polymeric composite devices or resistive-capacitive films-based FO-capacitors, and the comparison of all the discussed technologies are reported in the survey of Shah et al. [46], see Sec. 3.2 for more details.

Basing on the reported solid-state technologies, their common feature is the employment of a polymeric matrix and the diffusion of porous material inside it. Such a scenario leads to a distribution of time-constants, as reported in [34], that determines the fractional-order nature of the devices.
More specifically, this main concepts and the work realized by Buscarino et al. [74] build the foundations for the realization of the Carbon Black-based FOE described in the next chapter.

Additionally, none of the presented technologies, both multi-components, single-components and emulation, focus on ecological drawbacks of these implementations. For this reason, concurrently to the Carbon Black-based FOE implementation, a new green material, the Bacterial Cellulose, is investigated for the development of a green-based device, whose governing equations are described by FC.

Chapter 3

Carbon Black-based FOEs

In this chapter, based on the work presented by Buscarino et al. [74], a new FOE based on Carbon Black dielectrics is presented. FOEs are realized with the same main technology but some fabrication process parameters are studied more in details. Furthermore, the curing temperature of the devices is analysed as possible technological parameters to determine the fractional order of the developed devices.

More specifically, the proposed work starts with presenting the technological implementation procedure, then the device characterization is performed looking to both a wide frequency domain and to a restricted one where they act as CPE. Finally, several circuit applications are reported, highlighting the advantages of employing these devices. In conclusion, as stated in Sec. 1.3, the possibility of achieving better control performances is proved by realizing a Fractional-Order Controller.

3.1 Realization and characterization

As reported in Sec. 2.2.3, one of the most investigated technology is related to the employment of a polymeric matrix, where some conductive particles are dispersed inside. The proposed FOE [79] exploits a cylindrical shape, as reported in Fig. 3.1, where the internal cylinder has a diameter of 6 mm and a height of 120 mm, while the external cylinder has a diameter of 12 mm and its height is 80 mm. Finally, the polymeric dielectrics is inserted between these two concentric cylinders.

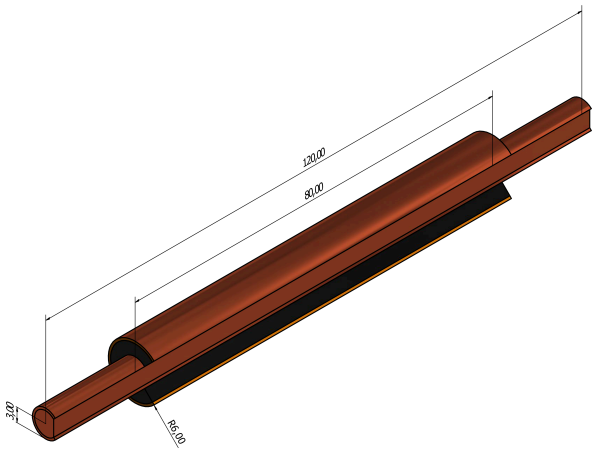

FIGURE 3.1: Schematics of the CB-based FOE

3.1.1 Materials

The polymeric matrix is realized by exploiting the Sylgard$_{184}$ as main material. It is a silicon elastomer, purchased from *Dow Corning*, and consists of two main parts, defined *Part A* and *Part B*, respectively. The former consists of a vinyl-terminated PolyDiMethylSiloxane (PDMS) prepolymer, the latter of a methylhydrosiloxane copolymer chains with a platinum catalyst and an inhibitor. It must be noticed that Part B acts as crosslinking curing agent in the dielectrics realization.
Accordingly to manufacturer suggestions, Part A is mixed with Part B in a 10:1 weighted ratio and then cured at room temperature for 48 h. The Curing Temperature (CT) has been chosen as technological parameter to realize different devices and, furthermore, to verify if some mathematical trends can be defined between the fractional order of the capacitors and the CT itself. High CTs have been investigated considering both the manufacturer recommendations and the propagation of heat through the mold. As a consequence of the heat diffusion process, a stabilization period is required for the PDMS curing temperature to approach the imposed CT.
In details, the following curing temperatures and the stabilization periods (SPs) have been investigated:

- CT = 125 °C and SP = 38 min;
- CT = 140 °C and SP = 32 min;
- CT = 150 °C and SP = 28 min;
- CT = 160 °C and SP = 24 min.

Related to the CB, it is purchased from Alfa Aesar and used without further modifications. More specifically, the main properties of CB are now reported: acetylene, 100% compressed, 99.9+%, specific area 75 m^2/g, bulk density 170 g L^{-1} to 230 g L^{-1}, average particle size 0.042 µm.

Taking into account the polymeric matrix and the CB particles described above, the device implementation process is now presented.
The CB-based FOEs have been realized by mixing the PDMS and the crosslinking agent in a ratio of 10:1 in a Teflon crucible. The obtained compound has

been mixed for 10 min and, hence, the amount of CB required to achieve 8% concentration in mass has been added. Additionally, the mixture has been shuffled for further 10 min, with the aim of enhancing the CB dispersion inside the matrix. In conclusion, the mixture has been transferred into the devices and cured overnight. Once the devices have been stabilized, in each capacitor two copper wires have been soldered in order to employ it as standard bipole. In the Fig. 3.2A, the schematics of the polymeric dielectrics is drawn: it is possible to notice that the CB particles define small capacitors among them, defining a path through which the charges move from one electrode to the other one. The overall equivalent electric circuit (parallel RC groups network) is depicted in Fig. 3.2B. From the results of the previous chapter and taking into account the fractional-order approximation described in Sec. 1.2.2, the evidence of the fractional-order nature of this device is provided.

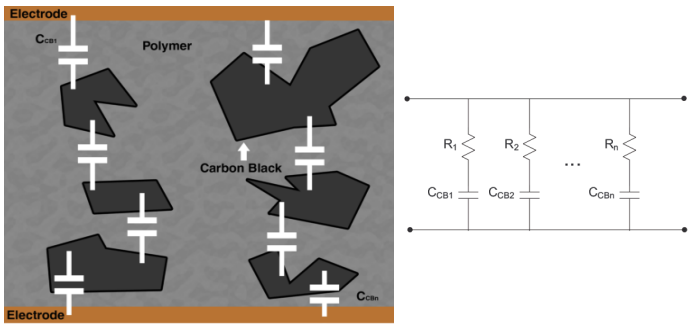

(A) Polymeric dielectrics (B) Equivalent Electric Circuit Model

FIGURE 3.2: Schematics and EECM of the CB-based FOE

The list of the realized FOEs with a CB percentage of 8% is reported in Tab. 3.1. However, it must be observed that other percentages and curing temperatures have been investigated without obtaining significant results. Only one device with a CB percentage of 2% a (CT of 130 °C and curing time of 36 min) exploits a fractional-order behaviour, as reported in Sec. 3.1.3. In conclusion, in Fig. 3.3 one of the realized CB-based FOE is reported.

FOE	**CB percentage**	**Curing Temperature**	**Curing Time**
C125	8%	125 °C	38 min
C140A	8%	140 °C	32 min
C140B	8%	140 °C	32 min
C150A	8%	150 °C	28 min
C150B	8%	150 °C	28 min
C160	8%	160 °C	24 min

TABLE 3.1: CB-based FOE with a CB percentage of 8%

FIGURE 3.3: CB-based FOE

In the next subsections, two different characterization procedure are described. In the first subsection, the realized devices are modelled as FOE, while in the second one, some of the CB-based devices are modelled as CPE in a smaller frequency domain.

3.1.2 FOE characterization

The devices reported in Tab. 3.1 have been investigated by measuring their impedance in a wide frequency range, from 0.01 Hz to 40 MHz with the Novocontrol Alpha-A high performance frequency analyzer. For each decade 10 points have been collected and measurements have been taken every 24 h.

The proposed impedance is reported in (3.1), where K is a gain, τ is the device time-constant and α is the fractional order.

$$Z(s) = \frac{K}{(1+\tau s)^{\alpha}} \tag{3.1}$$

Taking into account the frequency response of (3.1) and the measurements, the aforementioned unknown quantities have been identified by applying the Genetic Algorithms (GAs) [80], [81] with the following parameters:

- Population size: 4000;
- Generation number: 150;
- Generation gap: 0.9;
- Number of bit: 8

The cost function (CF) to minimize, represented with the symbol $\mathcal{J}$, takes into account both the magnitude and the phase response errors, computed between the real measurement Z_{real} and the simulated impedance Z_{sim}. The magnitude and phase errors, indicated as e_M and e_φ, are evaluated as follows:

$$e_M = \frac{\sum_i \left|20\log_{10}\left(Z_{real,i}\right) - 20\log_{10}\left(Z_{sim,i}\right)\right|}{N} \tag{3.2}$$

$$e_\varphi = \frac{\sum_i \left|\angle\left(Z_{real,i}\right) - \angle\left(Z_{sim,i}\right)\right|}{N} \tag{3.3}$$

where N is the number of recorded samples, i is the generic sample and $\angle(\cdot)$ evaluates the phase angle (in degree) of its argument. Hence, the CF is represented by:

$$\mathcal{J} = e_M + e_\varphi \tag{3.4}$$

For the sake of brevity, only the measured impedances for one device, C140B, are reported. See [79] for further details. The performed measurements and the simulated impedance are depicted in Fig. 3.4. It possible to notice that the magnitude slope of the equivalent model fits well the measurements, while some mismatch arises in the phase response, where a phase ripple of ± 5 deg can be observed up to 1 MHz. From that frequency, inductive parasitic effects occur: looking at the phase response, it exhibits a slope variation. The identified parameters $(\alpha;\, \tau\, K)$ for each device are reported in Tab. 3.2

FOE	α	τ	**K**	**Constant-phase range**
C125	0.724	2.7×10^{-3} s	0.163×10^{6}	1×10^{2} Hz to 1×10^{7} Hz
C140A	0.912	4081×10^{-3} s	3512×10^{6}	1×10^{2} Hz to 1×10^{7} Hz
C140B	0.955	$133\,918 \times 10^{-3}$ s	$60\,117 \times 10^{6}$	1×10^{2} Hz to 1×10^{4} Hz
C150A	0.854	97.8×10^{-3} s	19.5×10^{6}	1×10^{2} Hz to 1×10^{7} Hz
C150B	0.926	4887×10^{-3} s	1979.5×10^{6}	1×10^{1} Hz to 1×10^{7} Hz
C160B	0.898	$745\,845 \times 10^{-3}$ s	$141\,251 \times 10^{6}$	1×10^{1} Hz to 1×10^{7} Hz

TABLE 3.2: Parameters of the transfer function obtained by using the Bode diagram fitting

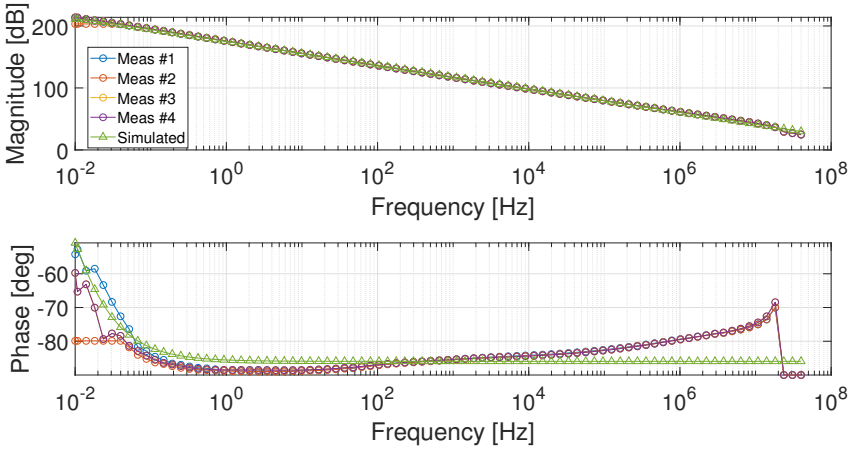

FIGURE 3.4: Bode diagrams for C140B - Comparison between performed measurements and simulated impedance

Finally, a comparison with the work conducted by Buscarino et al. [74] is made by analyzing the dependency of the α order over the curing temperature. Such a comparison is reported in Fig. 3.5. It seems that a transition between the two classes occurs when the curing temperature is among 125 °C and 140 °C.

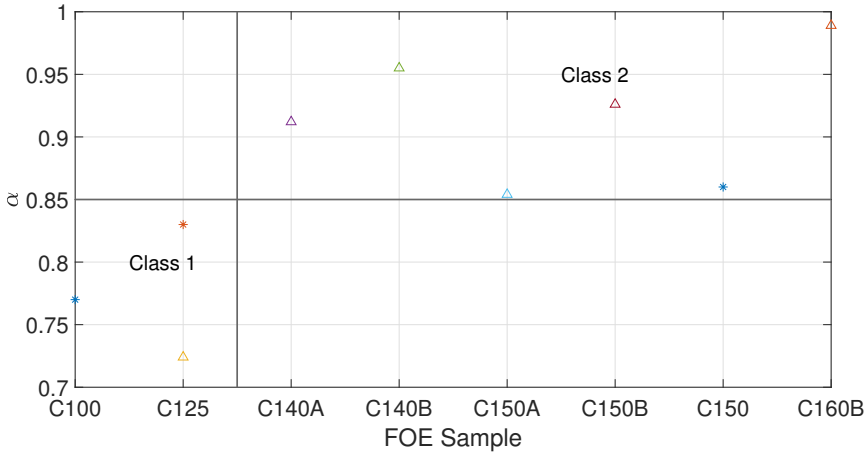

FIGURE 3.5: Comparison of α-order vs CT - Values with '*' are related to [74] devices, while '^' to [79].

3.1.3 CPE characterization

From all the realized devices with the technology presented in the previous section, two of them have been further investigated and modelled as CPEs in the 2019. The first one has a CB percentage equal to 8% with a curing temperature of 140 °C, while the other has a CB percentage of 2% and a curing temperature of 130 °C with a curing time of 36 min. They are labeled as *C140B* and *C130B*, respectively [82], [83].
Their magnitude and phase responses have been both measured with the Keysight Network Analyser E5061B by exploiting the fixture 16047E (here defined as "Gain-Phase port"), whose schematics is reported in Fig. 3.6. The instrument setup used during the measurement is the following:

- Logarithmic sweep in the range 5 Hz to 30×10^6 Hz;
- Intermediate Frequency Band Width (IFBW): 100 Hz;
- 201 points logarithmically distributed in the investigated domain;
- Averaging factor: 16.

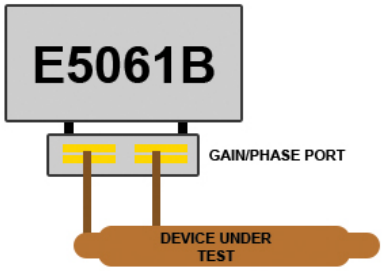

FIGURE 3.6: Schematics of the measurement with E5061B.

If not explicitly specified, the measurements are then filtered up to 1 MHz in order to avoid and exclude parasitic inductive effects. The screenshots of the measurements for the two devices are depicted in the next figures. Defining the range where their phase response is almost constant, both of them have been modelled as a CPE, whose impedance can be written as:

$$Z(s)_{CPE} = \frac{1}{Cs^{\alpha}} \tag{3.5}$$

FIGURE 3.7: Impedance measurement of C140B. Credits: [84]

FIGURE 3.8: Impedance measurement of C130B. Credits: [83]

Measurements have been identified by applying the GAs with the same setup parameters described in the previous section and the same CF (3.4), and the Bode diagram comparisons are reported in Fig. 3.9 and in Fig. 3.10, while their parameters are listed in Tab. 3.3. It can be observed that the devices have an α order of 0.81 (C140B) and 0.82 (C130B), with a Constant-Phase Zone of about 3 decades. They differ for the capacitance value, $2.7\,\mathrm{nFs}^{\alpha-1}$ for C140B, while $2.2\,\mathrm{nFs}^{\alpha-1}$ for C130B.

CPE	α	**C** $[\mathrm{Fs}^{\alpha-1}]$	**Constant-phase range**
C140B	0.81	$2.7 \times 10^{-9}\,\mathrm{Fs}^{\alpha-1}$	1 kHz to 1×10^{3} kHz
C130B [2019]	0.82	$2.2 \times 10^{-9}\,\mathrm{Fs}^{\alpha-1}$	1 kHz to 1×10^{3} kHz
C130B [2021]	0.85	$1.2 \times 10^{-9}\,\mathrm{Fs}^{\alpha-1}$	1 kHz to 1×10^{3} kHz

TABLE 3.3: Parameters of the investigated CPEs

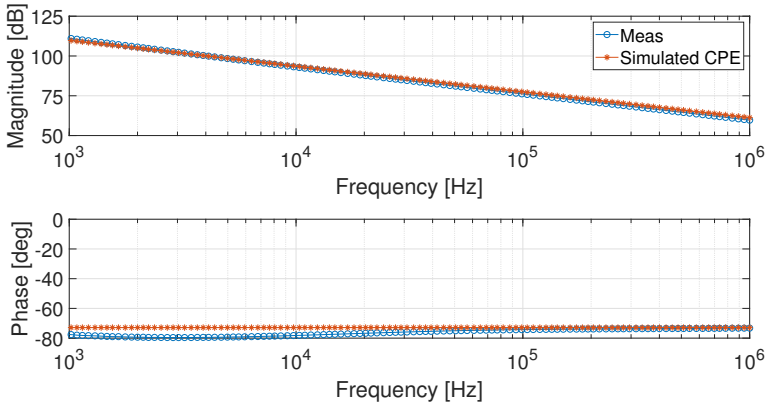

FIGURE 3.9: Comparison of Bode diagrams of measured impedance C140B and simulated model in the range 1 kHz and 1000 kHz.

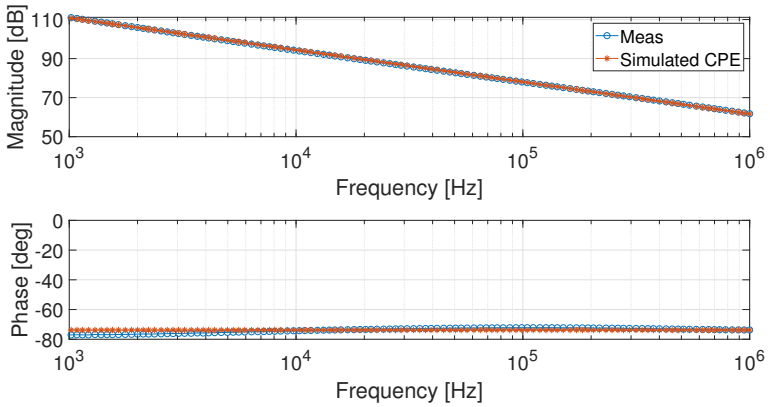

FIGURE 3.10: Comparison of Bode diagrams of measured impedance C130B and simulated model in the range 1 kHz and 1000 kHz.

Additionally, in Fig. 3.11 the error diagram (in absolute value) between measurement and simulated model for the C140B device is computed and reported. It can be detected a maximum magnitude error of about 1.5 dB, while a phase error of about 7 deg. Furthermore, also for the C130B the model error diagram is depicted in Fig. 3.12, where a maximum magnitude error of less than 0.5 dB and a maximum phase error of about 4 deg can be observed. The obtained errors, both for C140B and C130B, allow to validate the performed identification procedure.

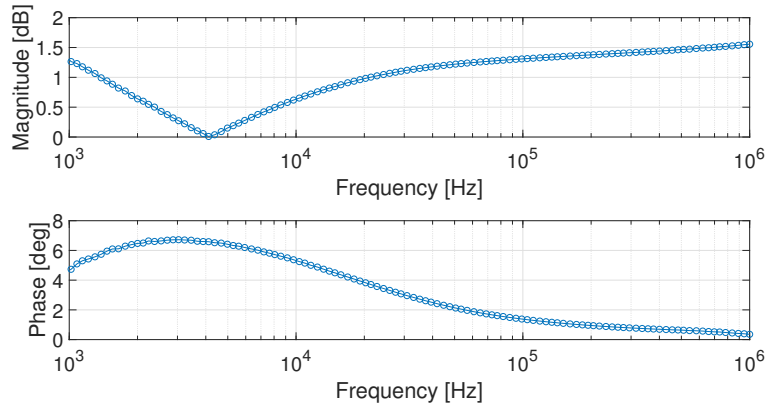

FIGURE 3.11: Bode diagram of C140B model error in the range 1 kHz and 1000 kHz.

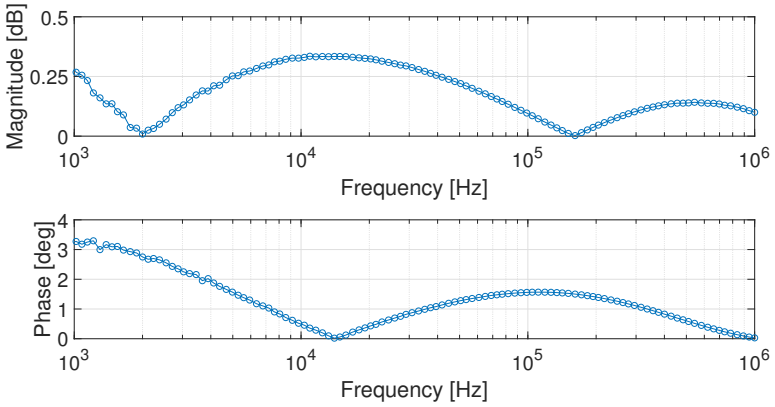

FIGURE 3.12: Bode diagram of C130B model error in the range 1 kHz and 1000 kHz.

Since their realizations, the devices have shown a robust stability. In particular, up to now in the 2021, the C140B does not show significant behaviour changes both in magnitude and in phase responses, allowing to employ it in several circuits without performing new identifications. On the other hand, the C130B has shown a slightly difference in its frequency response from its first application (RLC$^{\alpha}$ circuit) to the realization of a Fractional-Order Lead Compensator. The comparison of the Bode diagram from the response of 2019 and the one obtained in the 2021 are reported below. Identifying the new measurement, the new parameters are the following: $\alpha = 0.85$ and C $= 1.2\,\mathrm{nFs}^{\alpha-1}$. Therefore, a difference in the order of about 0.03 and a capacitance decreasing of $1\,\mathrm{nFs}^{\alpha-1}$ are measured. With the new model, a phase ripple of about ± 1 deg and a magnitude error of 1 dB can be measured. These parameters are also reported in Tab. 3.3.

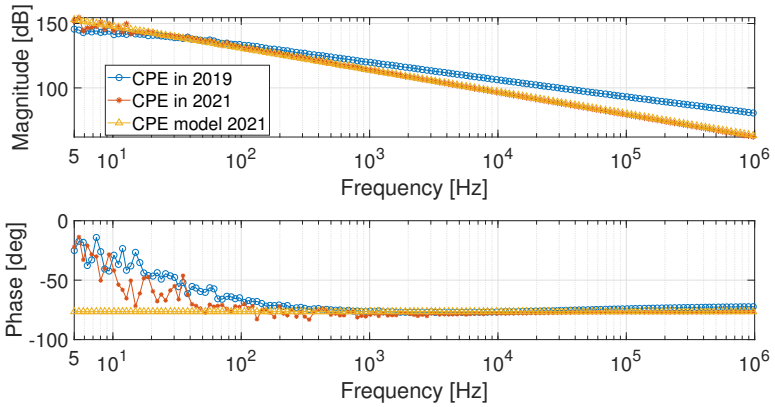

FIGURE 3.13: Comparison of Bode diagrams of C130B in the 2019 and 2021 and new simulated model in the range 5 Hz and 1×10^6 Hz.

In this following, the collection of all the realized circuits is reported and discussed in details. Each work is described in a proper subsection and the specific CB-based FOE exploited in the implementation is specified.

3.2 C140B applications

In this section, all the realized circuit implementations with the C140B will be presented. For each of them, none variations in the CPE parameters have been observed. Therefore, the values reported in Tab. 3.3 will be taken into account.

3.2.1 RC$^\alpha$ Circuit

The implementation of a FO-RC circuit has been treated in [82], [84]. In this application, both a passive and an active realization of the FO-filter are realized, whose schematics are reported in Fig. 3.14.

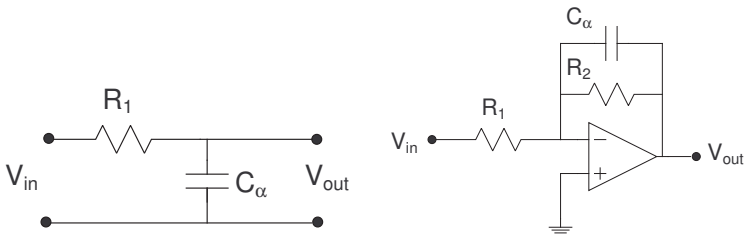

(A) Passive realization (B) Active realization

FIGURE 3.14: Schematics of passive and active RC$^\alpha$ circuits

The passive circuit has been realized with a resistor R = 100 kΩ and a non-inverting buffer output stage, while the active filter has been realized by exploiting the operational amplifier TL084 in an inverting integrator configuration with $R_1 = R_2 = 100\,k\Omega$ in order to have an unitary gain. This latter circuit is shown in Fig. 3.15 and its response is than inverted in post-processing, while in Fig. 3.16 the two responses are compared. The difference

of few mV shown between the passive and active filter responses is due to an offset of the operational amplifier.

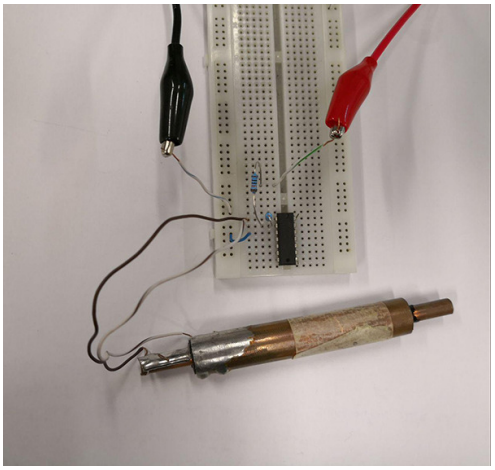

FIGURE 3.15: FO-RC active circuit implementation. Credits: [84]

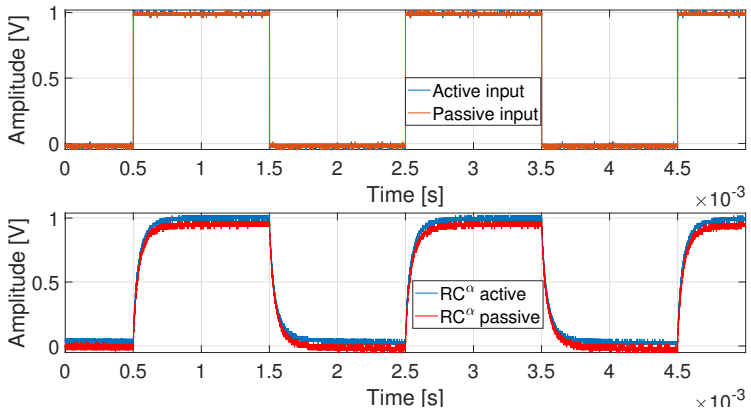

FIGURE 3.16: Comparison between passive and active FO-RC circuit output

In details, the response of the active circuit has been compared with the analytical solution of (3.6), which represents the differential equation of a FO-RC circuit of order α:

$$\frac{d^{\alpha}y(t)}{dt^{\alpha}} = -\frac{1}{RC}y(t) + \frac{1}{RC}u(t) \tag{3.6}$$

The equation has been integrated in MATLAB by using the procedure introduced in [85] with, as parameters, the C140B ones and R = 100 kΩ. The aforementioned comparison is reported in Fig. 3.17. The response allows to validate the identified parameters of the CPE, even if some steady-state error can be detected probably due to an operational amplifier attenuation or non-modelled parasitic effects.

Finally, a further comparison an integer-order RC filter has been conducted. A commercial capacitance of value C = 2 nF has been chosen in order to be as comparable as possible with the pseudocapacitance of the C140B. In Fig. 3.18 the two responses are drawn and it is possible to notice the effect of fractional-order derivative both in the transient, as well as in the steady state regime.

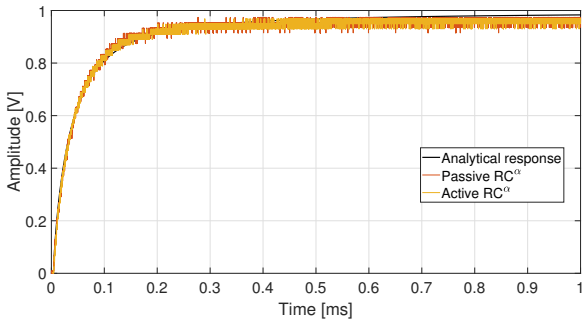

FIGURE 3.17: Comparison of the step responses between passive, active circuit implementations and the simulated one with (3.6).

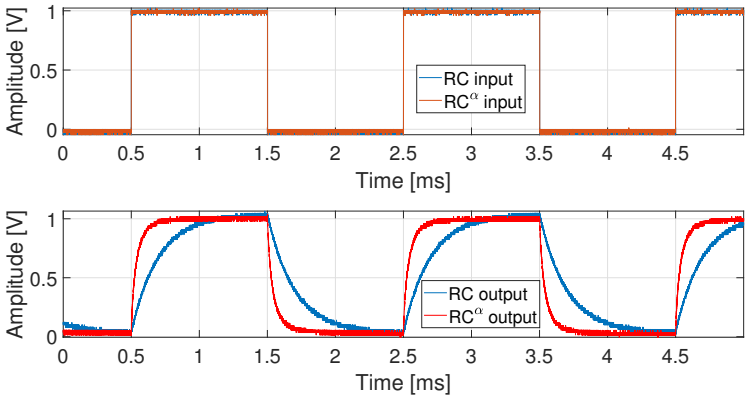

FIGURE 3.18: Step response comparison between IO-RC and FO-RC circuit implementations

3.2.2 Wien Oscillator

Generally, a system can act as oscillator if its order is greater or equal than two and if some nonlinearities are included in its governing equations. Such properties can be easily implemented in an analog system realization: the former by exploiting two state-space variables, i.e. two capacitors, the latter by implementing some nonlinearities, like the saturation of operational amplifiers. In [86], Radwan et al. have defined the general fractional-order Barkhausen oscillation conditions for systems with two or three state-space variables. Starting from these results, the possibility of implementing an analog FO-Wien oscillator has been treated in [84], [87].

Theoretical background

A general FO-Wien oscillator is depicted in Fig. 3.19, where both C_1 and C_2 are CPEs of orders α, $\beta \in \mathbb{R}$, respectively.

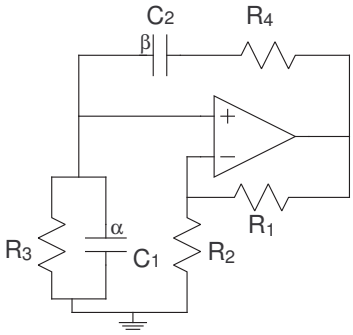

FIGURE 3.19: Fractional order Wien oscillator schematics.
Credits: [84]

Applying the Kirchhoff Voltage Law, the circuit equations, expressed with respect to the capacitor voltages V_{C_1} and V_{C_2}, are:

$$\begin{bmatrix} \frac{d^\alpha V_{C_1}}{dt^\alpha} \\ \frac{d^\beta V_{C_2}}{dt^\beta} \end{bmatrix} = \begin{bmatrix} \frac{a-1}{R_4 C_1} - \frac{1}{R_3 C_1} & -\frac{1}{R_4 C_1} \\ \frac{a-1}{R_4 C_2} & -\frac{1}{R_4 C_2} \end{bmatrix} \begin{bmatrix} V_{C_1} \\ V_{C_2} \end{bmatrix} + + \begin{bmatrix} \frac{b}{R_4 C_1} \\ \frac{b}{R_4 C_2} \end{bmatrix}, \tag{3.7}$$

where:

$$(a,b) = \begin{cases} (0, V_{sat}) & KV_{C_1} \geq V_{sat} \\ (K, 0) & -V_{sat} < KV_{C_1} < V_{sat} \\ (0, -V_{sat}) & -V_{sat} \geq KV_{C_1} \end{cases} \tag{3.8}$$

Equation (3.8) represents the circuit nonlinearity, which exploits the saturation of the operational amplifier: indeed, V_{sat} is the saturation voltage (i.e., the supply voltage). When the voltage across C_1 multiplied by the gain of the circuit ($K = 1 + R_1/R_2$) is greater than the saturation voltage, the values of the inputs change in order to restabilize the circuit. In the general case, where the passive components are different between each other and the Barkhausen oscillation conditions are satisfied, the oscillation pulsation ω of the circuit is:

$$\omega = \left(\frac{1}{R_3 R_4 C_1 C_2} \right)^{\frac{1}{\alpha + \beta}} \tag{3.9}$$

Taking into account the standard integer-order implementation of the Wien oscillator (i.e., by using same capacitors and same resistors), (3.9) can be simplified as $\omega = 1/\sqrt{RC}$. Observing the two expressions, it is easy to understand that having more degree of freedoms leads to the possibility of generate sinusoidal tones at very different frequencies covering, hence, a wide frequency domain. Furthermore, as Radwan et al. have demonstrated in [86], another important consequence is related to the stabilizing gain K. In the IO-Wien oscillator implementation, oscillations can be produced only if $K \geq 3$, while, in the general implementation, they have proven that the gain

Parameter	**Value**
α	0.81
C_1	$2.7\,\mathrm{nF/s^{1\,-\,\alpha}}$
β	1
C_2	1 nF
R_1	14.05 kΩ
R_2	33 kΩ
R_3	4.17 kΩ
R_4	0.78 kΩ
f	250 kHz
V_{cc}	± 7 V

TABLE 3.4: Component parameters for FO-Wien oscillator

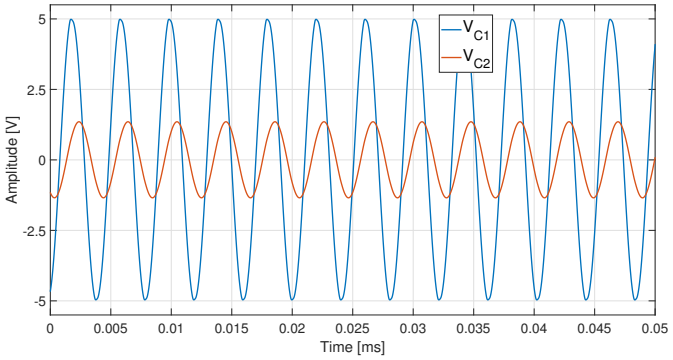

FIGURE 3.20: MATLAB simulation of FO-Wien oscillator state-space variables.

can assume also a smaller value.

Experimental setup

In this case study, both in simulation and real implementation design, the C140B parameters are considered. More specifically, exploiting the design procedure reported in [86], the circuit parameters of Fig. 3.19 are listed in the next table, taking into account that the C140B will be used as C_1 and the resistor R_2 has been arbitrary chosen. It must be observed that the design procedure is performed with the aim of generating a sinusoidal wave at 250 kHz: such a choice is led to the frequency domain where the C140B acts as a CPE.

Evaluating the gain of the circuit, that is mounted in a non-inverting configuration, it follows that $K = 1 + R_1/R_2 = 1.42$. As previously stated, this outcome demonstrates the possibility of having a gain less than three for a generic FO-Wien oscillator able to generate a sinusoidal tone. In the following, results on the proposed implementation are provided: firstly. the oscillator is completely simulated in MATLAB and, then, the circuit is physically realized and measurements are compared with the theoretical results. Simulations of the reported circuit have been performed in MATLAB, integrating (3.7) with the method proposed by Garrappa in [85]. Furthermore, an initial condition of 5 V has been fixed for each capacitor.

In Fig. 3.21, the discussed FO-Wien circuit is realized by exploiting a standard capacitor and the C140B. Considering both the simulation and the realized circuit, it can be observed that a FO-Wien oscillator can be implemented by employing only one CPE.

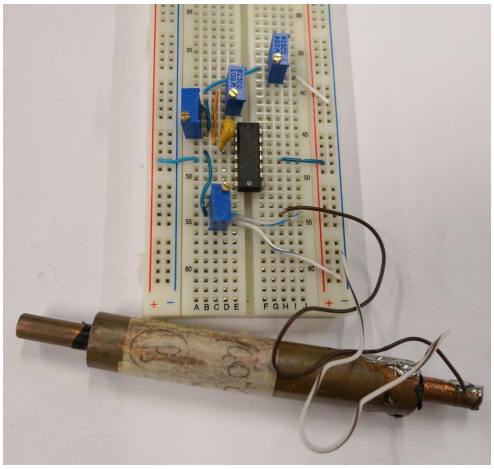

FIGURE 3.21: Fractional-order Wien oscillator realization.
Credits: [84]

During the experiment, it has been necessary to change some of the circuit parameters reported in Tab. 3.4 for slightly modifying the gain of the circuit to generate the oscillations. In particular, R_2 has been increased up to 35.8 kΩ in order to start the oscillations, obtaining a gain $K_{real} = 1.39$. Using the updated value of R_2 a sinusoidal tone at the desired frequency has been produced and reported in Fig. 3.22.

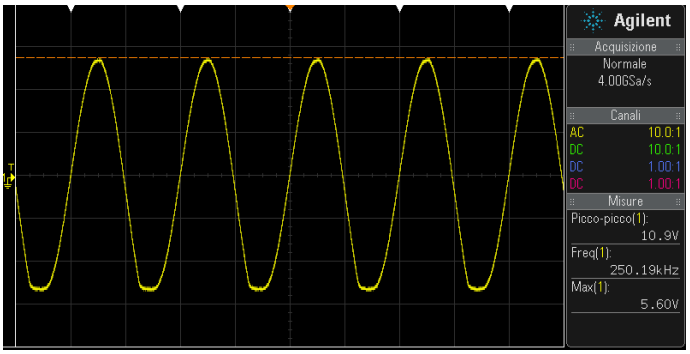

FIGURE 3.22: FO-Wien oscillator sinusoidal tone at 250 kHz measured across C140B.
Credits: [84]

Finally, the comparison between simulation and real experiment is provided and depicted in Fig. 3.23, both in the time and in the frequency domain. In the former, Fig. 3.23A, neglecting the phase-shift due to different starting point, a discrepancy in the signal amplitude can be detected, probably due to some non-modelled phenomena. In the latter, a Fast Fourier Transform of the two responses has been evaluated. The result depicted in Fig. 3.23B confirm that the implemented circuit oscillates at the desired frequency.

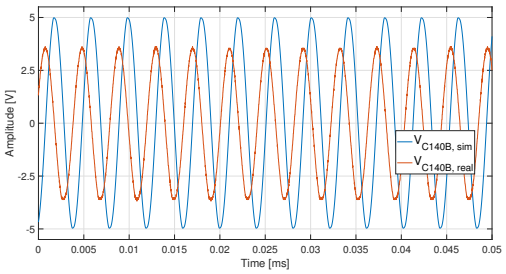

(A) Time domain

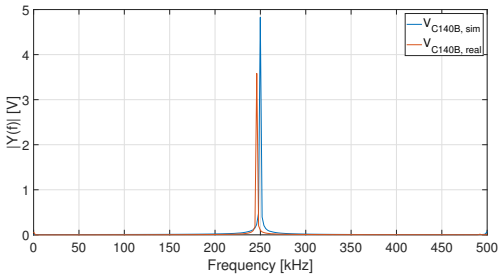

(B) Frequency domain

FIGURE 3.23: Comparison between simulated and real measurements of FO-Wien oscillator

3.2.3 Duffing Circuit

In this last C140B application, the possibility of exploiting chaotic behaviour from a FOS is investigated [84]. In particular, the C140B is used for implementing the governing equations of the Duffing system [88].

Theoretical background

The Duffing system is a second-order non linear system whose behaviour can vary from a canonical second-order system to oscillator or chaotic system accordingly to the provided input. Its governing equations are the following:

$$\begin{cases} \dfrac{dx}{dt} &= y \\ \dfrac{dy}{dt} &= x - x^3 - \delta y + \gamma \cos(\omega t) \end{cases} \tag{3.10}$$

Analysing (3.10), several considerations can be made. First of all, it is possible to realize them in an analog way by implementing a RLC circuit in sinusoidal regime. More specifically, the non-linearity is provided by employing a capacitor whose characteristic in the q-v plane has a cubic shape, as it can be noticed from the equation itself. Additionally, there are some free parameters, like δ, γ and the pulsation ω that can be thought as bifurcation parameters, i.e., those parameters that can change the dynamics of a system (from stable to bistable behaviour up to a chaotic one). In particular, if δ and γ are fixed and only the pulsation ω varies, it is possible to change the Duffing system behaviour, from a limit cycle to a chaotic attractor.

Strictly related to FOSs, several studies have been performed with the aim of demonstrating the feasibility of obtaining and controlling fractional-order chaotic systems, from Hartley et al. in the 1995 [89] to Petras in 2002 [90]. The two studies realized a FO-chaotic system by evaluating or the fractional-order derivatives of all the state-space equation or simply one state-space equation, respectively. In the reported study, only a fractional-order derivative is calculated and, then, the system is implemented with analog components.

Starting from (3.10), they can be rearranged in a fractional-order way by computing the FO-derivative of the x variable with a generic order $\alpha \in \mathbb{R}$: $0 < \alpha < 1$. This choice allows to easily implement the system by exploiting a CPE, because it represents the equation for a FO-integrator. In conclusion, the general equations for the FO-Duffing system are the following:

$$\begin{cases} \dfrac{d^{\alpha}x}{dt^{\alpha}} &= y \\ \dfrac{dy}{dt} &= x - x^3 - \delta y + \gamma \cos(\omega t) \end{cases} \tag{3.11}$$

It can be observed that the new order of the system is equal to $\alpha + 1 < 2$. Buscarino et al. [91] have already proved the possibility of obtaining a chaotic system even if its order is less than two, under the assumption that the system is properly excited. In details, they have implemented the FO-Duffing system by exploiting the Charef's approximation method, discussed in Sec. 1.2.2.

Experimental setup

In this study, the fractional-order integrator of the FO-Duffing system will be realized by exploiting the C140B: evaluating its fractional order, $\alpha = 0.81$, the implemented system will have an overall order equal to 1.81.

The first equation is implemented by exploiting a simple inverting integrator in series with an inverting configuration as reported in Fig. 3.24. In particular, the following parameters have been used: $R_1 = R_2 = 10\,k\Omega$ and R_3 is obtained with a trimmer, whose value has been fixed to $8.8\,k\Omega$.

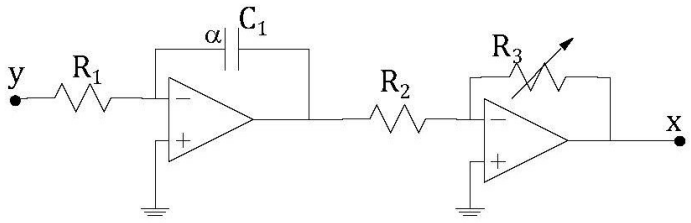

FIGURE 3.24: Implementation of FO-Duffing system first equation with the C140B.
Credits: [84]

Defining y of Fig. 3.24 as output of the first equation, the overall FO-Duffing system is reported in Fig. 3.25, where $R_f = 100\,k\Omega$, $R_y = 80\,k\Omega$, R $= 10\,k\Omega$ and C $= 10\,pF$.

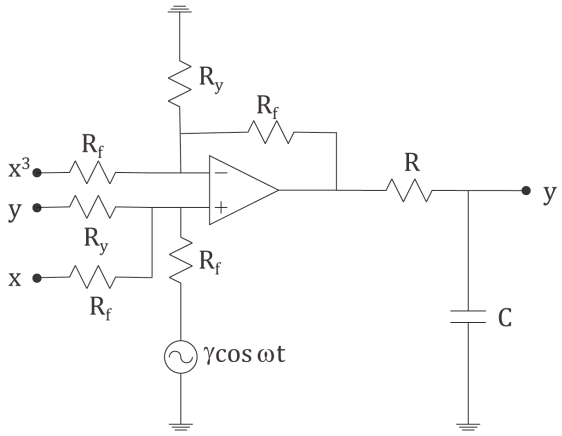

FIGURE 3.25: Implementation of FO-Duffing system second equation.
Credits: [84]

Considering the two schematics depicted in the previous figures, the FO-Duffing system has been implemented by using TL084 as operational amplifiers. A picture of the circuit is reported in Fig. 3.26.

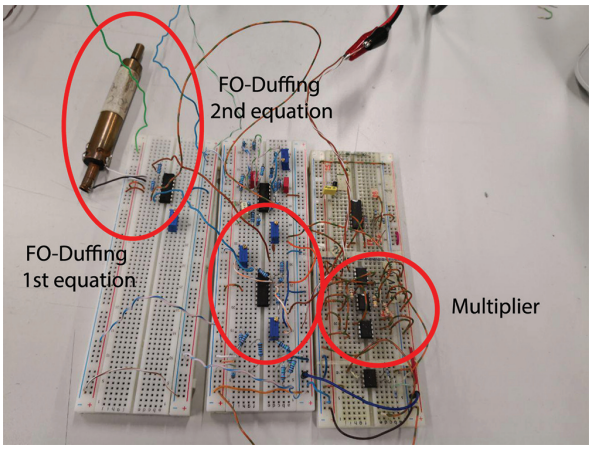

FIGURE 3.26: Circuit implementation of FO-Duffing System with C140B

In the first two breadboards, the schematics of Fig. 3.24 and Fig. 3.25 are implemented, respectively. A further conditioning circuit has been developed in the third breadboard in order to evaluate the cubic power of the first state-space variable. Such a circuit has been realized with two *AD-366* multipliers and two TL084. The schematics is reported in Fig. 3.27, where the following resistance have been used: $R_1 = R_2 = 10\,k\Omega$, $R_2 = R_4 = 100\,k\Omega$.

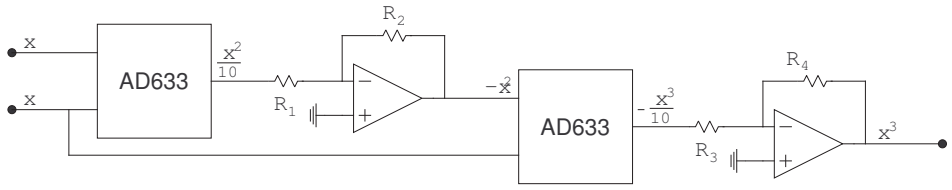

FIGURE 3.27: Analog realization of cubic multiplier.
Credits: [84]

The simulations have been performed by imposing, as input, a sinusoidal tone with a peak-to-peak amplitude of 4 V, whereas the frequency has been changed in order to investigate different system behaviour. Also in this case, the analysed frequencies belong to the range in which the C140B acts as CPE. In details, if the frequency is equal to 200 kHz a double-scroll-like shape is obtained, see Fig. 3.28A, while if it is increased up to 300 kHz a torus surrounding the attractor can be observed, Fig. 3.28B. Investigating higher frequencies, the aforementioned torus collapses into an internal limit cycle (frequency of 500 kHz) as reported in Fig. 3.29A. Finally, at a frequency of 800 kHz a stable attractor can be observed, Fig. 3.29B.

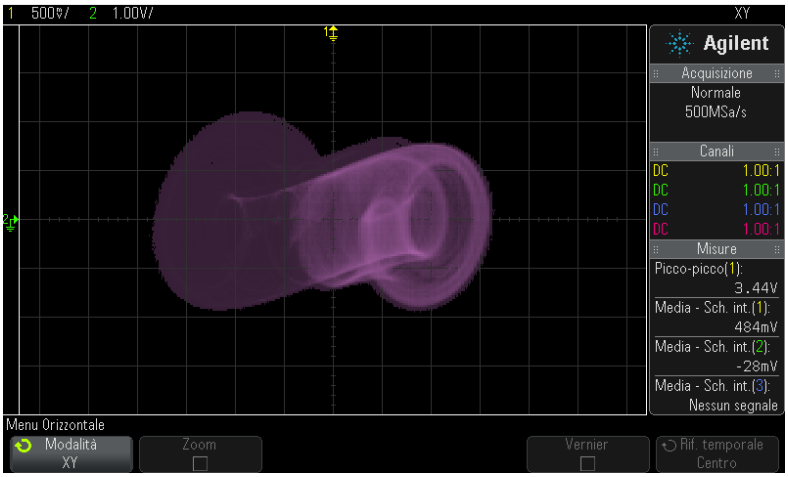

(A) 200 kHz

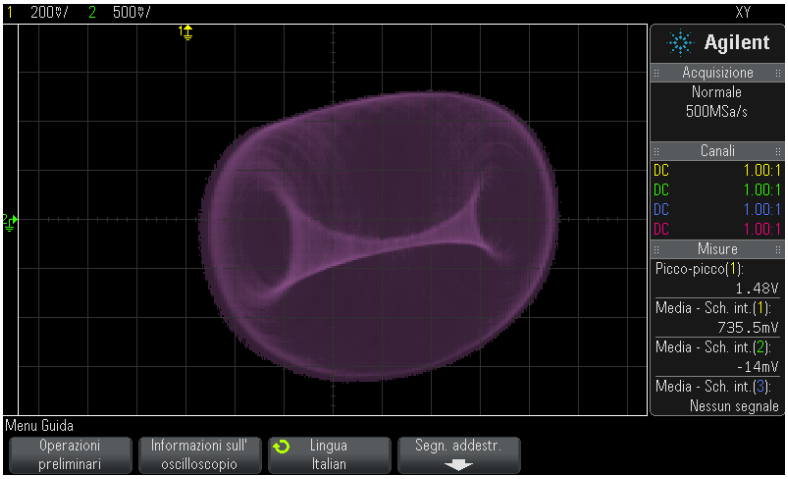

(B) 300 kHz

FIGURE 3.28: FO-Duffing system excited at 200 kHz and 300 kHz. Credits: [84]

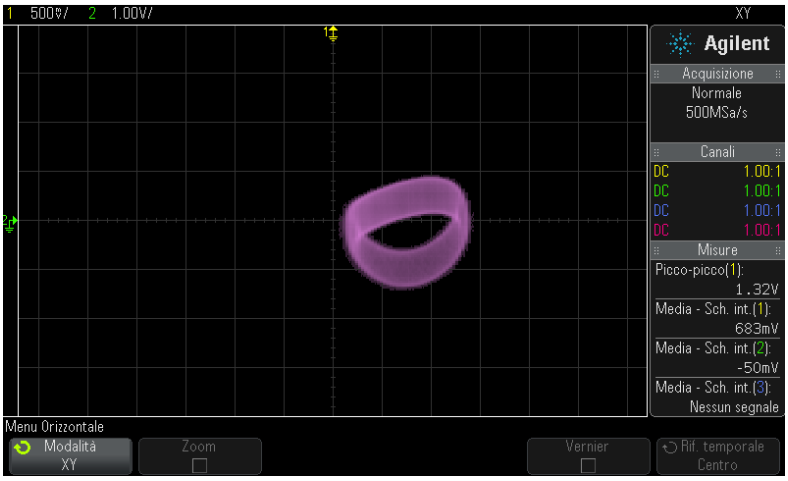

(A) 500 kHz

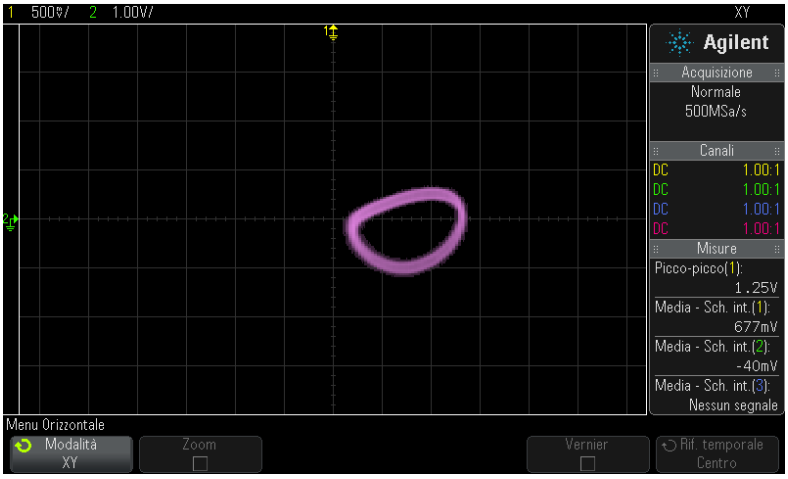

(B) 800 kHz

FIGURE 3.29: FO-Duffing system excited at 500 kHz and 800 kHz. Credits: [84]

3.3 C130B applications

In the following, the two circuit implementations with the C130B are described. In particular, these two applications have been realized in the 2020 and 2021. Therefore, considering the analysis conducted during the CPE characterization, the proper parameters have been used.

3.3.1 RLC$^{\alpha}$ Circuit

In the study performed in the 2020 [83], the possibility of implementing an analog FO-RLC has been investigated by employing the C130B. The discussion of this study will be divided into two main steps: in the first one, some theoretical aspects will be analyzed while, in the second stage, the experimental results will be provided.

Theoretical background

Several studies have been conducted for the realization of FO-RLC circuits, like Gòmez et al. in 2013 [92] or Radwan et al. in 2013 [93]. In all these studies, different aspects are analyzed, such as optimization or design techniques, but none of them exploits directly an analog CPE for the circuit implementation.

The schematic of a passive FO-RLC series circuit is reported in Fig. 3.30. Easily, it can be observed that if $\alpha = \beta = 1$, the standard RLC circuit is obtained.

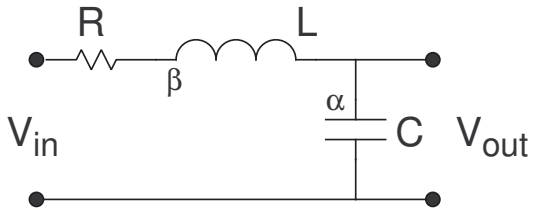

FIGURE 3.30: FO-RLC series schematics.
Credits: [83]

Generally, defining $i(t)$ as the flowing current in the circuit, the fractional-order inductor and capacitor equations can be formulated as follows:

$$V_L(t) = L\frac{d^\beta}{dt^\beta}\left[i(t)\right], \qquad i(t) = C\frac{d^\alpha}{dt^\alpha}\left[V_C(t)\right] \tag{3.12}$$

Therefore, the circuit voltage equation is:

$$LC\frac{d^\beta}{dt^\beta}\left(\frac{d^\alpha V_c(t)}{dt^\alpha}\right) + RC\frac{d^\alpha V_c(t)}{dt^\alpha} + V_c(t) - V_{in}(t) = 0 \tag{3.13}$$

Applying the chain-rule presented in the first chapter, i.e. $\mathcal{D}^\alpha\left[\mathcal{D}^\beta f(t)\right] = \mathcal{D}^{\alpha+\beta}\left[f(t)\right]$, (3.13) can be rearranged:

$$LC\frac{d^{\alpha+\beta}V_c(t)}{dt^{\alpha+\beta}} + RC\frac{d^\alpha V_c(t)}{dt^\alpha} + V_c(t) - V_{in}(t) = 0 \tag{3.14}$$

In the time domain, the governing equations of the circuit can be defined as:

$$\begin{aligned} \frac{d^\alpha x_1(t)}{dt^\alpha} &= x_2(t) \\ \frac{dx_2(t)}{dt} &= -\frac{1}{LC}x_1(t) - \frac{R}{L}x_2(t) + \frac{1}{LC}V_{in}(t) \end{aligned} \tag{3.15}$$

where $x_1 = V_c(t)$ and $x_2(t) = \mathcal{D}^\alpha\left[V_C\right]$.

Evaluating (3.14) and applying the Laplace transform, it is possible to study the behaviour of the system in the frequency domain. Indeed, the overall transfer function is:

$$G(s) = \frac{V_c(s)}{V_{in}(s)} = \frac{1}{LCs^{\alpha+\beta} + RCs^\alpha + 1} \tag{3.16}$$

According to Radwan et al. [93], it is possible to evaluate the resonance pulsation ω_r:

$$\omega_r = \left[\frac{\sin\left(\frac{\alpha\pi}{2}\right)}{LC\sin\left(\frac{\beta\pi}{2}\right)} \right]^{\frac{1}{\alpha+\beta}} \tag{3.17}$$

Also in this scenario, the standard integer-order resonance pulsation $\omega_r = 1/\sqrt{LC}$ is obtained simply imposing $\alpha = \beta = 1$.

Among the properties defined in the cited works, the asymptotic phase value Φ_{as} has been computed. By putting $s = j\omega$, the general expression of the asymptotic phase lag can be defined:

$$\begin{aligned} G(j\omega) &= \frac{1}{LC\cdot(j\omega)^{\alpha+\beta} + RC\cdot(j\omega)^{\alpha} + 1} = \frac{N(j\omega)}{D(j\omega)} \rightarrow \\ \angle\left[G(j\omega)\right] &= \angle\left[N(j\omega)\right] - \angle\left[D(j\omega)\right] = -\angle\left[D(j\omega)\right] \end{aligned} \tag{3.18}$$

Using the Euler formula, i.e., $(j\omega)^{\alpha} = \omega^{\alpha}\left[\cos\left(\alpha\pi/2\right) + j\sin\left(\alpha\pi/2\right)\right]$, the following expression holds:

$$\begin{aligned} &\angle D(j\omega) = \\ &= \arctan \frac{\omega^{\alpha}\left[LC\omega^{\beta}\sin\left((\alpha+\beta)\frac{\pi}{2}\right) + RC\sin\left(\alpha\frac{\pi}{2}\right)\right]}{LC\omega^{\alpha+\beta}\cos\left((\alpha+\beta)\frac{\pi}{2}\right) + RC\omega^{\alpha}\cos\left(\alpha\frac{\pi}{2}\right) + 1} \end{aligned} \tag{3.19}$$

The asymptotic phase value, Φ_{as}, can be evaluated from (3.19) by applying the limit infinity order comparison:

$$\Phi_{as} = -\lim_{\omega\rightarrow+\infty} \angle D(j\omega) = -\left(\alpha+\beta\right)\frac{\pi}{2} \tag{3.20}$$

In the next subsection, both the simulated and real measurements are presented. In details, the simulations are performed by exploiting the FOMCON toolbox developed by Tepljakov et al. [94].

FO-RLC model validation

The experimental circuit is reported in Fig. 3.31, where the resistance has been fixed to 1 kΩ and the inductance to 47 mH. The C140B parameters used in this experiment are: $\alpha = 0.82$ and $\mathrm{C} = 2.2\,\mathrm{nF/s}^{1-\alpha}$.

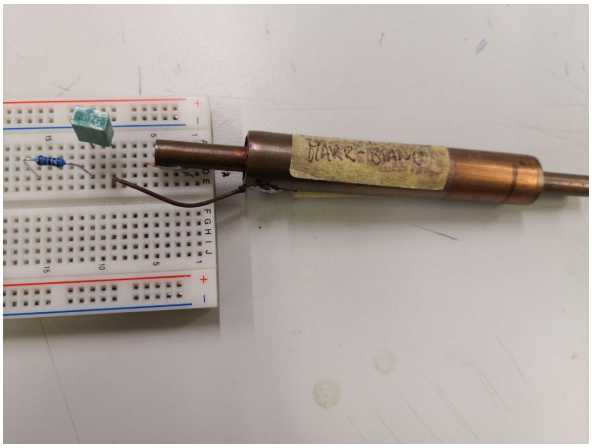

FIGURE 3.31: FO-RLC circuit implementation.
Credits: [83]

Starting from the nominal FO-RLC model, a comparison between the theoretical and the real frequency responses of the system under investigation is performed in the range 1 kHz to 1×10^3 kHz and reported in Fig. 3.32. The frequency response of the real model has been taken with the already presented network analyzer E5061B. It is possible to notice that some non-modelled parasitic phenomena occur at high frequencies. For such a reason, the passive components have been further investigated.

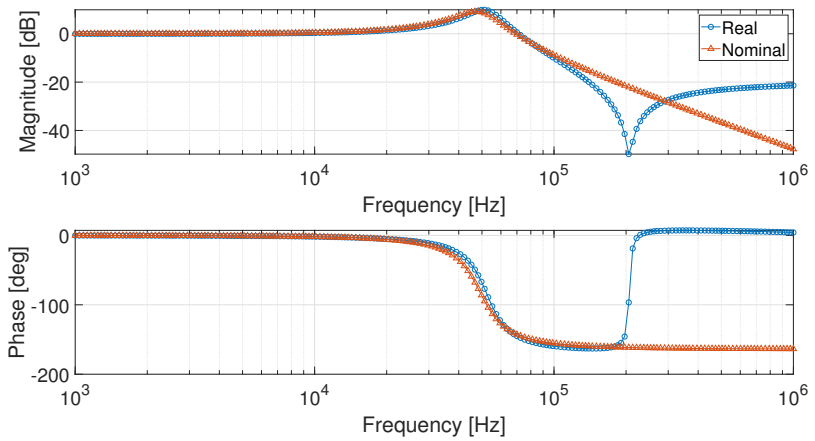

FIGURE 3.32: Bode diagrams of the nominal FO-RLC model and the implemented circuit.
Credits: [83]

Regarding the resistor, its real value has been measured with a multimeter and a value of 997.8 Ω has been detected and considered in the following. Instead, regarding the inductor, its frequency response has been evaluated in the analysed range. From Fig. 3.33 a resonant peak at high frequencies (about 250 kHz) is not modelled from the ideal model, reported with circular markers. Hence, the complete model of the inductor, see Fig. 3.34, has to be taken into account. The inductor Equivalent Electric Circuit Model (EECM) parameters have been identified by applying the GAs with the same CF described in (3.4) and their values are listed in Tab. 3.5.

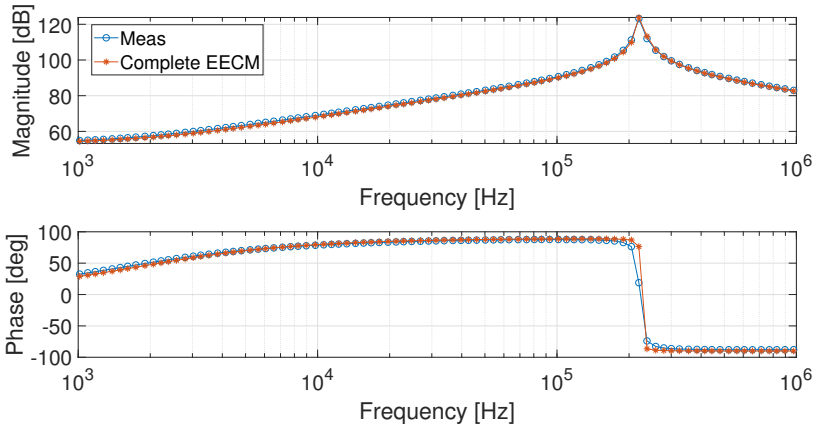

FIGURE 3.33: Bode diagrams of the inductor and its EECM

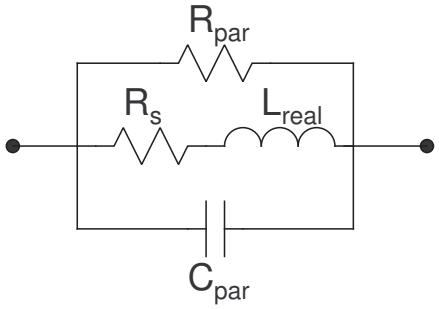

FIGURE 3.34: Inductor EECM.
Credits: [83]

Parameter	**Value**
R_{par}	15.874 GΩ
C_{par}	12.707 pF
R_s	0.459 kΩ
L_{real}	39.8 mH

TABLE 3.5: Parameters of the inductor EECM

Finally, in Fig. 3.35 the Bode diagrams comparison between the complete FO-RLC model and the real implementation is drawn. It highlights the completeness of the model, giving the possibility to perform more accurate simulations. Furthermore, Fig. 3.35 allows to validate the identified order α of the C130B because the asymptotic phase lag value is almost equal to the one of the simulated model.

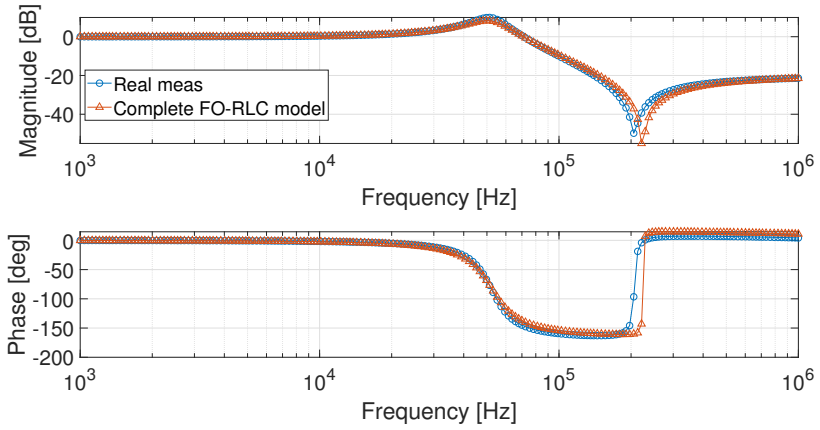

FIGURE 3.35: Bode diagrams of the real FO-RLC circuit and the complete equivalent model

Results

The realized FO-RLC circuit exhibits a resonance behaviour, as Fig. 3.35 confirms: indeed, the resonance peak occurs at about 50 kHz, while a pseudo-anti-resonant peak occur at about 250 kHz due to the parasitic effects of the inductor that has been modelled in previous section. All the acting parasitic effects determine some discrepancies that can be observed both in module and in phase responses. Their deviations have been computed and reported in Tab. 3.6.

Deviation	**Value**	**Frequency**
Module	1.704 dB	51.286 kHz
Phase	8.289 deg	63.648 kHz

TABLE 3.6: Maximum deviation values

Taking into account these parasitic effects, the analysis of the implemented circuit is restricted up to 100 kHz. Both the frequency and the time domain responses are studied and discussed.

The sinusoidal regime has been studied by testing three different frequencies in the second decade of the reported Bode diagram: 10 kHz for exploring the circuit behaviour at low frequencies, 50 kHz for investigating the performances near the resonance frequency, while 100 kHz for defining the high frequencies behaviour. Both real and simulated responses at the aforementioned frequencies are reported in Fig. 3.36. The simulations at the lowest and the highest investigated frequencies confirm the experimental frequency response of the FO-RLC circuit and no difference can be detected. On the other hand, the simulation and the real responses highlight a discrepancy at 50 kHz. Considering the Bode diagrams of Fig. 3.35 and the maximum deviations computed and reported in Tab. 3.6, a module error of about 2 dB is measured. Therefore, the variation of about 0.2 V detected in Fig. 3.36C justifies such a discrepancy.

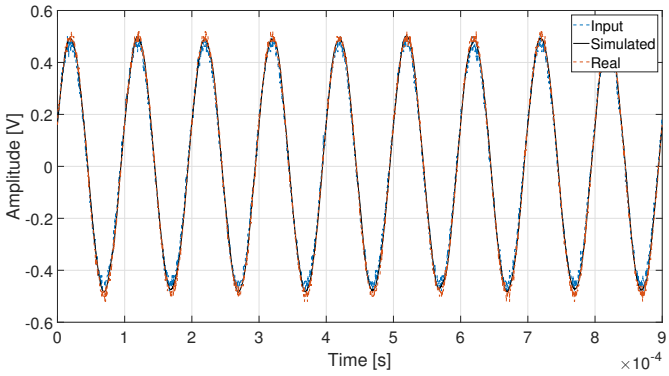

(A) 10 kHz

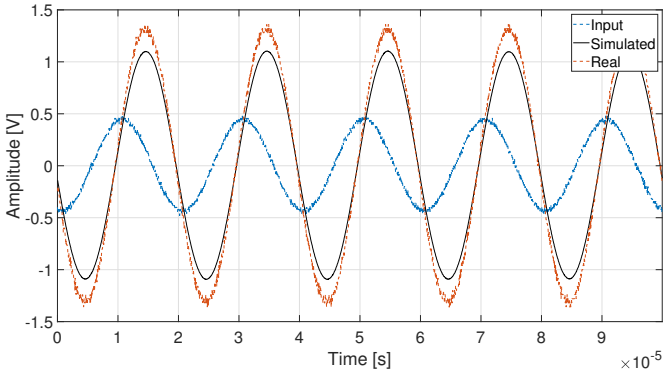

(B) 50 kHz

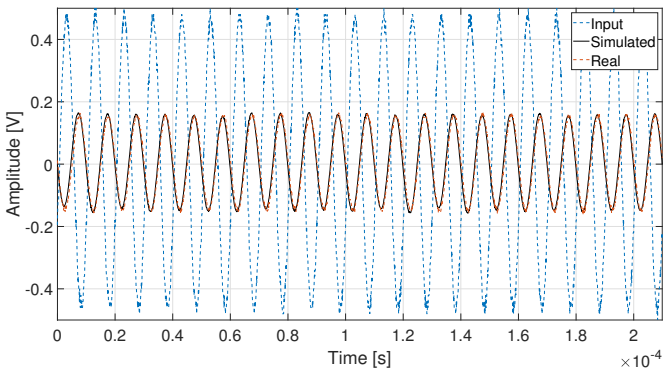

(C) 100 kHz

FIGURE 3.36: Sinusoidal simulations of FO-RLC at different frequencies. Credits: [83]

Regarding the time-domain analysis, the step response has been also investigated and depicted in Fig. 3.37. The pseudo-period of both real and simulated responses are almost equal, even if the real response is less dumped than the simulated one. Also in this case, this discrepancy can be justified by the deviation in the module response between the real circuit implementation and the corresponding model.

Estimated for / **Bode diagram**	**IO**	**FO-S**	**FO-R**
Resonance peak	10.1 dB	8.4 dB	9.9 dB
Resonance frequency	15.2 kHz	46.7 kHz	51.3 kHz
Module slope	-40 dB/dec	-38 dB/dec	//
Asymptotic phase value	-180 deg	-163.8 deg	-163 deg
Sine response			
Amplitude peak-to-peak @ 10 kHz	1.462 V	0.975 V	1 V
Amplitude peak-to-peak @ 50 kHz	0.122 V	2.195 V	2.64 V
Amplitude peak-to-peak @ 100 kHz	0.024 V	0.313 V	0.3 V
Step response			
Rise time	1.128×10^{-5} s	4.3×10^{-6} s	4.3×10^{-5} s
98% *Settling time*	2.138×10^{-4} s	1.032×10^{-4} s	1.104×10^{-4} s
Overshoot	58%	37%	50%

TABLE 3.7: Parameters for different computed responses

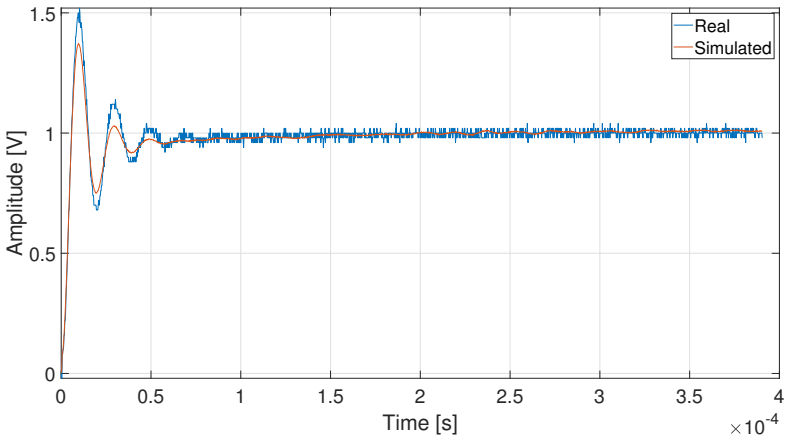

FIGURE 3.37: FO-RLC step response.
Credits: [83]

In conclusion, different response features (both in the sinusoidal regime and in the time domain) are listed in Tab. 3.7 for the FO-RLC circuit implementation and the equivalent model. Furthermore, the aforementioned parameters are also computed for the integer-order RLC circuit counterpart by exploiting the same resistance, inductance and capacitance values with $\alpha = 1$. It must be highlighted that, in this final comparison, the parasitic effects of the inductor are neglected. The following notation has been adopted: *IO* indicates the integer-order RLC circuit, *FO-S* is used for the simulated FO-RLC circuit, and *FO-R* for the implemented FO-RLC circuit.

Results reported in the table give evidence of the fractional-order nature of the implemented circuit. Furthermore, the values for the real FO-RLC implementation are in agreement with the analytical model, confirming the applied model goodness of fitting in the investigated frequency range.

3.3.2 Fractional-Order Lead Compensator

In this application, a Fractional-Order Lead Compensator (FOLC) is physically realized by means of the C130B. As mentioned in the previous section, the CPE parameters are changed from its original characterization. The following parameters will be used in this experiment: $\alpha = 0.85$, $\mathrm{C} = 1.2\,\mathrm{nFs}^{\alpha-1}$.

The objective of this study is to design and implement a robust controller for the following second-order system:

$$P(s) = \frac{k}{(1+\tau_1 s)(1+\tau_2 s)} \tag{3.21}$$

where $k = 1000$, $\tau_1 = 2.4 \times 10^{-3}\,\mathrm{s}$ and $\tau_2 = 0.8 \times 10^{-3}\,\mathrm{s}$. The constraints for the controller design are:

- desired crossover pulsation $\omega_{t,des} = 2\pi \cdot 4 \cdot 10^3\ \mathrm{rad\,s^{-1}}$;
- required phase margin $M_\varphi = 60$ deg;
- gain and pole variation rejection in the frequency range 1 kHz to 10 kHz.

The synthesis of the controller will be performed in the frequency domain. Its corresponding Bode diagram is reported in Fig. 3.38.

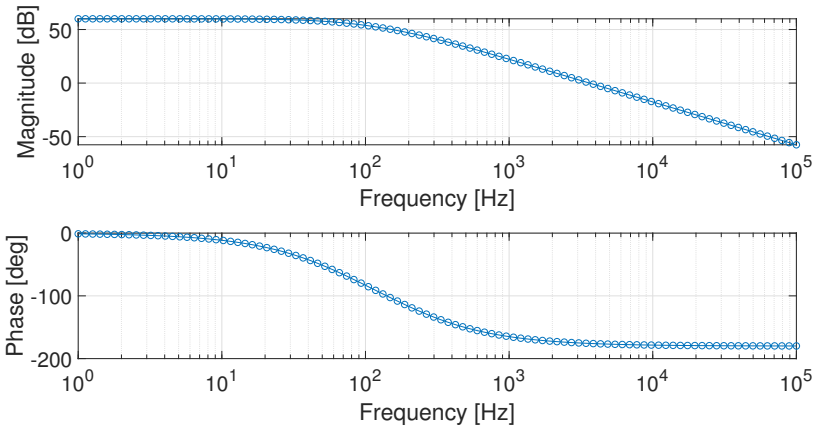

FIGURE 3.38: Bode response of the system plant to be controlled

It can be observed that the pulsation of the system is more or less the same, while it is required a phase lead of about 60 deg. According to Sec. 1.3, in order to avoid gain or pole variation rejection, it is required that the controller should be of fractional order because it is able to provide a flat phase in the desired crossover frequency neighbourhood.

Design procedure

The FOLC transfer function that will be considered in the following is:

$$C(s) = K_C \frac{\tau_z s^\alpha + 1}{\tau_p s^\alpha + 1} \tag{3.22}$$

As stated in Sec. 1.3, (3.22) is the transfer function for the active realization of a FOLC. The regulator parameters have been defined by a frequency

domain design procedure. In particular, the FO α has been put equal to the α-order of the C130B device. On the other hand, the pole and zero of the controller have been chosen in order to fulfill both the crossover frequency $\omega_{t,des}$ and the phase margin M_φ specifications. Furthermore, the tuning procedure has been performed by finding the values of τ_z and τ_p such that the phase response of the open-loop system (i.e., $C(s)P(s)$) is constant for all the frequencies of the decade in which the crossover frequency belongs. In particular, the exploited parameters are listed in Tab. 3.8, while the Bode diagrams of the plant and the overall open-loop system are depicted in Fig. 3.39. With these identified parameters, it is possible to notice that the phase response is constant at about -120 deg from 1 kHz to 10 kHz, providing a phase margin of $\sim$60 deg while, looking at the magnitude response, it can be noticed that the desired crossover frequency is at about 4 kHz, satisfying both the imposed constraints.

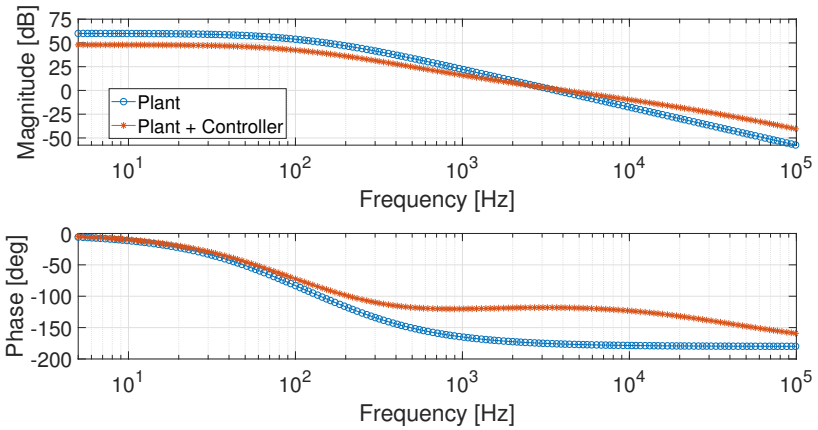

FIGURE 3.39: Bode diagrams of the plant and the open-loop system

Parameter	**Value**
K_C	0.25
τ_z $[\mathrm{s}^{1/\alpha}]$	0.0889×10^{-2}
τ_p $[\mathrm{s}^{1/\alpha}]$	0.2667×10^{-4}

TABLE 3.8: Parameters of $C(s)$

To test the validity of the proposed controller, the open-loop system is closed with an unitary feedback. Therefore, its robustness towards pole and gain variations are investigated. Furthermore, the comparison with the IO-compensator is performed by taking into account the parameters of Tab. 3.8 and setting $\alpha = 1$ in order to understand the main role of the fractional-order α.

Gain variation: To provide significant proofs for the *isodamping property*, the gain k of the plant has been varied from its nominal value in order to test the controller robustness. In particular, the gain has been changed from 800 up to 2000 with a step of 100. The nominal gain, both for the FO- and the IO-compensator, has been marked with circles. For each variation, the step response has been computed and results are reported in Fig. 3.40, where on

the left side the FO-closed-loop system responses are depicted, while on the right side the IO ones.

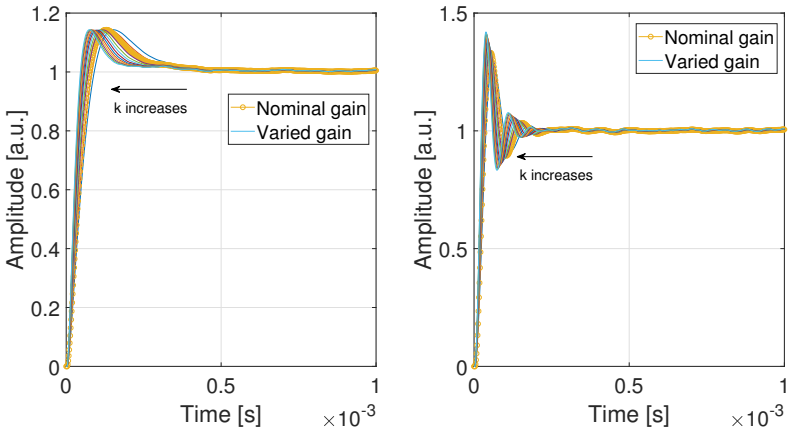

FIGURE 3.40: FO- (left) and IO-closed-loop systems (right) responses for different gain

Employing the FO-compensator, the closed-loop system maintains the same overshoot despite of the gain variation, even when the plant gain has been doubled from its nominal value. Additionally, the bigger the gain, the smaller the rising time: increasing the gain of the plant, the crossover frequency of the plant increases as well. Therefore, the system is faster.

On the other hand, the IO-regulator determines a less dumped response and, besides, the overshoot increases when the gain increases too. In conclusion, the IO-compensator is not able to maintain the same overshoot if the gain varies, while this property is easily achieved by the FO-controller.

τ_1 variation: In this paragraph, the variation of the first pole will be investigated. More specifically, the first time constant τ_1, whose nominal value is equal to $2.4 \times 10^{-3}\,\mathrm{s}^{1/\alpha}$, has been varied with a step of 0.1×10^{-3} from $1 \times 10^{-3}\,\mathrm{s}^{1/\alpha}$ to $4 \times 10^{-3}\,\mathrm{s}^{1/\alpha}$: by changing this value, the crossover frequency of the open-loop system decreases from 7 kHz to about 2 kHz, covering, hence, a greater frequency variation. In this way, the pole variation moves the crossover frequency inside the constant-phase zone. The comparison of the responses are reported in Fig. 3.41.

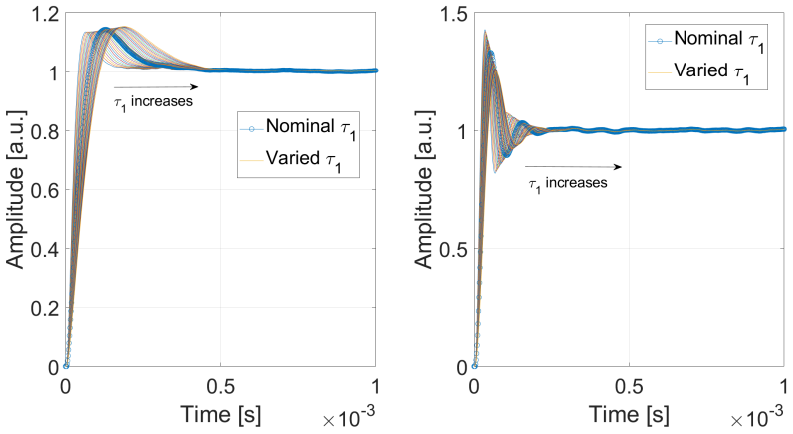

FIGURE 3.41: FO- (left) and IO-closed-loop systems (right) responses for different τ_1

Also in this case, the FO-closed-system responses are more stable and less affected by the pole variation: there is an increasing of the rising time when τ_1 increases, but the overshoot changes of about $\pm$ 1% for the minimum and maximum investigated τ_1 values, respectively. On the contrary, the IO-closed-loop system responses are less robust, as it can be noticed by the overshoot variation and also by the pseudo-period of the oscillations.

τ_2 variation: In this last paragraph, the variation of τ_2 will be studied. The time constant, whose nominal value is $0.8 \times 10^{-3}\,\mathrm{s}^{1/\alpha}$, has been varied from $0.4 \times 10^{-3}\,\mathrm{s}^{1/\alpha}$ to $1.6 \times 10^{-3}\,\mathrm{s}^{1/\alpha}$. Obtained step responses are drawn in Fig. 3.42.

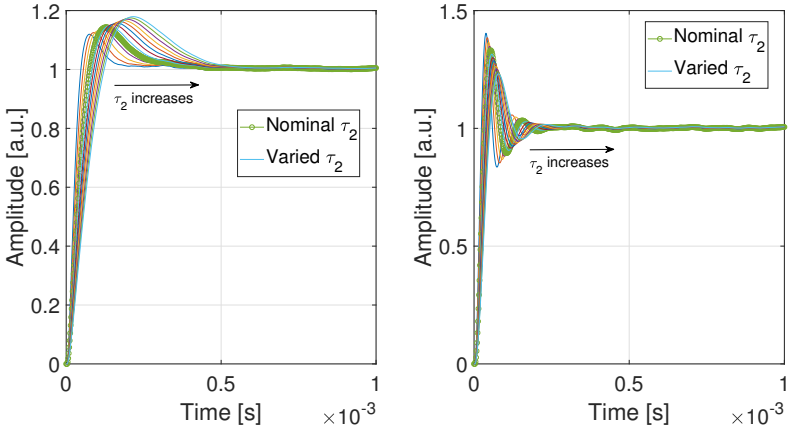

FIGURE 3.42: FO- (left) and IO-closed-loop systems (right) responses for different τ_2

Although the crossover frequency is in the constant-phase zone of the open-loop system, due to the position of τ_1, the system seems less robust towards τ_2 changes: an overshoot variation of about $\pm$4% can be detected. Nevertheless, the FO-response does not show significant variations from the nominal one and, additionally, none pseudo-oscillations like the IO-counterpart arise.

Experimental setup

In this section, the experimental setup of the entire control loop will be described. In each paragraph, the tuning procedure of the analog configuration will be compared with its simulated counterpart, in order to check if there any mismatched with the reported simulation analyzed before.

Controller: The controller has been implemented taking into account the schematics of Fig. 1.3, tuning the resistor values in order to have the parameters reported in Tab. 3.8 according to the following expressions,

$$\begin{aligned} \tau_z &= (R_1 C)^{1/\alpha} \\ \tau_p &= \left(\frac{R_1 \cdot R_2}{R_1 + R_2} \cdot C \right)^{1/\alpha} \\ k &= \left(1 + \frac{R_3}{R_4} \right) \cdot \frac{R_2}{R_1 + R_2} \end{aligned}$$

The related parameters are, then, listed in Tab. 3.9, while the obtained transfer function, labelled as $C_a(s)$, is evaluated in (3.23).

Parameter	**Value**
R_1 [kΩ]	748
R_2 [kΩ]	22
R_3 [kΩ]	1
R_4 [kΩ]	7

TABLE 3.9: Resistance values for the analog implementation of $C(s)$

$$C_a(s) = \frac{8s^{0.85} + 8912.7}{s^{0.85} + 38993} \tag{3.23}$$

The controller has been implemented by using a LT1007 operational amplifier, as shown in the red shape inside Fig. 3.43A . Furthermore, to assure the fairness circuit implementation, its frequency response has been measured with the E5061B from 5 Hz to 1×10^5 Hz, whose electrical connections are shown in Fig. 3.43B.

The frequency responses of the nominal controller $C(s)$, the tuned one $C_a(s)$ and the real circuit implementation are show in in Fig. 3.44. The tuned controller is slightly different in the magnitude response of less 1 dB with respect to the nominal one, while no significant difference can be detect in the phase response. The real controller Bode diagram is almost identical to the tuned one up to 10 kHz, validating the implementation of the regulator. Furthermore, the real compensator suffers of parasitic effects at high frequencies, as the phase response slope changes from 10 kHz: probably, a parasitic pole acts beyond the investigated frequency range, limiting its employment. To give further evidence of the FO-controller benefits, in the figure the integer-order compensator $C_I(s)$ counterpart has been also presented. It has been obtained with the identical gain and time constants but fixing $\alpha = 1$. Both the magnitude and the phase responses are completely different from

the fractional-order one.

In the following, all the simulation results of the controller will be done by considering $C_a(s)$, in order to match with the real compensator described in Fig. 3.43A.

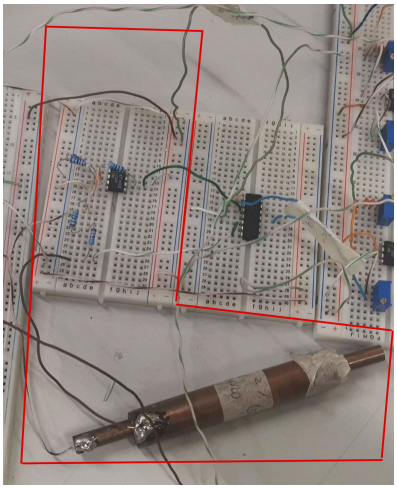

(A) Controller implementation

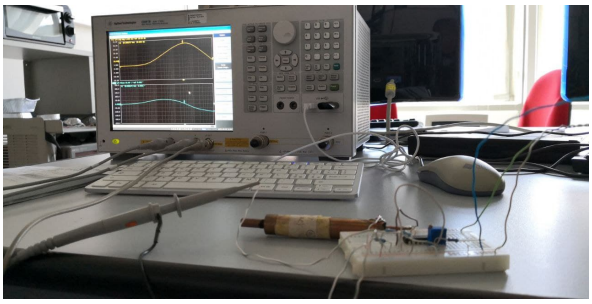

(B) Frequency response measurement

FIGURE 3.43: Implementation and frequency measurement setup for the FOLC

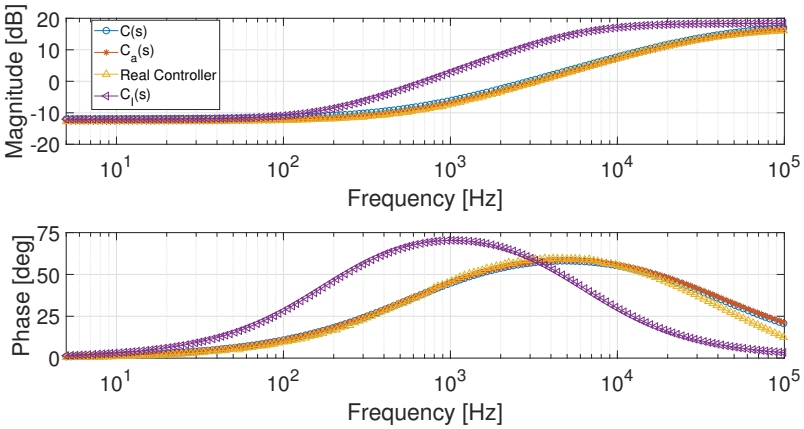

FIGURE 3.44: Bode diagrams of the nominal, tuned, real and integer-order controllers

Plant: The plant of (3.21) has been implemented by using two inverting Miller's integrators according to the schematics of Fig. 3.45, exploiting two LT1007 opamps.

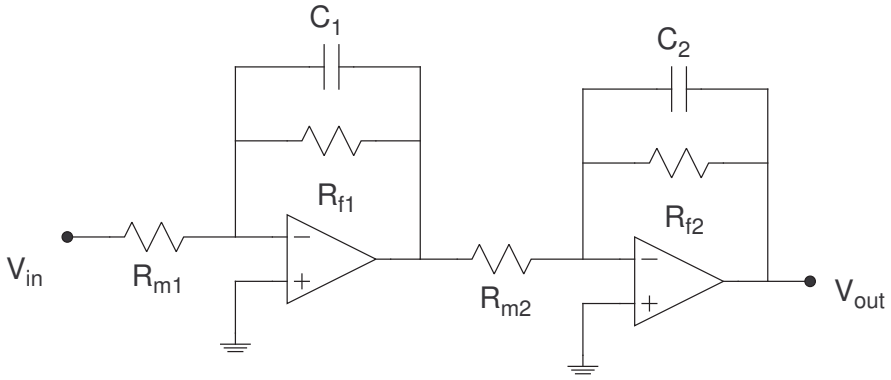

FIGURE 3.45: Electronics schematics of $P(s)$

The gain and the two time constants of $P(s)$ can be computed by the following relationships, while in Tab. 3.10 the obtained capacitance and resistance values are reported.

$$\begin{aligned} \tau_1 &= R_{f1}C_1 \\ \tau_2 &= R_{f2}C_2 \\ k &= \left(-\frac{R_{f1}}{R_{m1}}\right) \cdot \left(-\frac{R_{f2}}{R_{m2}}\right) \end{aligned}$$

Parameter	**Value**
R_{f1} [kΩ]	100
R_{m1} [kΩ]	1
R_{f2} [kΩ]	33
R_{m2} [kΩ]	3.3
C_1 [nF]	24
C_2 [nF]	25

TABLE 3.10: Resistance and capacitance values for the analog implementation of $P(s)$

Also in this case, the comparison between the nominal plant and the tuned one are compared in Fig. 3.46. Unfortunately, the real frequency response has not been taken due to the high gain of the process that cannot be investigated by the network analyzer.

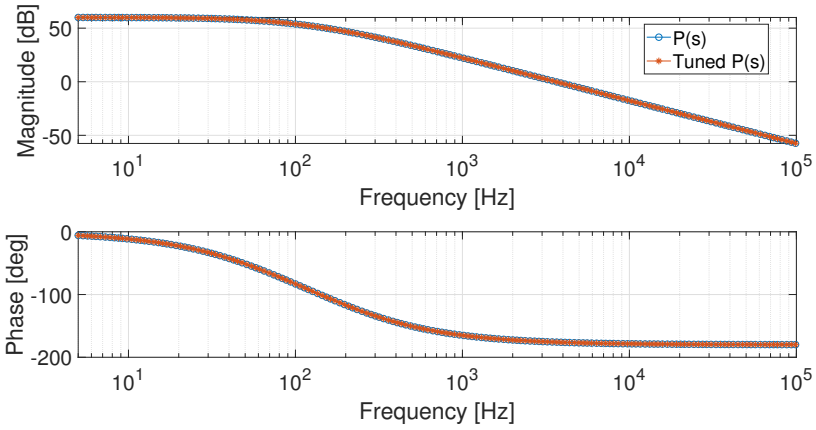

FIGURE 3.46: Bode diagrams of the nominal and tuned plants

Open-loop system: Once both the controller and the plant have been implemented, a first analysis on the open-loop system has been performed. In particular, taking into account the real controller frequency response, the Bode diagram of the open-loop TF (i.e., simulated plant and real controller) has been evaluated in order to understand if the real implementation fits the nominal behaviour of the system. In addition, also the IO-open-loop system is depicted with the aim of highlighting the difference with the proposed compensator.

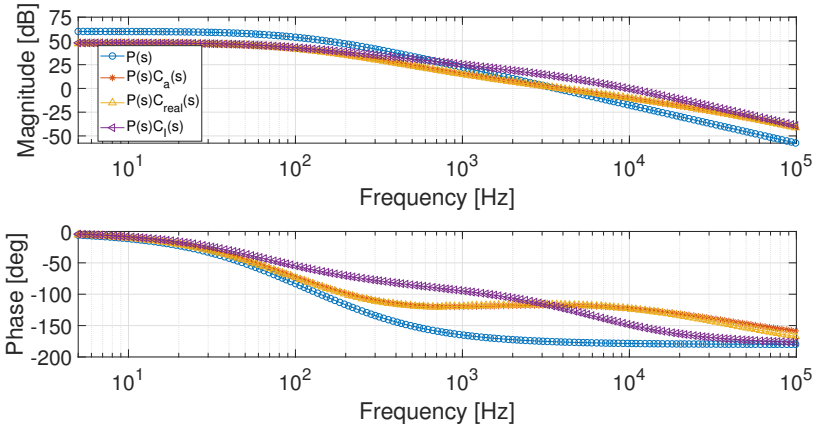

FIGURE 3.47: Bode diagrams of simulated, real and integer-order open-loop system

The IO-open-loop system does not have any constant-phase zone and, therefore, the required constraints are not satisfied. On the other hand, the real open-loop system implemented with the C130B fits almost well the nominal open-loop system response, both in the magnitude and in the phase.

Closed-loop system: Finally, the unitary feedback action has been realized by implementing a differential amplifier with R = 1 kΩ and a LT1007 as opamp. The overall system is schematized in Fig. 3.48, where the first opamp implements the feedback action, the second one takes into account the FOLC and the last two opamps are related to the plant implementation.

In particular, $\mathbf{y}$ represents the system output, $\mathbf{V_{in}}$ the signal reference and $\mathbf{V_e}$ the closed-loop error.

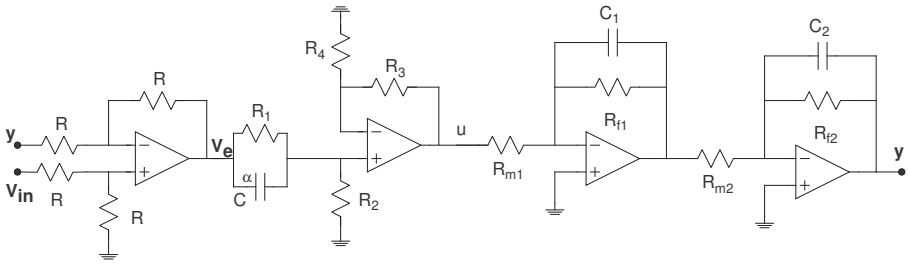

FIGURE 3.48: Electronics schematics of the full analog closed-loop system

However, in the real circuit implementation, two non-inverting voltage buffers have been mounted before and after the FOLC to avoid any further influence or impedance coupling.

The overall circuit is shown in Fig. 3.49, where in the first breadboard the feedback action is implemented (top) and the input buffer for the controller (bottom), the second and third ones are related to the FOLC realization and the regulator output buffer, respectively, while, in the fourth, the plant has been mounted with the two Miller's integrators.

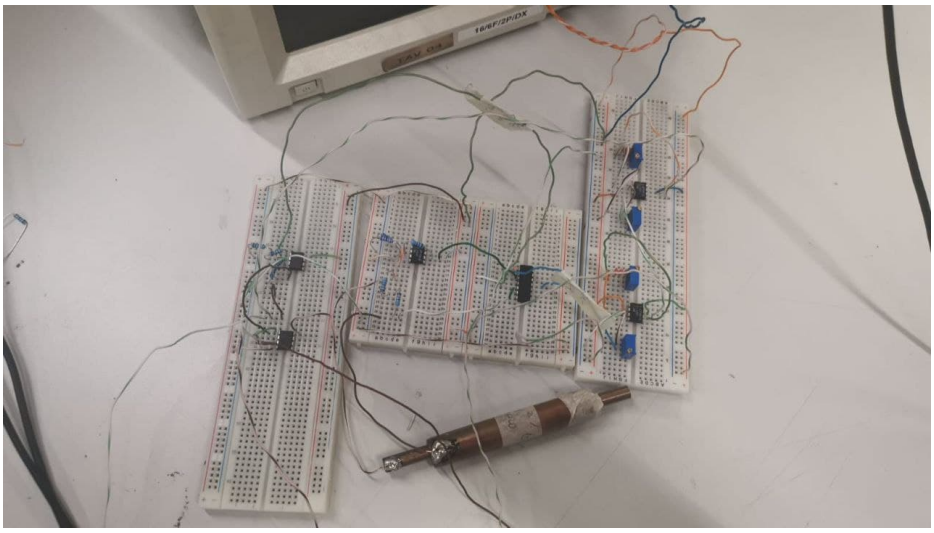

FIGURE 3.49: Real implementation of the overall closed-loop system

Results

Taking into account all the considerations made above, the simulations of the whole system have been performed by changing, once at time, the resistance values related to the gain k and the time constants τ_1 and τ_2. In details, the comparison with the simulated system will be always reported to highlight any difference with the real circuit.

The nominal system response has been performed by providing a square wave as input and it has been measured with a standard oscilloscope, whose screenshot is reported in Fig. 3.50.

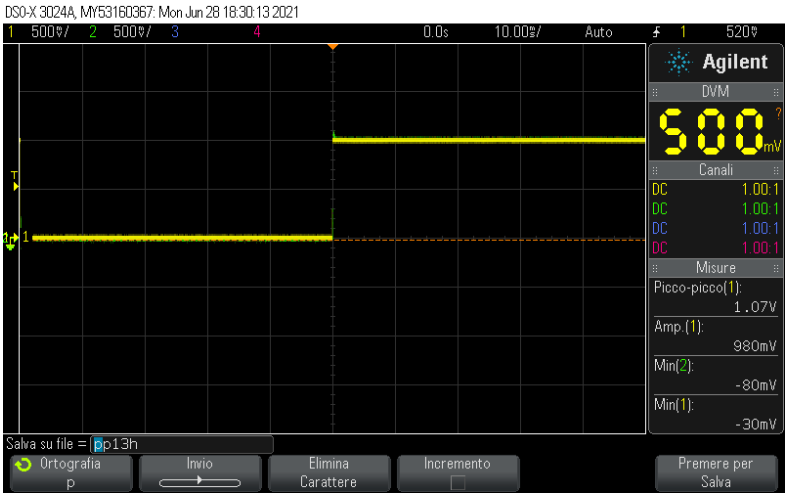

FIGURE 3.50: Screenshot of the nominal closed-loop system response

The comparison of the acquired response with the simulated closed-loop system is depicted in Fig. 3.51. It can be noticed that some mismatches arise with the simulated response: the real system is more damped than the simulated one (about 8% smaller). This phenomenon probably is due to leakage of energy caused by the breadboards and wires of the all four breadboards used during the experiment. Moreover, the two responses show a different rising time. These values have been measured and their difference is about 46.4 µs: such a small discrepancy can be accepted considering that the entire circuit is mounted in the breadboards.

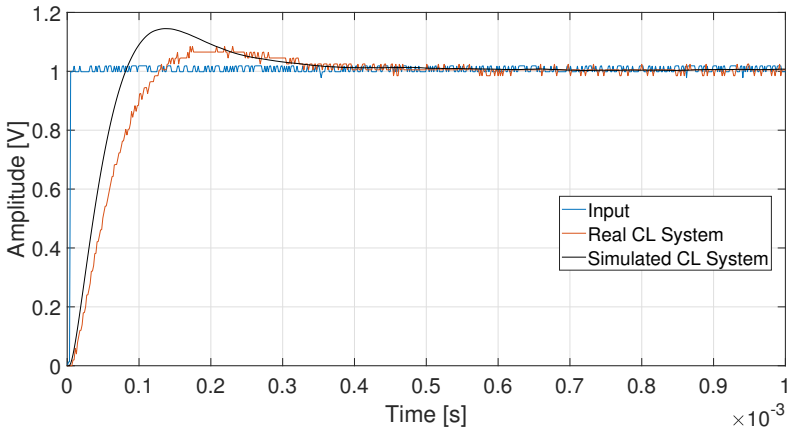

FIGURE 3.51: Input, acquired and simulated closed-loop system responses in the nominal conditions

In the last three paragraphs, the three parameters variations will be investigated, providing the lists of resistance values used and the related plots for the comparison with the simulated system.

Gain variation: The real circuit gain k has been changed from 800 to 1200 with a step of 100, according to the different R_{m2} values of the analog circuit of Fig. 3.48. In particular, the different values are listed in Tab. 3.11.

Gain	$\mathbf{R_{m2}}$ [kΩ]
800	4.09
900	3.61
1000	3.3
1100	3
1200	2.73

TABLE 3.11: Values of R_{m2} for the tested plant gains

The resistance values have been obtained with a trimmer, which has been measured with a bench multimeter. The measurements have been performed in the same working conditions, and they are depicted in Fig. 3.52, where on the left the simulated responses are shown, while on the right the acquired ones. More specifically, a zoom of the transient response have been taken in Fig. 3.52B. From these two figures, it can be observed that the real system follows the same behaviour of the simulated one, as the gain varies. In particular, the time difference between the first response (i.e., $k = 800$) and the last one (i.e., $k = 1200$) of both real and simulated systems are comparable, about 28.8 µs and 25.6 µs, respectively.

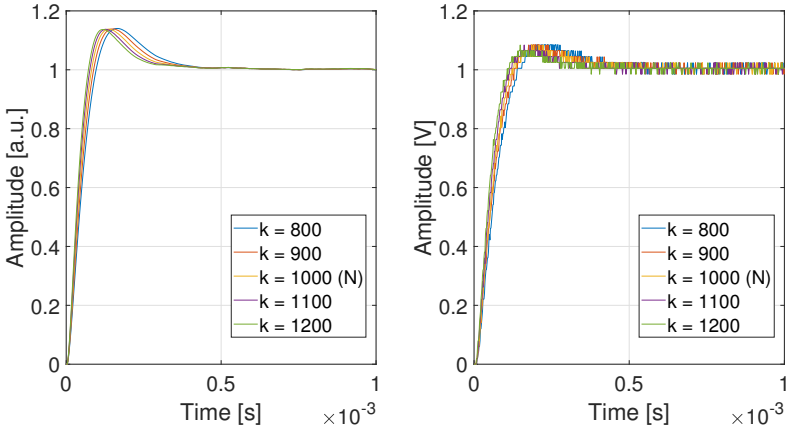

(A) Comparison between simulated (left) and acquired (right) FO-closed-loop systems

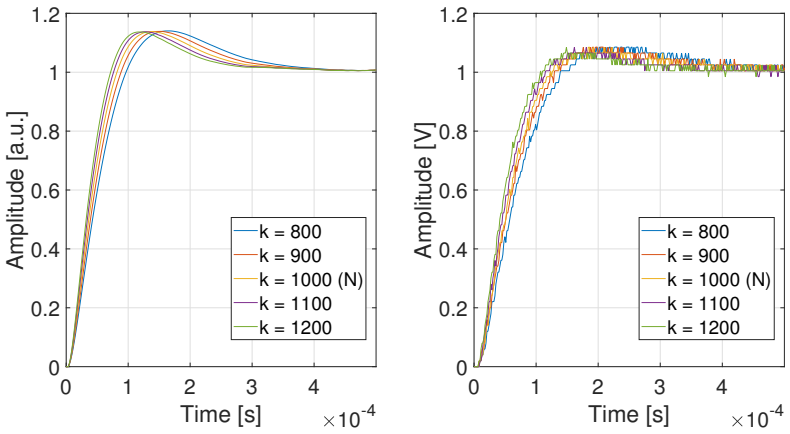

(B) Zoom in the transient region

FIGURE 3.52: Comparison between simulated and acquired FO-closed-loop systems for different plant gain

τ_1 variation: After the gain, also τ_1 has been varied in order to understand if the real circuit follows the nominal behaviour. More specifically, the time constant has been varied from $2.2 \times 10^{-3}\,\mathrm{s}^{1/\alpha}$ to $2.6 \times 10^{-3}\,\mathrm{s}^{1/\alpha}$ with a step size of 0.1×10^{-3}. In this case, according to the plant implementation of Fig. 3.45, both R_{m1} and R_{f1} have been changed, and their values are defined in Tab. 3.12. Also in this case, the two resistance values are obtained with a trimmer and, then, measurements have been performed. Results are reported in Fig. 3.53, where on the left the simulated responses are evaluated and on the right the acquired ones.

τ_1	$\mathbf{R_{m1}}$ [kΩ]	$\mathbf{R_{f1}}$ [kΩ]
$2.2 \times 10^{-3}\,\mathrm{s}^{1/\alpha}$	0.915	91.680
$2.3 \times 10^{-3}\,\mathrm{s}^{1/\alpha}$	0.963	95.815
$2.4 \times 10^{-3}\,\mathrm{s}^{1/\alpha}$	1	100
$2.5 \times 10^{-3}\,\mathrm{s}^{1/\alpha}$	1.02	104.12
$2.6 \times 10^{-3}\,\mathrm{s}^{1/\alpha}$	1.073	108.38

TABLE 3.12: Values of R_{m1} and R_{f1} for the tested time constant τ_1

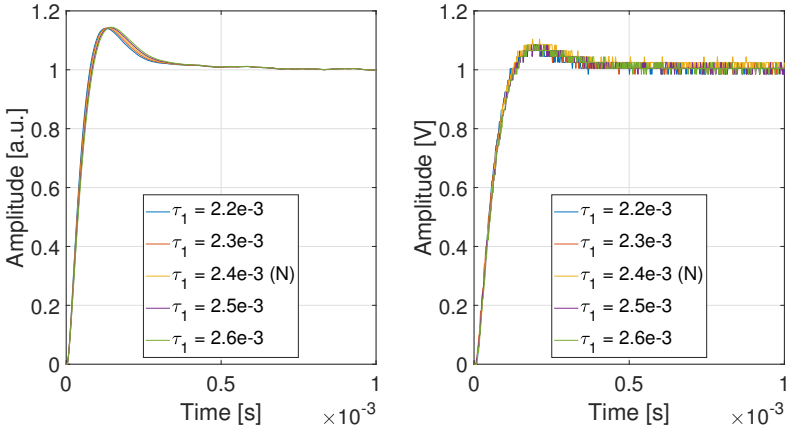

(A) Comparison between simulated (left) and acquired (right) FO-closed-loop systems for different τ_1

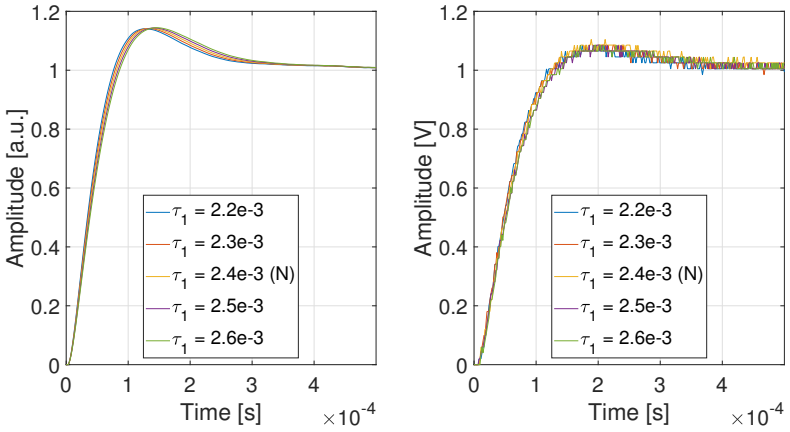

(B) Zoom in the transient region

FIGURE 3.53: Comparison between simulated and acquired FO-closed-loop systems for different τ_1

Despite of the aforementioned mismatches in the overshoot and rising time that have been justified, the acquired responses maintain the same overshoot and also the dynamics are comparable with the simulated ones, as the zoom of Fig. 3.53B highlights.

τ_2 variation: In the last analysis, τ_2 has been varied from $0.6 \times 10^{-3}\,\mathrm{s}^{1/\alpha}$ to $1 \times 10^{-3}\,\mathrm{s}^{1/\alpha}$ with a step size of $0.1 \times 10^{-3}\,\mathrm{s}^{1/\alpha}$. Also in this case, taking into account the Miller's integrators implementation, both $\mathrm{R_{m2}}$ and $\mathrm{R_{f2}}$ values are computed to match with the interested time constants and they are reported in Tab. 3.13.

τ_1	$\mathbf{R_{m2}}$ [kΩ]	$\mathbf{R_{f2}}$ [kΩ]
$0.6 \times 10^{-3}\,\mathrm{s}^{1/\alpha}$	2.467	23.980
$0.7 \times 10^{-3}\,\mathrm{s}^{1/\alpha}$	2.813	27.990
$0.8 \times 10^{-3}\,\mathrm{s}^{1/\alpha}$	3.3	33
$0.9 \times 10^{-3}\,\mathrm{s}^{1/\alpha}$	3.690	36.030
$1 \times 10^{-3}\,\mathrm{s}^{1/\alpha}$	4.054	39.975

TABLE 3.13: Values of $\mathrm{R_{m2}}$ and $\mathrm{R_{f2}}$ for the tested time constant τ_2

The comparison between the acquired measurements and the simulated step responses is depicted in Fig. 3.54. As reported in the paragraph 3.3.2, the overshoot increases when the time-constant τ_2 increases as well. More in details, the percentage of overshoot increasing is comparable (almost 3% in both cases). Besides, the rising time increases with τ_2.

In conclusion, all these results allow to validate the usage of the C130B as CPE for control applications: indeed, its robustness has been proved by varying all the parameters of the plant to be controlled and the device stability has been also demonstrated considering the several tests that have been performed with this experimental setup. Furthermore, the comparison with the IO-lead compensator counterpart has allowed to give evidence of the efficiency of the Fractional Calculus in the automatic control field.

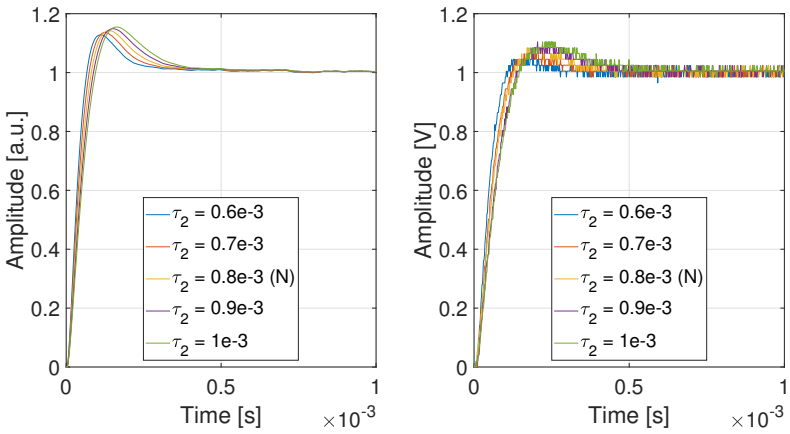

(A) Comparison between simulated (left) and acquired (right) FO-closed-loop systems for different τ_2

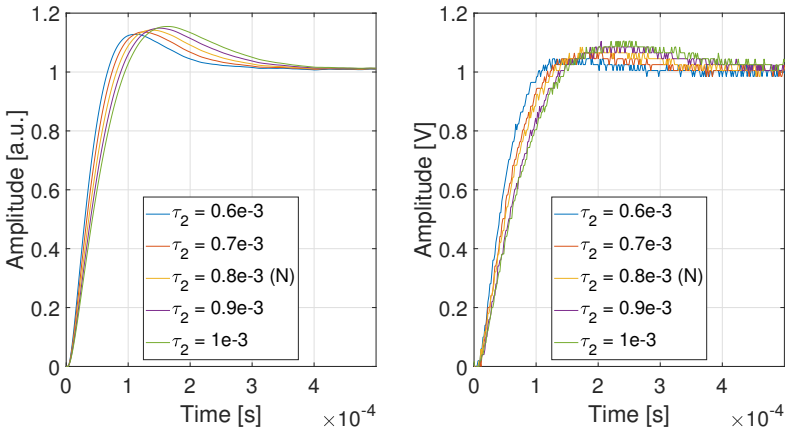

(B) Zoom in the transient region

FIGURE 3.54: Comparison between simulated and acquired FO-closed-loop systems for different τ_2

Chapter 4

Bacterial Cellulose-based FOEs

As stated in the Introduction, one of the most important problem in the modern technology is strictly related to the amount of non renewable materials, energy and the quantity of produced electronics. Due to the low-cost of commercial electronics, their utilization life is reduced compared to the products of fifty years ago. The huge quantity of unused electronics, also defined as electronics wastes (e-wastes), determines significant issues in their correct disposal.
Actually, it has been estimated that 44.7×10^9 kg of e-wastes have been produced in the 2016, an equivalent of about 4500 Eiffel towers [95], and the amount of e-wastes increase every year: WEEE forum estimates that every person will produced in the 2021 an average of e-wasteS of about 7.6 kg - so, overall, 57.4×10^9 kg [96]. Indeed, the COVID-19 outbrake has highlighted the increasing demand of electronics, from wireless headphones to computers for smart working or e-learning. The main drawback of such a demand is that only a small percentage of discarded devices are correctly disposed [97]. Obviously, this might lead to the release of dangerous chemical matter in the environment that can affect our health. For this reason, the most important companies are working on new technologies to recover components and materials to reduce the amount of e-wastes [98], [99].
Considering all these aspects, a new greener and ecological technology should be realized. In particular, in the electronics field, a new class of electronics has to be proposed with the aim of maintaining (or improving) the already existing performances and, above all, respecting and protecting the environment. The aforementioned objectives can be fulfilled by exploiting new materials, produced in an eco-friendly way with small energy quantities and ease of disposing.

In such a context, the proposed work introduces a new possible technology for realizing a new class of green capacitors by exploiting the cellulose, which

is the most common biopolymer on Earth. In details, the cellulose produced by bacteria will be employed due to its eco-friendly production and ease of disposing. As demonstrated in the previous chapters, the possibility of having more degree of freedoms allows to achieve more robust performances. Therefore, the realized capacitor is always described inside the Fractional Calculus framework: in this way, the possibility of realizing a green device with enhanced performances is investigated.

The chapter will be divided as follows: in the first section, a brief overview of the Bacterial Cellulose will be provided; then, the FOE realization and characterization will be described. Finally, some further investigations on the Bacterial Cellulose-based FOE are conducted.

4.1 Overview

Bacterial cellulose (BC) is an organic compound with the formula $(C_6H_{10}O_5)_n$ generated by some bacteria species, like *Acetobacter*, *Agrobacterium* or *Sarcina*. Although BC has the same chemical formula of the pulp-based counterpart, the former shows very different macromolecular structure and unique proprieties, as demonstrated in the next section.

The BC production has been studied from different scientists evaluating the type of bacteria or the necessary biochemical reactions [100], [101]. Furthermore, it has also been proven that BC can be produced in typical laboratory conditions [102], without excessive use of water, energy, or other non-eco-friendly procedures, which are required by the pulp industry. BC can be obtained by commercial tea bags, sucrose, bacteria and yeast strain. A catalyst like acetic acid can be employed to increase the yield, control the pH or the temperature, while sodium hydroxide is used for the final product purification. The final BC pellicle is shown in Fig. 4.1.

FIGURE 4.1: BC pellicle.
Credits: Wikipedia.

4.1.1 Proprieties and applications

As said before, the BC and pulp-based cellulose are represented by the same chemical formula showing, however, different properties. Due to BC fundamental components, it is classified as polysaccharide and shows polymeric characteristics.
The main BC proprieties are [103], [104]: more chemically pure, high water

capability holding, greater polymerization and, so, a greater tensile strength, more crystalline structure and it shows an ultrafine network architecture. These two last proprieties allow BC to have a greater moldability and the BC chains can aggregate to form ribbon-like micro-fibrils with a width of some nm, which are smaller than the plant cellulose ones and make the BC more porous. These fibrils are insoluble and inelastic and create a dense reticulated structure which is stabilized by the presence of hydrogen, having a tensile strength comparable to the steel [105].
The Young's modulus, which expresses the relationship among stress and strain in linear elasticity regime, is in the order of GPa in any polymeric sheet and is maximum across the plane of the sheet. This behaviour is in accordance to what said before and allows to define the BC structure as a *"super-molecular"* one.

Related to BC applications, the compound is employed in several different fields such as medical application, electro-active polymers, magnetic sensors and electronics industry. In the next subsections, a brief description of the aforementioned applications is provided.

Electro-active polymers

This application here reported is based on the study of Kim et al. [105]. Electro-Active Polymers (EAPs) are particular structures that exhibit a deformation if they are subjected to an electric field. They find a lot of applications in bio-inspired sensors, biomedical devices, artificial muscles, photovoltaic cells, chemical sensors, organic light-emitting diodes and touch panels. A great challenge is to exploit BC for its peculiar proprieties (like its high tensile strength or dense reticulated structure) with the aim of producing an eco-friendly electro-active actuator.
However, two main problems arise due to the BC utilization:

- interface between BC and metallic electrode;
- performance enhancement in dry air.

The first problem arises when a long utilization of BC is made: indeed, electrodes come loose from the BC. This problem can be solved using more flexible and conducting polymers: in this way BC can still be used as EAP. As solution, this study proposes a particular approach where a tri-layered structure is developed: in the middle there is the BC properly treated (as it will be explained below), while layers (i.e., electrodes) made up with poly(3,4-ethylenedioxythiophene)poly(styrenesulfonate) PEDOT:PSS are used as external face sheets.

The second issue is strictly related to the deteriorating system performances because, in hydrate conditions, BC swells up. To overcome such a drawback, Kim et al. proposed to employ Ionic Liquids (ILs). ILs are organic solvents and they can be chosen according to the BC application. They exhibit a lot of advantages like high ionic conductivity, high thermal stability, non-volatile and non-flammable properties. They can also be used as electrolytes for electrochemical capacitors and EAP actuators. Example of

the most common ILs used are 1-ethyl-3-methylimidazolium tetrafluoroborate (EMIM-BF_4) and 1-butyl-3-methylimidazolium chloride (BMIM-Cl).

To make sure that BC absorbs a great quantity of ILs, it has been properly prepared. A simple *freeze-dry* method at $-50\,°C$ for 24 h is applied, showing good results: the treated BC has a more porous structure and able to hold more ILs.

Finally, the overall sandwich structure reported in Fig. 4.2 can be tested as EAP.

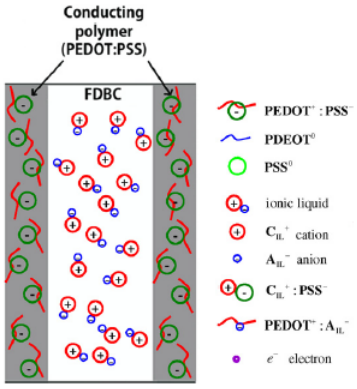

FIGURE 4.2: BC EPA structure.
Credits: Kim et al. (2013)[105].

If an external voltage is applied, two main electrochemical reactions will occur: at the anode there will be an electrochemical reduction, while at the cathode an oxidation, thanks to the PEDOT:PSS layers that absorb ions (cations or anions) and re-eject counter-ions from the other layer. Cations and anions generate an ions migration in different size (anions molecular size is smaller than the cations one) and, hence, the applied external voltage determines a large bending deformation, as Fig. 4.3 highlights.

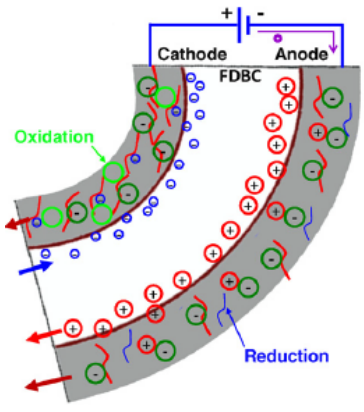

FIGURE 4.3: BC EPA deformation.
Credits: Kim et al. (2013) [105].

As the figure shows, BC acts as electro-active actuator and the ILs presence allows to have a more porous structure and better electrochemical reactions in the external layers (i.e., electrodes).

Experiments reported in [105] use both EMIM-BF_4 and BMIM-Cl, guaranteeing different performances.

Magnetic sensors

This application here reported is based on the study of Zheng et al. [106]. BC is used to create a flexible magnetic membrane and synthesize in situ FeO_4 particles. Due to their nature, magnetic nanoparticles tend to aggregate and change the mechanical proprieties of the matrix in which they are diffused. This study, using the particular dense reticular structure of the BC, tries to diffuse homogeneously nanoparticles using an ultrasonic irradiation. Considering the appropriately treated BC reticular structure and iron ions diffused inside, the aforementioned nanoparticles are able to anchored on some BC fibers (in which there are polar hydroxyl groups) and synthesize FeO_4 particles according to this simple chemical reaction:

$$Fe^{2+} + 2Fe^{3+} + 8OH^{-} \rightarrow Fe_3O_4 + 4H_2O. \tag{4.1}$$

From (4.1), it can be detected that also water molecules are produced and kept by the BC due to its water absorption propriety. The general process and the obtained reticular structure are reported in Fig. 4.4.

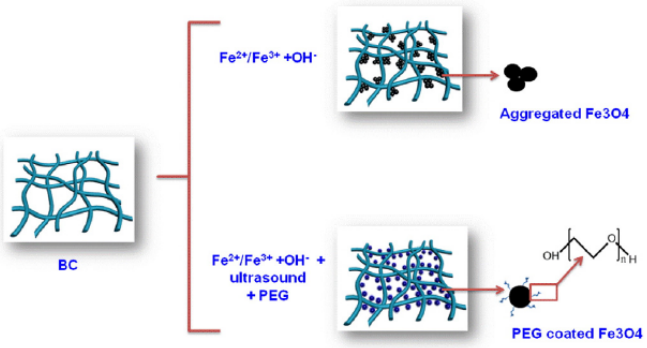

FIGURE 4.4: BC-based magnetic membrane formation process. Credits: Zheng et al. (2013) [106].

The BC membrane is prepared according to these following steps:

- BC membrane is boiled in NaOH solution and then washed into distilled water (nytrogen was bubbled to prevent oxidation) until it becomes neutral;
- Solutions with Fe are prepared and dissolved in the above-mentioned distilled water;
- BC membrane is then immersed for 12 hours in the prepared solutions;
- At the end, BC membrane is then immersed into the distilled water differently treated: simple aqueous solution of NaOH (indicated as "b."), aqueous solution of NaOH with ultrasound irradiation (indicated as "c."), and again this last one with ethylene glycol (indicated as "d.") This particular solution is represented in the last part of Fig. 4.4.

The untreated BC and the different membranes are shown in the next figure using the Field Emission Scanning Electron Microscope according to the above discussed legend (the untreated BC membrane is indicated as "a.").

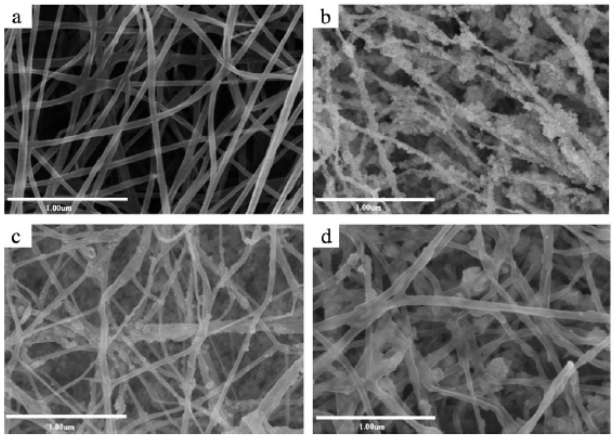

FIGURE 4.5: BC structure with FeO_4 particles.
Credits: Zheng et al. (2013) [106].

Looking at the figure, different reticular structures are defined. In any case, these membranes show a small hysteresis loop with low remaining magnetization, allowing to define them as "super-paramagnetic material". In particular, the ultrasonic irradiation provides a lower saturation magnetization (the ethylene glycol surround each magnetic particles) and gives the possibility to magnetically actuate the treated membranes, as Fig. 4.6 reveals.

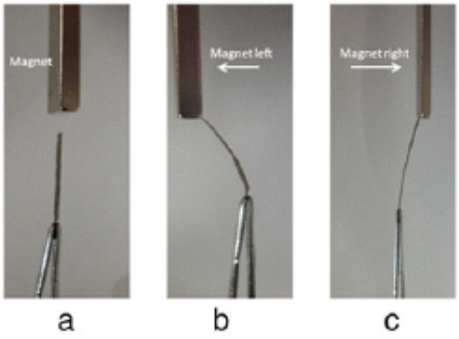

FIGURE 4.6: BC membrane actuated by a magnet.
Credits: Zheng et al. (2013) [106].

Fig. 4.6 highlights the flexible nature of the membrane and, in particular, neither thermal nor mechanical proprieties have got worse: the presence of FeO_4 improves both thermal stability (it is also higher in those membranes treated with ultrasound irradiation) and Young's module due to a more dense structure and in particular the maximum value is obtained for the membrane treated with ethylene glycol.

4.2 Bacterial Cellulose-based capacitor

The presented applications have highlighted the possibility of using BC as a green material in the electronics field. The feasibility of obtaining a new type of capacitor, where BC is employed as dielectrics in a parallel plate configuration, has been realized in the 2019 [107] and will be presented in this section. In details, the features of the materials will be described and the evidence of the fractional-order nature will be demonstrated.

4.2.1 Materials

The BC employed for the device realization, has been purchased from Bio-Faber s.r.l.s. and used without any further manipulation. It has been obtained by a culture of Acetobacter xylinum, see [102] for further details on the production procedure, as dehydrated sheets of about $(230 \times 280 \times 0.04)$ mm^3. A square of roughly 5 mm has been cut and it has been used as dielectrics. Finally, the parallel plates have been realized by exploiting conventional single side Fr4 Copper laminated card. The overall device, during its assembling phases, is depicted in Fig. 4.7. The final size of the assembled device is 11 mm $\times$ 31 mm $\times$ 4 mm.

(A) BC dielectrics

(B) BC dielectrics and Fr4 copper electrodes

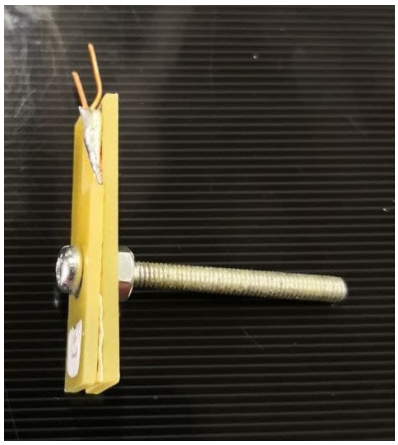

(C) Assembled device

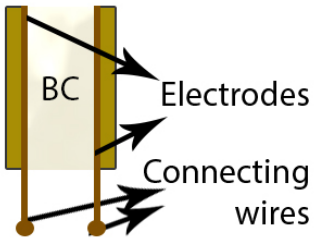

(D) General schematics

FIGURE 4.7: BC-based device

4.2.2 FOE characterization

The electrical characterization has been performed by means of the Keysight Network Analyzer E5061B, whose general schematics is drawn in Fig. 4.8.

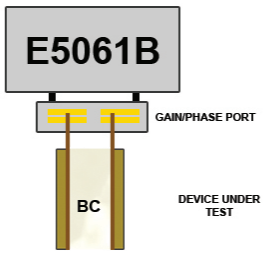

FIGURE 4.8: Schematics of the measurement with E5061B

The instrument setup used during the measurement is the following:

- Logarithmic sweep in the range 100 Hz to 30×10^6 Hz;
- Intermediate Frequency BandWidth (IFBW): 100 Hz;
- 201 points logarithmically distributed in the investigated domain;
- Averaging factor: 64.

More specifically, three different samples, labeled as *#1*, *#2* and *#3* have been realized. As example, the screenshot of a performed measurement is reported in the next figure.

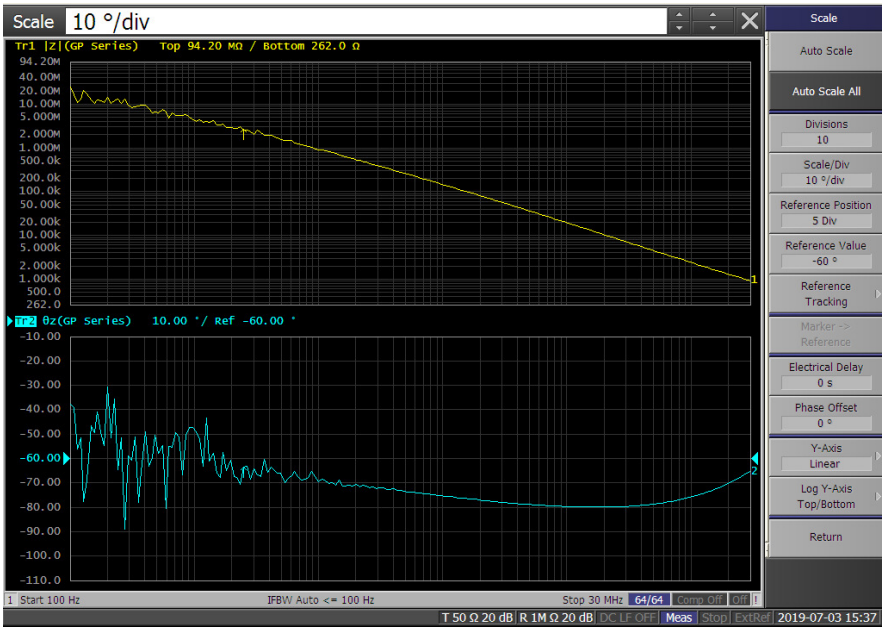

FIGURE 4.9: Frequency measurement of the BC-based FOE.
Credits: [107]

The frequency response of the BC-based FOE exhibits a constant phase-lag of about −80 deg in the high frequency range, more specifically from

1 kHz to 1000 kHz. For such a reason, the proposed EECM of Fig. 4.10 takes into account a FO-capacitor. Furthermore, the resistor R_1 models the electrodes/contact resistance and it has been directly measured and set approximately to 0.5 Ω, while the parallel FO-R_2C describes the BC electrical behaviour. The overall impedance of the proposed model is reported in (4.2)

$$Z(s)_{BC} = R_1 + \frac{1}{1 + R_2 C s^{\alpha}} \tag{4.2}$$

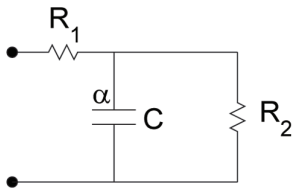

FIGURE 4.10: BC-based FOE EECM.
Credits: [107]

The realized devices have been tested in typical lab conditions and, for each of them, ten different measurements have been performed and identified. More specifically, the system parameters of (4.2) have been identified by applying the GAs with the following parameters:

- Number of individuals: 300;
- Maximum number of iteration: 1000;
- Generation gap: 0.90;
- Precision: 10;
- Number of variable: 3.

Related to the objective function, the same cost function $\mathcal{J}$ defined in (3.4) has been exploited to find out the best parameter values. As example, a comparison of the Bode diagrams between a performed measurement and its equivalent simulated impedance for the sample *#3* is shown in Fig. 4.11. More specifically, the error diagram (in absolute value) between measurement and correspondence model is depicted in Fig. 4.12. It can be noticed a maximum magnitude error of 1 dB and a phase error of less than 20 deg. Such a discrepancy is caused by measurement noise due to the employed network.

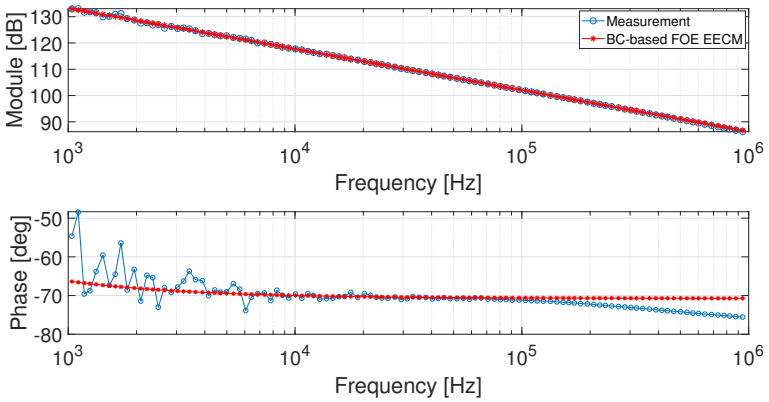

FIGURE 4.11: Bode diagram comparison for *#3* sample

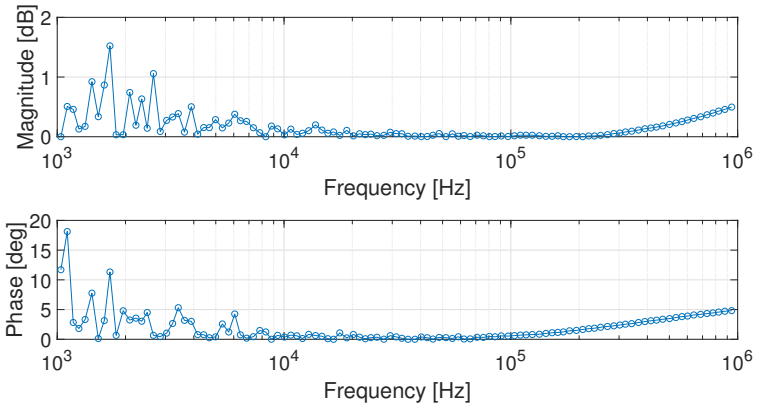

FIGURE 4.12: Bode diagram for *#3* sample model error

It can be detected that the BC-based device can be modeled as a FOE in the investigated frequency domain with a phase-angle ripple of about $\pm 5\,\text{deg}$ in $1 \times 10^4\,\text{kHz}$ to $1 \times 10^6\,\text{kHz}$. The overall parameters for each sample and its corresponding measurements are reported in Fig. 4.13, while in Tab. 4.1 the averaged parameters and their standard deviations are listed. From these results, the BC-based device can be defined as a FOE with a fractional-order of about 0.8.

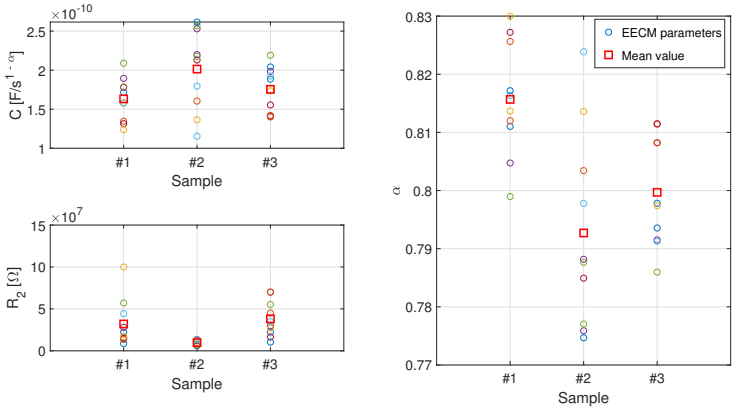

FIGURE 4.13: EECM parameters for each performed measurement

Sample	$\mathbf{R_2}$ [MΩ]	$\sigma_{\mathbf{R_2}}$ [MΩ]	**C** [nF/s$^{1-\alpha}$]	$\sigma_{\mathbf{C}}$ [nF/s$^{1-\alpha}$]	α	σ_α
#1	3.205×10^1	2.832×10^1	0.1632	2.737×10^{-2}	0.816	0.009
#2	9.790	2.953	0.2014	5.148×10^{-2}	0.793	0.017
#3	3.813×10^1	2.124×10^1	0.1754	2.922×10^{-2}	0.799	0.009

TABLE 4.1: EECM averaged parameters and standard deviations

4.2.3 Model validation

In this subsection, the proposed model will be validate both providing some possible explanations of its internal physical phenomena and analysing the relationship between the pseudocapacitance and the integer-order counterpart.

Physical phenomena

The diffusion of charges carrier inside a dispersing medium has been reported in Sec. 2.2.3 as possible explanation of solid-state capacitor fractional-order behaviour. Gea et al. in the 2011 have investigated the structure of the BC, and they discovered a three dimensional network of ultra-fine ribbon-shape bundles of cellulose microfibrils [108]. To verify the BC employed nature, a SEM (Scanning Electrone Microscope) analysis has been realized and reported in Fig. 4.14. SEM micrograph has been obtained using a *Cambridge 90* instrument and the sample has been fractured in liquid nitrogen. The shattered surface has been sputter-coated with gold before the SEM micrographs have been taken. Looking at the figure, it can be stated that even the investigated BC in this study has a porous nature.
Furthermore, an XPS (X-ray Photoelectron Spectroscopy) analysis has been performed in order to investigate the presence of species that can justify the diffusion of mobile charges inside the network. The measurements have been carried out on a *VG Instrument* electron spectrometer using a $Mg\ K_{\alpha_{1,2}}$ X-ray source with an energy of 1253.6 eV. In details, the standard X-ray source working conditions are: 300 W, 15 kV and 20 mA. The base pressure of the instrument has been set tp 5×10^{-10} Torr, while an operating pressure of 2×10^{-8} Torr has been exploited. Pass energy values of 100 eV and 20 eV have been used for widescans and narrowscans, respectively. The semiquantitative surface analyses have been performed by the determination of the photoelectron peak areas, which are computed by multiplying the experimental values with the appropriate sensitivity factor. For acquiring the spectra, a take-off angle of 80 deg has been chosen. Finally, the binding energies have been referred to the C-H level at 285 eV.

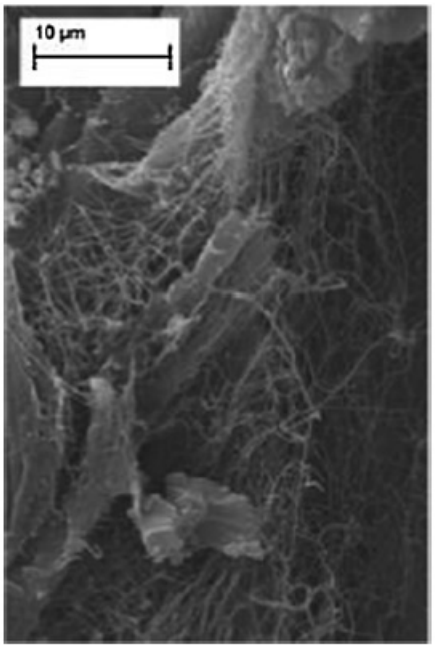

FIGURE 4.14: SEM micrograph of the BC section sample.
Credits: [107]

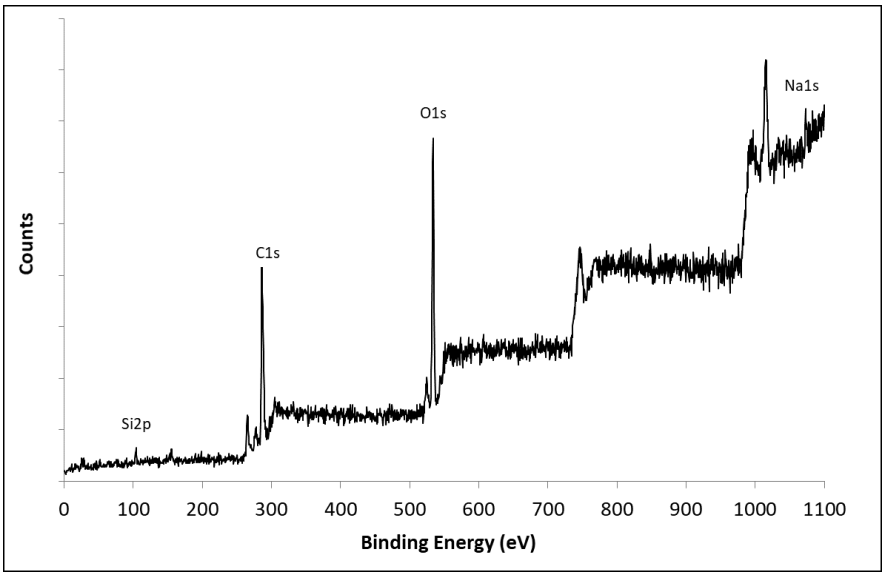

FIGURE 4.15: XPS widescan of BC sample.
Credits: [107]

From the XPS analysis of Fig. 4.15, the presence of different species can be observed. More specifically, the presence of Carbon has been observed with an atomic abundance of 64%, Oxygen 31%, Silicon contamination 3%, and Sodium 2%. The sodium presence can be due to a residual of NaOH deriving from the mercerization process, where the following reaction occurs:

$$(C_6H_{10}O_5)_n + NaOH \rightarrow (C_6H_9O_4ONa)_n + nH_2O \tag{4.3}$$

The sodium ions can interact with water, forming a solvation shell [109].

In particular, the amount of water detected after drying of the BC samples under investigation is about 4% by weight. Therefore, these solvated ions can diffuse into the BC pores, being their transport facilitated when humidity intake is higher. From this first analysis, the diffusion of positive charges, i.e., Na^+ according to the phenomena and hypotheses described before, is a reasonable explanation of the fractional-order nature of the realized device.

Another investigation has been performed with the aim of understanding how the water inside the BC-based FOE characterizes the "fractionality"of the device.
The comparison has been conducted by extracting the water contained inside one of the investigated BC sample and drying it overnight in a oven at 60 °C. Subsequently, impedance measurements with the same experimental setup defined before have been taken. Results of this investigation are given in Fig. 4.16. The values of C, R_2 and α, identified for the dried sample, are reported as straight lines. The (C, R_2, α) mean values and corresponding 2σ intervals are also drawn for the samples described in the previous section. Studying the box plot, the capacitance values obtained for the dry device are outside the corresponding 2σ intervals, while for the α-order there is an overlapping with device *#1*. In conclusion, the performed analysis provides an indirect evidence of how mobile charges and water play a role in the BC-based FOE behaviour.

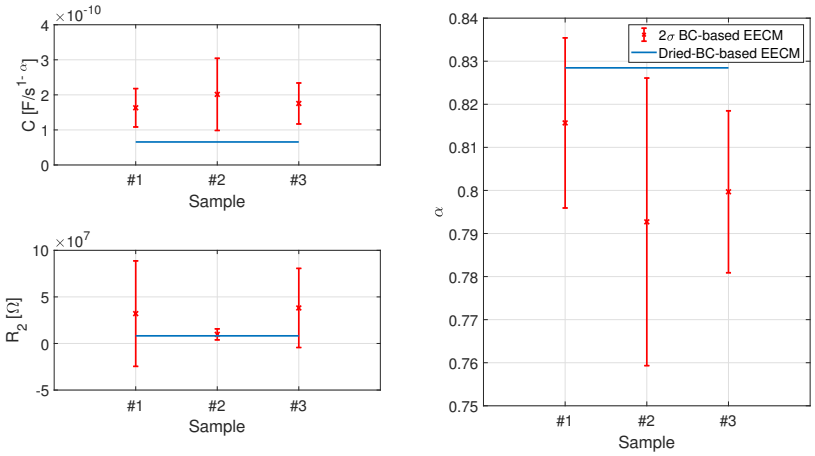

FIGURE 4.16: Box plot diagram for parameters of the three investigated devices. The corresponding values obtained for the dried device are reported as blue straight lines

Sensitivity to external agents

Brunetto et al. [110], [111] have studied the influence on environmental agents, such as humidity or temperature, in polymeric-based devices. Due to the presence of water in the BC, a further investigation on the humidity and temperature effects has been conducted in order to understand how they can change the device behaviour and, hence, its fractionality. The first analysis has been realized by sealing the device under investigation with a polyethylene sheet: with this new setup, the BC-based FOE is insulated from external humidity variations. Additionally, another sealed sample has been placed inside a polystyrene foam in order to avoid the device characteristics variation

due to external temperature changes. The temperature has been maintained constant when the device has not been used. The new setup is depicted in Fig. 4.17.

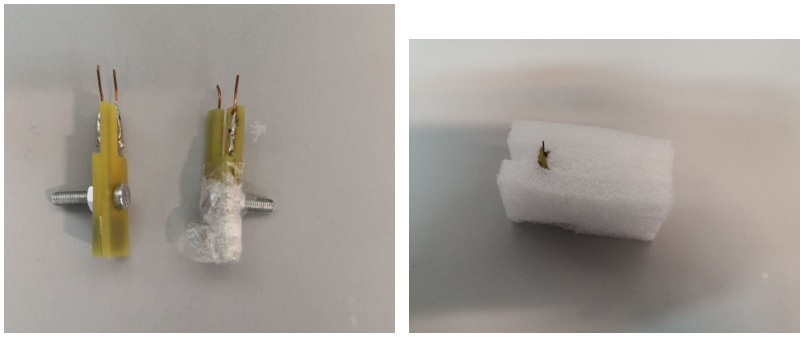

(A) Unsealed and sealed devices (B) Sealed device inside polystyrene foam

FIGURE 4.17: Sealed device to avoid humidity effects (left) and polystyrene box to avoid external temperature effects (right)

For these two experiments, more attention has been focused on the α order of the realized devices. The identified orders for the aforementioned analysis have been compared with a previous nominal sample and reported in Fig. 4.18, where: 'A' represents the sample analysed in the nominal working conditions, 'B' stands for the sample with the polyethylene sheet (i.e., subjected only to temperature variations), and 'C' is the sample insulated from both humidity and temperature changes. Neglecting the differences of the mean values due to three different investigated devices, it can be observed that the variability of α is reduced when the sample is not subjected to relative humidity and the variability decreases further when the sample is completely insulated from external environmental agents.

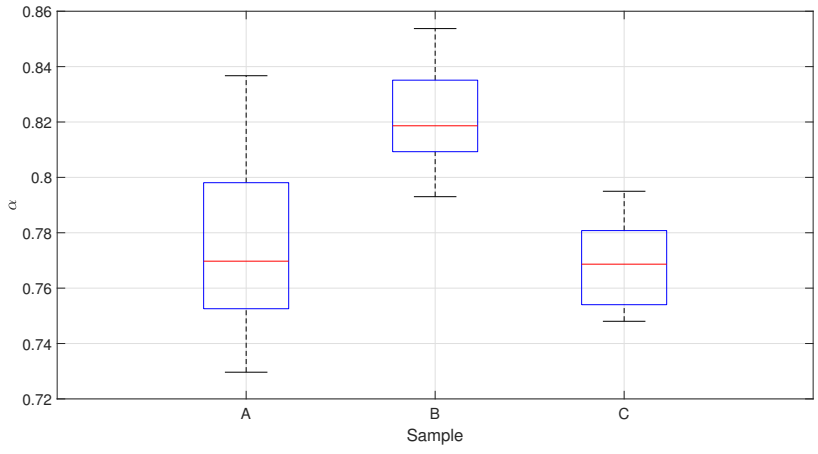

FIGURE 4.18: Humidity and temperature effects on the α order. A: typical lab working conditions; B: polyethylene sheet sealed sample; C. polyethylene sheet sealed sample inside polystyrene foam box

Effective and nominal capacitances comparison

A further evidence of the BC-based device fractional-order nature is provided by analyzing the relationship between the pseudocapacitance and the effective integer-order one, as already described in (2.2). The obtained values of C_i are then compared with the nominal capacitances C_n, whose values have been estimated by evaluating the materials properties of the dielectrics and devices geometry:

$$C_n = \varepsilon \cdot \frac{S}{d}, \tag{4.4}$$

where $\varepsilon = \varepsilon_0 \cdot \varepsilon_r$ is the dielectrics constant, S the electrodes surface, and d the dielectrics thickness. In details, ε_0 is the vacuum dielectrics constant and ε_r the relative one, which is computed by analyzing the type of material placed inside the parallel plates. Related to the BC relative dielectrics constant, it has been evaluated considering its main components: water in a percentage of 4% ($\varepsilon_{r,w} \approx 80$) and paper cellulose for the remaining part ($\varepsilon_{r,c} \approx 2$). Therefore: $\varepsilon_{r,BC} = 0.96 \cdot \varepsilon_{r,c} + 0.04 \cdot \varepsilon_{r,w} \simeq 5.12$.
Defining the parameters of the BC geometry, i.e., S = (6×5) $\text{mm}^2 = 3 \times 10^{-5}\,\text{m}^2$, the dielectrics thickness d = 170 µm and the BC dielectrics constant $\varepsilon_{r,BC}$, the nominal capacitances C_n are computed and the comparison with C and C_i is listed in Tab. 4.2. Looking at the values of C_i and C_n, it can be concluded that the two capacitances are comparable, providing evidence of the proposed EECM.

Sample	**C** [nF/s$^{1\text{ - }\alpha}$]	**C$_i$** [nF]	**C$_n$** [nF]
#1	1.632×10^{-1}	1.796×10^{-2}	7.966×10^{-3}
#2	2.014×10^{-1}	1.693×10^{-2}	7.966×10^{-3}
#3	1.754×10^{-1}	1.600×10^{-2}	7.966×10^{-3}

TABLE 4.2: Comparison between pseudo-, equivalent integer-order and nominal capacitances for the investigated samples

4.2.4 Application

The proposed BC-based FOE has been exploited for realizing a passive low-pass filter, whose schematics is reported below, with a resistance equal to R = 100 kΩ. This resistance value has been chosen in order to use the device under investigation in the region where it acts as FOE.

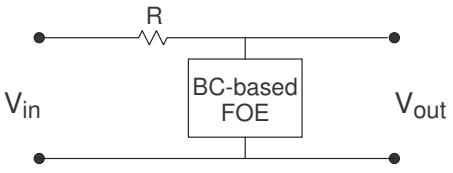

FIGURE 4.19: Passive BC-based RC schematics.
Credits: [107]

The FO-low-pass filter frequency response has been measured with the network analyzer E5061B. A screenshot of the performed experiment is depicted in Fig. 4.20. The evidence of the FO-nature has been highlighted by

comparing the obtained response with a standard low-pass filter. In details, the same resistor and a commercial integer-order capacitor of $C_i = 22\,pF$ have been employed as main components. The capacitance value has been defined in order to be as close as possible to effective capacitance of the investigated FOEs at the cut-off frequency value. The Bode diagrams of the realized filters are shown in Fig. 4.21, where it is quite evidence the difference both in the magnitude slope response and in the asymptotic phase-lag value, confirming the fractional-order nature of the proposed device.

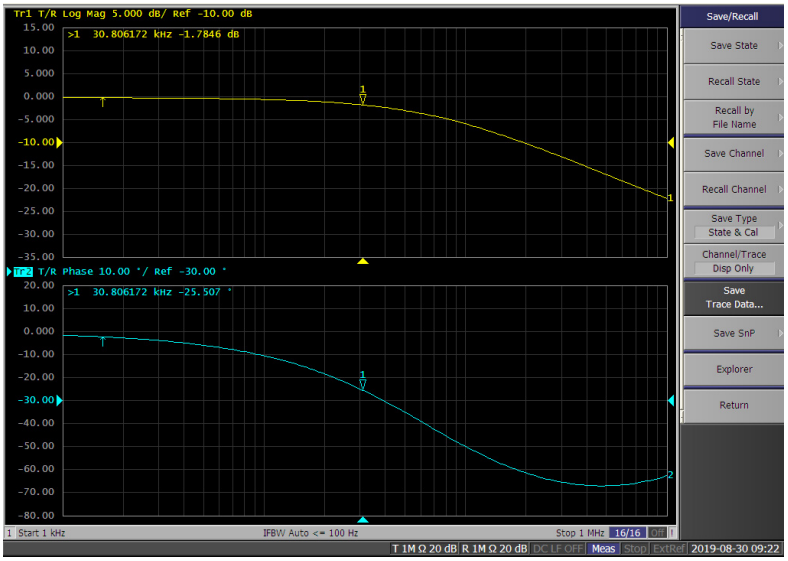

FIGURE 4.20: BC-based FOE low-pass filter frequency response. Credits: [107]

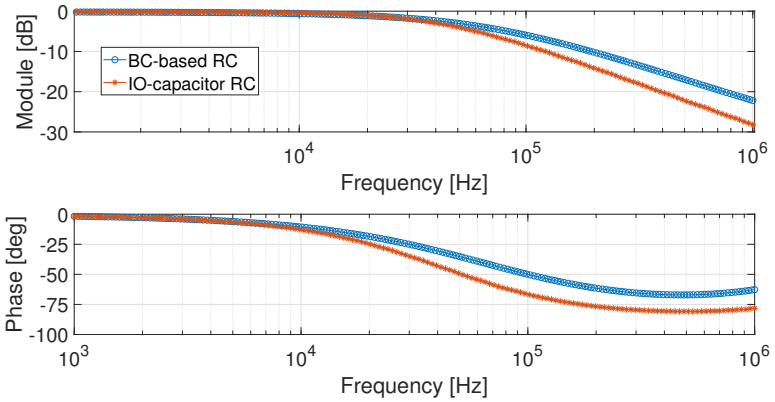

FIGURE 4.21: Frequency response comparison between the FO- and IO- RC filter implementations

4.3 Bacterial Cellulose with Ionic Liquids

A deeper analysis on the BC-based FOE has been conducted by exploiting the Ionic Liquids (ILs). As already shown, the presence of ILs inside the porous structure of the BC allows to enhance its performances thanks to the increased ionic conductivity. In this work, several ILs (made of different cations and/or anions) have been tested. However, only one of them has

provided encouraging results. Therefore, in this chapter only the promising ones will be provided, while in Appendix A the results for the other tested ILs are reported.

4.3.1 EMIM-TFMS

In the conducted studies during the 2020 and 2021, see [112]–[114] the 1-Ethyl-3-Methylimidazolium Trifluoromethanesulfonate (EMIM-TFMS) has been exploited as ILs to modify the BC characteristics. It has been purchased from Alfa Aesar, and its main properties can be found in [115]. In the following, the material preparation and the capacitor realizations are described.

Realization

The BC membrane employed during this experiment has been produced always by BioFaber s.r.l.s., with the same properties and characteristics of the one presented in Sec. 4.2.1. Additionally to the BC preparation, the membrane has been properly treated to remove the water contained inside it by drying in an oven overnight. Therefore, the membrane has been soaked with EMIM-TFMS for 24 h and then dried in a vacuum oven for 2 h with a fixed temperature of 65 °C. The ILs uptake has been evaluated by comparing the weights of the ILs-treated sample with the dried one and it was about 34%. It has been demonstrated that anion component of the ILs strongly coordinates to the carbohydrates' hydroxyl groups with consequent disruption of inter- and intramolecular hydrogen bonding between cellulose fibrils [116]. Such a consequence allows to justify the high percentage of ILs inside the membrane. Furthermore, due to this strong interaction, cellulose fibrils are easy wetted by diffused ILs at room temperature, determining its swelling and the partial hydrolysis on surface. The BC membrane immersed inside the EMIM-TFMS is shown in Fig. 4.22.

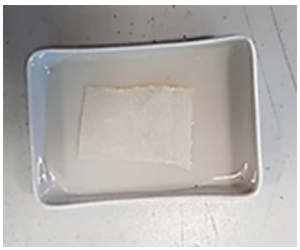

FIGURE 4.22: BC membrane soaked inside the EMIM-TFMS.
Credits: [112]

From the sheet, a square of about 6 mm has been cut and put as dielectrics between two rigid Fr4 copper electrodes (as already presented in Sec. 4.2.1). Furthermore, taking into account the results of Sec. 4.2.3, the realized capacitor has been sealed in a polyethylene sheet and, then, inserted in a polystyrene foam to avoid influences of external agents. The device has been stored in a controlled-temperature chamber at 10 °C. The unassembled device is reported in Fig. 4.23A, while the final setup in Fig. 4.23B.

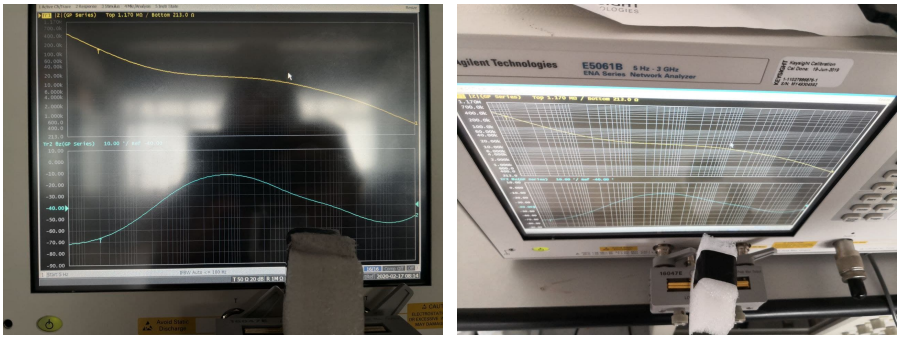

(A) Frontal (B) Perspective

FIGURE 4.24: Picture of a typical measurement with E5061B

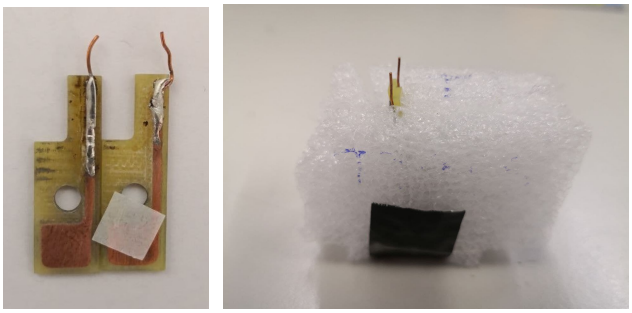

(A) Unassembled device (B) Final setup

FIGURE 4.23: BC-ILs-based FOE setup.
Credits: [112]

The frequency characterization has been performed by using the network analyzer E5061B, with the following setup parameters:

The instrument setup used during the measurement is the following:

- Logarithmic sweep in the range 5 Hz to 30×10^6 Hz;
- Intermediate Frequency Band Width (IFBW): 100 Hz;
- 201 points logarithmically distributed in the investigated domain;
- Averaging factor: 16.

It must be pointed out that starting from 1 MHz inductive parasitic effects occur and so, if it is not explicitly expressed, the identification or the measurement itself are limited to that frequency bound. Each investigation, during the three different campaigns described in the next subsections, has been performed in the same working conditions by removing the sample from the controlled-temperature chamber, exploiting its characteristics with the E5061B and restoring the device again in the chamber. In details, two different perspectives during a typical measurement are shown in Fig. 4.24.

Before going into the details of the aforementioned characterizations, the comparison between the BC-based device and the BC-ILs-based FOE is depicted in Fig. 4.25. It can be easily observed that the presence of ILs decreases the magnitude response of about 40 dB, while the two phase responses are completely different.

In conclusion, it must be pointed out that all the considerations and results presented in the next subsection are related to the same sample, whose investigation started in the end of 2019. This allows also to define a trend in the physical phenomena that occur inside the membrane.

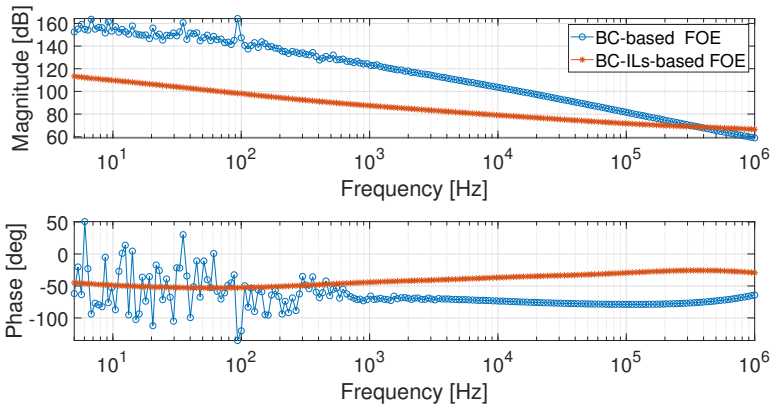

FIGURE 4.25: Bode diagram BC-based device and BC-ILs-based sample

Low frequency range characterization

The first characterization has been realized between the 2019 and the 2020. Starting from the measurement reported in Fig. 4.26 from 5 Hz to 1×10^6 Hz, the sample behaves as a CPE in the low frequency range.

For such a reason, a deeper analysis is restricted to the range 5 Hz to 1000 Hz by performing nineteen different measurements in the same nominal conditions. The obtained magnitude and phase responses are collected in Fig. 4.27.

Analyzing the Bode diagrams, and in particular the phase responses, the BC-IL-based sample exhibits an almost constant-phase response (different from the standard -90 deg) at very low-frequency values. Furthermore, the phase response starts to increase from 100 Hz, requiring also another component besides a fractional-order capacitor. The proposed EECM is made of a FO-RC group, whose configuration is schematized in Fig. 4.28. Such a model has been chosen looking at the device frequency response: at very low frequencies the phase response is almost flat and then it starts to increase. This behaviour, therefore, requires a pole and a zero.

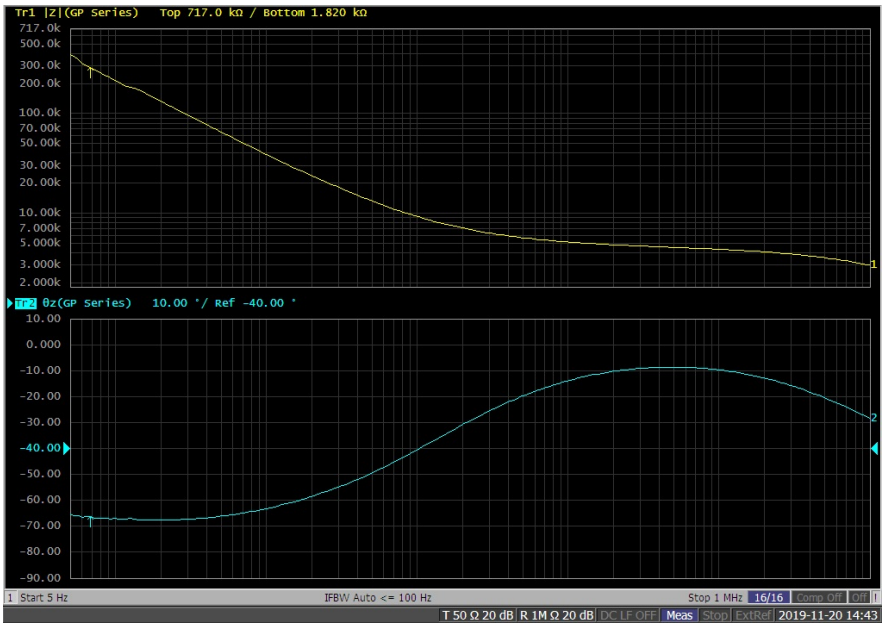

FIGURE 4.26: Screenshot of a BC-ILs-based device frequency response measurement.
Credits: [112]

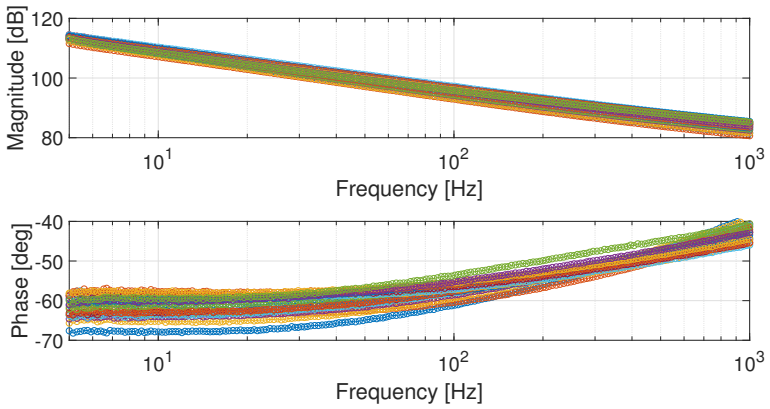

FIGURE 4.27: Bode diagram of the BC-ILs-based FOE restricted to the low frequency range

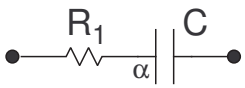

FIGURE 4.28: Proposed EECM

The impedance of the proposed model is represented by (4.5), which is characterized by three different parameters.

$$Z(s) = R_1 + \frac{1}{s^{\alpha}C} \tag{4.5}$$

R_1, C and the α order are identified by means of GAs (whose setup have been defined in Sec. 4.2.2), while the cost function to minimize is described

in (3.4), see Sec. 3.1.2. The box plot of the parameters for all the performed measurements and the averaged ones (in black lines) are shown in Fig. 4.29. In particular, the mean parameters values are listed in Tab. 4.3.

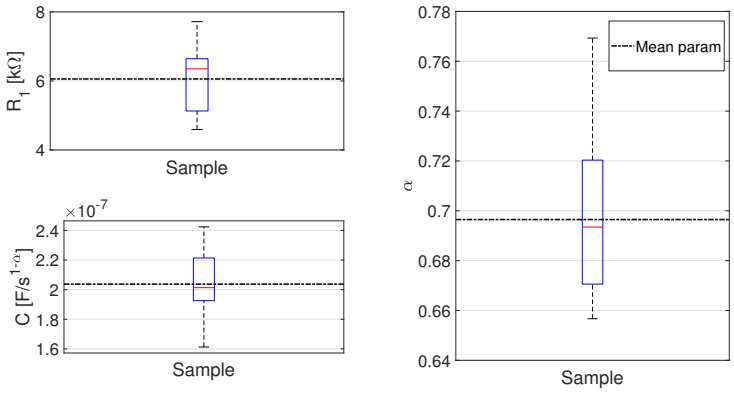

FIGURE 4.29: Box plot and averaged values of the identified parameters for each measurement

Parameter	**Value**
R_1 [kΩ]	6.1
C [nF/s$^{1\text{ - }\alpha}$]	200
α	0.70

TABLE 4.3: Averaged parameter values for the proposed EECM in the low frequency range

To validate the proposed model, both module and phase errors, for each measurement, have been computed with respect to the averaged model. The corresponding maximum errors and their standard deviations have been therefore estimated. As far as the error module concerns, its maximum error and standard deviation are $e_M = 3.6\,\text{dB}$ and $\sigma_M = 0.8\,\text{dB}$, respectively. Instead, for the phase response error, the maximum error and the related standard deviation are $e_\varphi = 9\,\text{deg}$ and $\sigma_\varphi = 2.2\,\text{deg}$.

A further proof of the FC requirement has been performed by trying to model the averaged measurement of the conducted acquisition campaign with a standard capacitor. This simulation has exploited the same GAs optimization procedure and the same cost function, maintaining the same nominal conditions used in the identification of the parameters. Results of such a comparison are depicted in Fig. 4.30, where the measurements are compared with the averaged integer-order model and the fractional-order one, obtained with the parameter of Tab. 4.3. From the figure, it is quite evident that the integer-order model is not able to fit the behaviour of the BC-ILs-based device, while the proposed EECM with the averaged parameters exhibits good approximation capabilities.

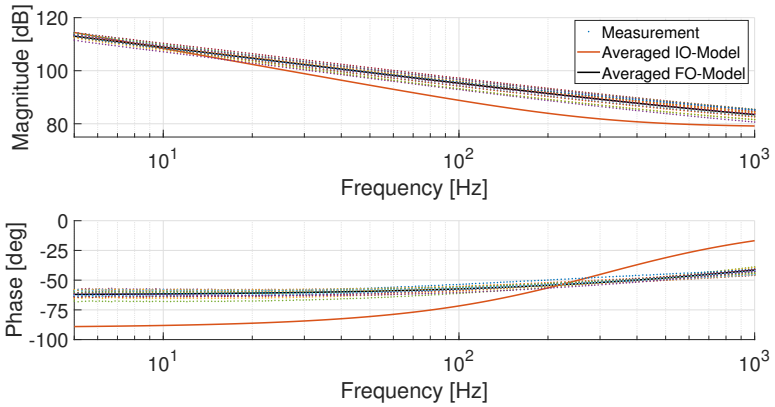

FIGURE 4.30: Bode diagram of each measurement, averaged integer-order model (orange solid line) and averaged fractional-order one (black solid line)

Low and high frequency range characterization

After the low frequency range characterization, a deeper analysis has been executed with the aim of defining a EECM in all the investigated frequency domain, i.e., from 5 Hz to 1×10^6 Hz. Two different measurement campaigns have been conducted, covering a wide interval of time, from September 2019 to March 2020, for an overall period of about 160 days (3900 h). Twenty different observations have been performed in the same nominal conditions. The Bode diagrams are reported in Fig. 4.31 where two clusters can be identified, G_1 and G_2, for the first and the second campaign, respectively. G_1 takes into account the first ten measurement performed in the first month (700 h), while G_2 the remaining ones. Analyzing both the magnitude and the phase responses, a drift effect can be detected: the device has an higher magnitude value and its phase is shifted towards the low frequencies, maintaining the same bell-like shape. Furthermore, although this group has been modeled with the same procedure of G_1, some parameters are not stable with respect to the analysed measurement. For what stated before, even if the entire campaign will be processed and identified, only the observations belonging to G_1 will be deeply investigated.

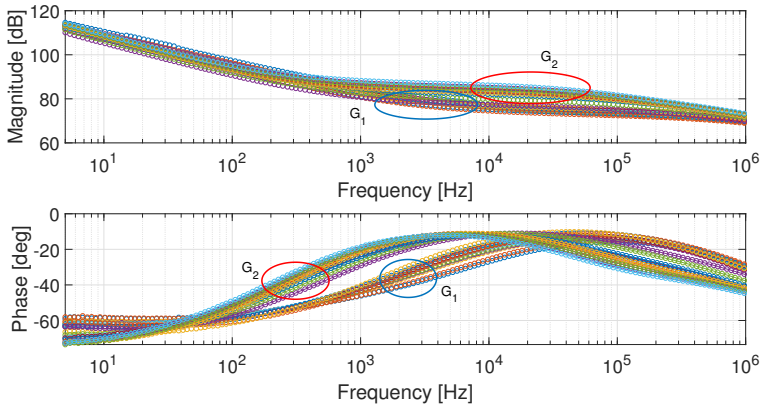

FIGURE 4.31: Bode diagrams of the twenty performed measurements

Additionally, in order to understand the physical phenomena that occur in the BC-ILs-based device, the Nyquist plot has been obtained, see Fig. 4.32. In particular, the circular-like behaviour is due to high-frequency phenomena, while the straight line corresponds to the low-frequencies [117]. The BC-ILs-based device deviates from the nominal behaviour, where a semicircle should be obtained at high frequencies, and a vertical line at the low frequency range. The difference from the nominal case could be addressed to the diffusion process of the mobile charges inside the composite. For this reason, a deeper investigation about the physical phenomena that occur in a polymeric electrolytes has been performed.

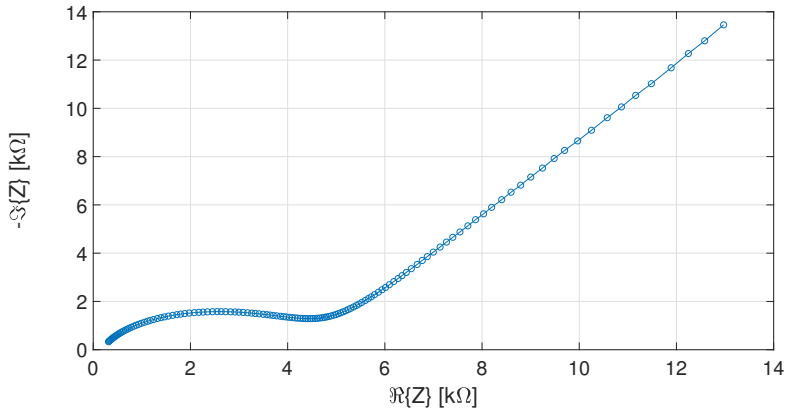

FIGURE 4.32: Nyquist plot of a performed measurement belonging to G_1

A possible model to explain all the diffusive phenomena for polymeric electrolytes has been proposed by Qian et al. [118] and reported in Fig. 4.33. R_1 represents the bulk resistance, C_1 is an IO capacitor that models the geometry of the BC membrane, C_3 is a CPE of order β used for describing the phenomena inside the BC membrane, and C_2, of order α, denotes the double-layer capacitance between the electrodes and the dielectrics. The parallel block made of C_3, C_1 and R_1 determine the high-frequencies behaviour of the device, while the C_2 capacitances the low-frequencies one.

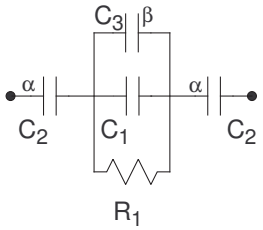

FIGURE 4.33: Proposed EECM for modelling the BC-ILs-based device. Credits: [114]

Evaluating the impedance of Fig. 4.33, its six parameters have been identified by applying the GAs, exploiting the same cost function of the previous case, (3.4). The results of the identification for the two clusters are reported in Fig. 4.34, where the vertical lines divide the G_1 and G_2 groups, respectively. For sake of comparison, one single identified measurement for cluster will be reported in Fig. 4.35. Looking at these diagrams, the model is able

to reproduce correctly the behaviour of the cluster G_1, while some evident mismatches can be detected for the G_2 cluster.

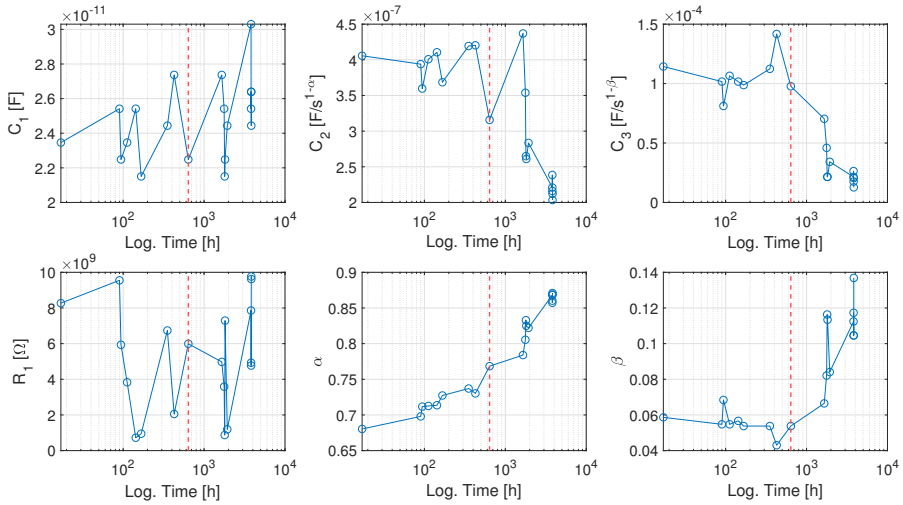

FIGURE 4.34: Parameter trends for the proposed EECM.
Credits: [114]

Furthermore, a quantitative index has been computed for each measurement in order to evaluate the goodness of fit of the performed procedure. The Normalized Root-Mean-Square Error (NRMSE) has been evaluated for both magnitude and phase responses: defining the acquired signal (i.e., measurement) as x_{acq}, and the corresponding estimaned one (i.e., EECM) as x_{est}, the goodness of fit $\mathcal{F}$ is equal to:

$$\mathcal{F} = 1 - \frac{|x_{acq} - x_{est}|}{|x_{acq} - \overline{x_{acq}}|} \tag{4.6}$$

where $\bar{\cdot}$ evaluates the averaged value of its argument. Equation (4.6) is the one's complement of NRMSE and, hence, it provides a value between $[-\infty; 1]$: the smaller the error, the better the quality of fitting. The $\mathcal{F}$ index has been computed both for magnitude and phase responses and they are labelled as $\mathcal{F}_{\mathcal{M}}$ and $\mathcal{F}_{\varphi}$, respectively. Their values are listed in Tab. 4.4. As stated before, for the measurements belonging to G_1, the fitting capabilities of the proposed EECM are satisfactory, providing results of about 95 % for both $\mathcal{F}_{\mathcal{M}}$ and $\mathcal{F}_{\varphi}$. On the other hand, the EECM performance for G_2 are worst: despite of a well-identified magnitude response, the phase response of the device is not correctly fitted. Therefore, the derive effect in G_2 is the cause for which the proposed EECM is not capable to represent correctly the BC-ILs-based device dynamics.

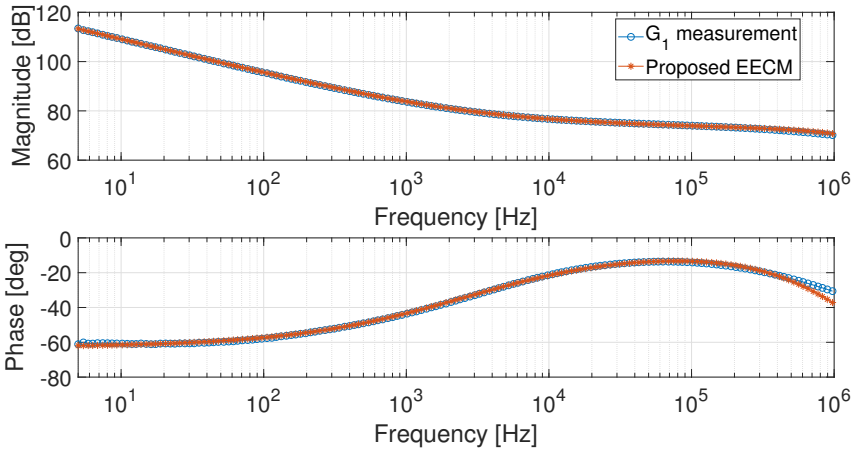

(A) Fitting measurement beloning to G_1

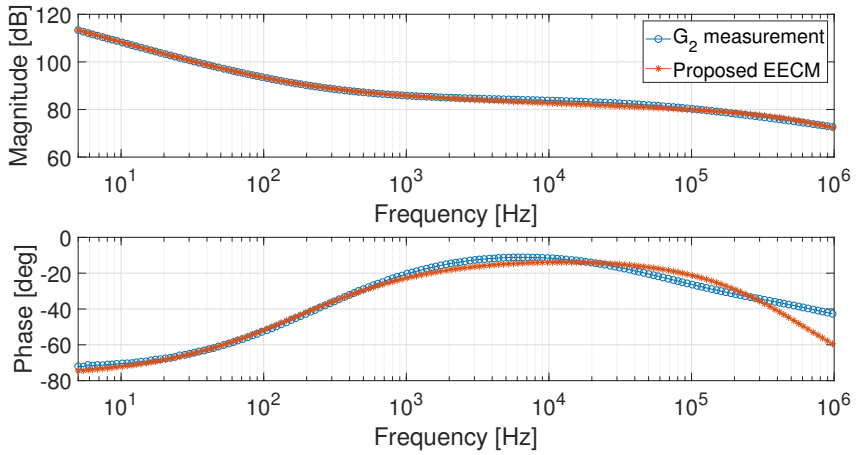

(B) Fitting measurement beloning to G_2

FIGURE 4.35: Comparison between proposed EECM and measurement Bode diagrams for G_1 and G_2

Measurement	$\mathcal{F}_{\mathcal{M}}$	$\mathcal{F}_{\varphi}$
1 - 0 h	0.9641	0.9578
2 - 17 h	0.9850	0.9514
3 - 90 h	0.9920	0.9390
4 - 94 h	0.9914	0.9582
5 - 112 h	0.9922	0.9538
6 - 143 h	0.9928	0.9486
7 - 167 h	0.9855	0.9505
8 - 352 h	0.9916	0.9554
9 - 427 h	0.9885	0.9265
10 - 639 h	0.9347	0.9587
11 - 1654 h	0.9888	0.8785
12 - 1770 h	0.9749	0.8890
13 - 1798 h	0.9860	0.8604
14 - 1817 h	0.9773	0.8514
15 - 1935 h	0.9766	0.8449
16 - 3808 h	0.9868	0.8020
17 - 3809 h	0.9839	0.8383
18 - 3814 h	0.9875	0.7843
19 - 3831 h	0.9902	0.7997
20 - 3832 h	0.9838	0.7702

TABLE 4.4: Goodness of fit values for the two clusters G_1 and G_2

A final analysis has been performed to understand the role of the employed components in the EECM schematized in Fig. 4.33. For this purpose, three different reduced models have been studied by removing, once at time, the three different capacitors. They are labelled as EECM-1, EECM-2, and EECM-3, where C_1, C_2 and C_3 are not inserted in the model, respectively. In details, in EECM-1 and EECM-3, the eliminated capacitors have been replaced by open circuits, while in EECM-2 by a short circuit. The impedances of the three reduced circuits have been computed and their parameters have been identified with the same procedure for the complete EECM. Results of this comparison are shown in Fig. 4.36, where, as reference, the first measurement of G_1 has been considered.

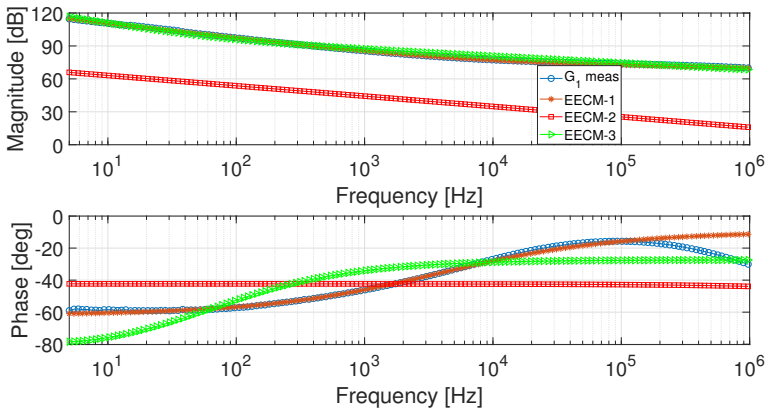

FIGURE 4.36: Comparison of reduced EECMs for a G_1 measurement

Although EECM-1 is capable to reproduce correctly the magnitude response of the device, its phase response exhibits an increasing error with respect to the frequency, up to a maximum error of about 20 deg. Worst results are obtained with EECM-2, both in the magnitude and in the phase responses. Finally, the comparison with EECM-3 can be discussed. Also in this case, the magnitude response is almost fit well, while the phase one is completely different from the real measurement.

In conclusion, the conducted analysis allows to validate the proposed model, highlighting that none of the capacitors can be removed without loosing good fitting capabilities, although the device behaviour derives over time.

BC-ILs-based device as CPE

From the characterizations described until now, it emerges that the device acts as FOE because it cannot be modeled properly by means of IO-capacitors. However, except for a limited frequency domain, it does not exhibit a CPE behaviour.

The same sample, whose first observation has been performed in the 2019, has been further subjected to a third measurement campaign from September 2020 to November 2020, covering an overall investigation period greater than a year. The gap of six months is due to the outbreak of COVID-19 that has not allowed to access to the university laboratories. Therefore, the device has been stored in the controlled-temperature chamber for six months without any external disturbances or influences. When the access to the laboratories has been guaranteed, in September 2020 another measurement of the same sample was performed (with the same experimental setup) with the aim to verify if the device had found an electrical stability. The screenshot of the measurement is reported in Fig. 4.37. Although the magnitude response has almost maintained the same shape of the previous observations, the phase response is completely different, showing a constant phase for about four decades, starting from the low frequencies. For these preliminary results, it seems that the material requires a cooling period to achieve this behaviour.

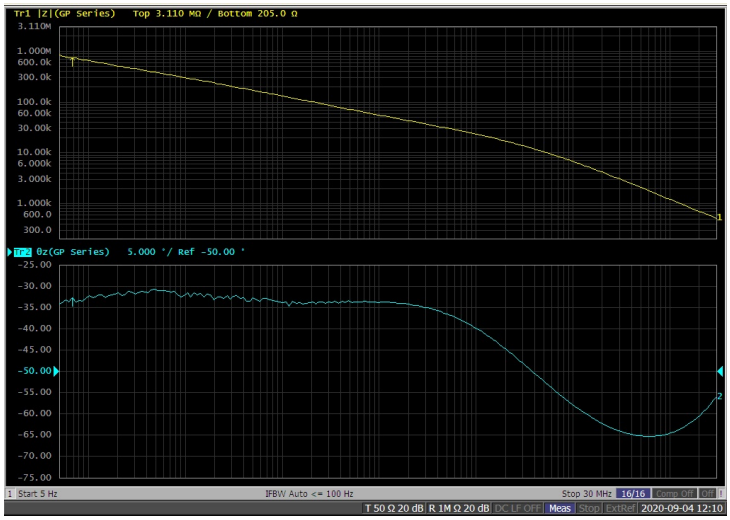

FIGURE 4.37: Screenshot of BC-ILs-based device measurement performed on 09/2020.
Credits: [113]

A comparison of the Bode diagram for the three different campaigns is shown in Fig. 4.38. G_1 takes into account the measurements performed from September 2019 to October 2019, G_2 the observations from December 2019 to March 2020, while G_3 from September 2020 to November 2020. From the diagrams, it can be observed that G_3 has an higher phase-lag from the other two clusters. Furthermore, no magnitude slope changes can be detected in G_3, while it occurs both in G_1 and G_2. For this reasons, the measurement campaign has been conducted for about three months in order to understand the stability of this new behaviour.

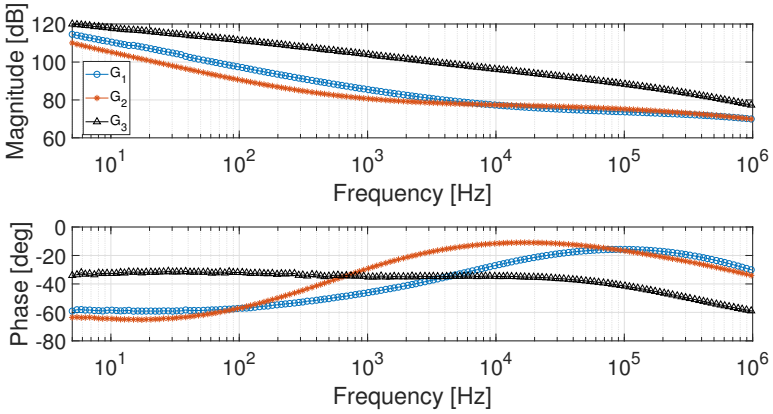

FIGURE 4.38: Bode diagrams for the three measurement campaigns G_1 (2019/09 to 2019/10), G_2 (2019/12 to 2020/03) and G_3 (2020/09 to 2020/11)

More specifically, thirty-two measurements have been performed in the same nominal conditions with the same experimental setup. The obtained observations from 5 Hz to 1×10^6 Hz are drawn in Fig. 4.39: in all of them it is possible to detect a flat phase zone of about -35 deg from 5 Hz to 1×10^4 Hz. Additionally, no significant dispersion can be detect both in the magnitude and in the phase responses. The former has a maximum difference of about 7 dB, while the latter of about 7 deg.

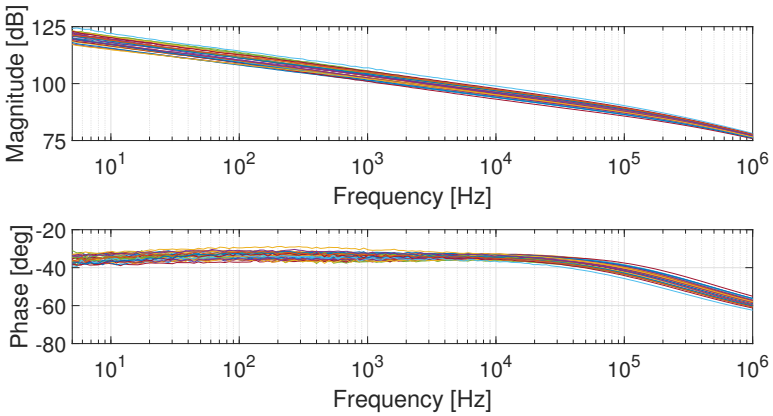

FIGURE 4.39: Bode diagrams for the thirty-two measurements of the BC-ILs-based device

The identification procedure has been restricted to the frequency range where the device acts as a CPE in the same working conditions. In this case, the GAs have to identify only two parameters. Furthermore, in this measurement campaign, the objective function $\mathcal{J}$ has been computed by taking into account the NRMSE for both the magnitude and phase responses that have been already defined as $\mathcal{F}_{\mathcal{M}}$ and $\mathcal{F}_{\varphi}$. Hence, by putting $w_1 = w_2 = 0.5$, the cost function can be evaluated as follows:

$$\mathcal{J} = w_1 \mathcal{F}_{\mathcal{M}} + w_2 \mathcal{F}_{\varphi} \tag{4.7}$$

The parameters of the whole dataset have been computed and reported, as boxplot, in Fig. 4.40, while in solid black lines the averaged values (i.e., $\mathrm{C} = 266.8\,\mathrm{nF/s^{1-\alpha}}$ and $\alpha = 0.378$) are drawn. Therefore, in Fig. 4.41 a comparison between a performed measurement and its equivalent model response is depicted, where a phase ripple of about $\pm 2\,\mathrm{deg}$ can be observed. Such a value is in accordance with the phase ripple of other CPEs realized and discussed in the previous chapter, giving validity to define the sample as CPE.

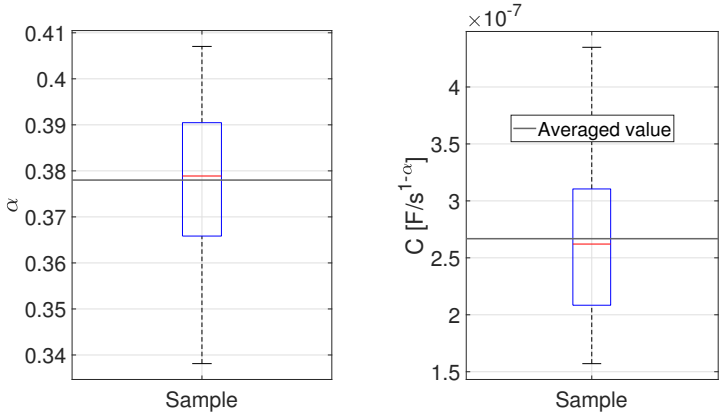

FIGURE 4.40: Box plot of BC-ILs-based device for the G_3 dataset

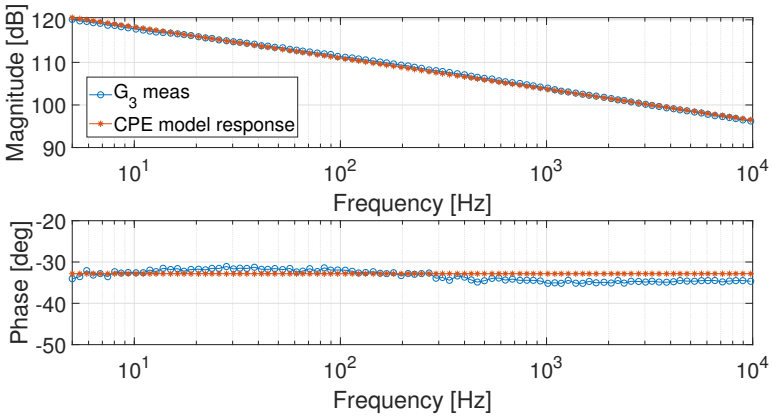

FIGURE 4.41: Bode diagrams of a G_3 measurement and related simulated response

With the aim of validating the proposed model, the averaged parameters have been exploited and compared with the entire G_3 cluster (reported as dotted markers), see Fig. 4.42. From the averaged model, the maximum errors have been computed for both the magnitude and the phase responses. As far as the magnitude response error concerns, the maximum residual is e_M = 4.763 dB with a standard deviation of σ_M of 1.013 dB, while the maximum phase error is equal to e_φ = 5.399 deg with σ_φ = 1.325 deg.

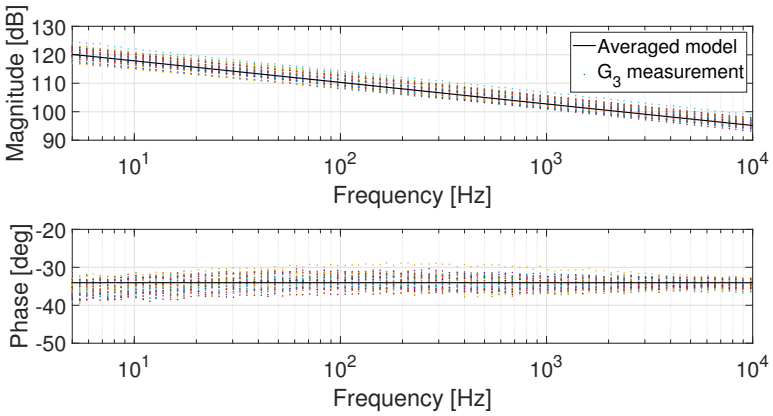

FIGURE 4.42: Bode diagrams of obtained CPE model (solid line) and a G_3 measurements (dotted marked)

As final study, the device has been used in a RC filter implementation furnishing, as input, a square wave between 0 V and 1 V. However, the filter response has not been in accordance with its EECM. Probably, when the input has been provided, the charges motion has abruptly changed the device internal thermal equilibrium, determining a different response. For such a reason, some new observations of the device have been taken and compared with the nominal behaviour. Therefore, the sample has been stored again in the temperature-controlled chamber and three measurements have been performed in order to verify its recover capabilities. The results of this study are represented in Fig. 4.43

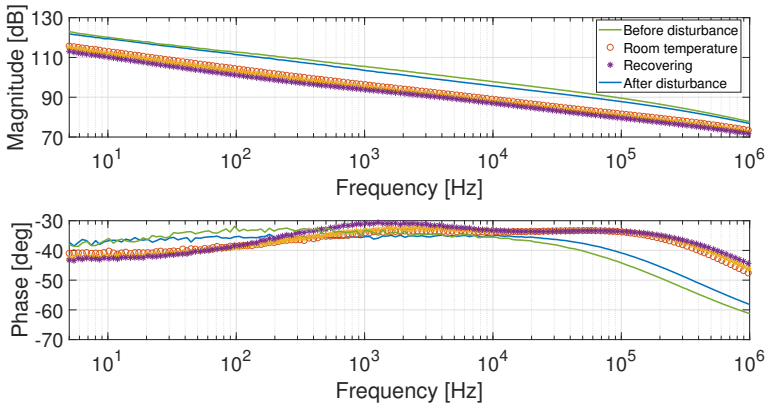

FIGURE 4.43: Bode diagrams of the BC-ILs-based device before, during and after the external temperature variation

Looking at the figure, the device has a different magnitude response with a lower intensity after its employment in the filter implementation. This new performance can be justified by a variation in the dielectrics viscosity that, due to the provided energy and, hence, to an higher internal temperature, allows the mobile charges to move easily. Furthermore, also a decreasing of the phase response can be observed, loosing the flat zone in the low frequency range. It must be pointed out that the device has not shown a fast recovery capability. Indeed, the asterisk-marked responses have been taken after 8 h and 48 h that the device has been restored in the temperature-controlled chamber, and no significant difference can be detected. For such a reason, the next measurement (reported as green solid line) has been performed one week later the implementation test, and it can be stated that the device has almost restored its previous behaviour. Therefore, two up to seven days are necessary to restore the BC-ILs-based sample conditions from temperature variations: the diffusive phenomena which determine its fractional-order nature have a very slow dynamics. In addition, the realized device cannot be used in real circuit implementation with typical laboratory conditions.

Among the performance variation explanations and, hence, to propose a proper device engineerization, a possible phenomenon to study can be due the membrane degradation process, see Fig. 4.44. The contact between the membrane and the copper electrodes determines some chemical reactions where, due to the presence of ions inside, copper (or carbonates) salts are created and deposited in the membrane itself, giving it a blueish colour. This phenomenon has been retrieved both using the EMIM-TFMS, see Fig. 4.44, and other ILs, as reported in App. A. In particular, the device represented in Fig. 4.44 is another sample of BC imbibed with EMIM-TFMS, mounted in a parallel-plate configuration and kept at room temperature.

Another important aspect to consider is related to the low temperature at which the device is stored. Indeed, the temperature is responsible for slowing down the described reaction between the electrodes and the membrane, as the analysis performed in the entire year have demonstrated. On the other hand, the temperature limits the possible applications of the BC-ILs-based FOE.

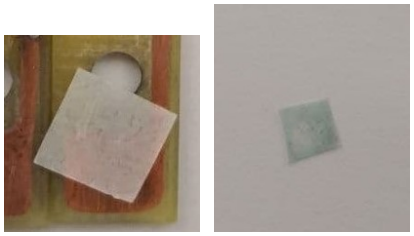

(A) Unused BC (B) Mounted BC

FIGURE 4.44: Comparison between the unused BC (left) and the mounted membrane inside the copper cards

Chapter 5

Conclusions

The proposed thesis analyses the possibility of exploiting the Fractional Calculus as a new framework in the automatic control field. In particular, its advantages have been widely described in the first chapter, highlighting the differences with the standard Integer Calculus.

Two main purposes for the conducted research can be detected: the realization of new capacitors (integrators) with new functionalities and the possibility of developing such capacitors also in an eco-friendly way. Starting from an overview of the state of art about the physical phenomena and possible realization of Fractional-Order Capacitors (or Constant-Phase Elements), the attention has been paid in the CPE realization by means of a solid-state technology.

The CB-based devices, presented in the third chapter, employ the Carbon Black particles which are diffused inside a polymeric dielectrics matrix. The capacitors have been realized by varying some technological parameters with the aim to find out a well-described relationship between the fractional-order α and the investigated parameters. Even if not significant trend has been detected, a group classification, discriminated by the Curing Temperature, has been discovered. Among the realized devices, two capacitors with different CB percentage and Curing Temperatures have been modeled as CPEs and deeply studied in several applications, from simple RC circuit to a real fractional-order controller.

Thanks to the fractional-order of the capacitor, it has been possible to realize a full analog closed-loop system robust towards gain and pole plant variations (see Ch. 3), providing a constant overshoot and a constant open-loop phase response in an entire decade. Results of the possible implementation of this technology are very encouraging, also due to their long-time stability. They can be thought as a starting point for future research developments, such as the packaging miniaturization or the investigation of other technological parameters that can determine the device fractional-order behaviour.

The other proposed technology deals with Bacterial Cellulose, an organic compound widely studied in different application fields. The choice of this material allows to realize a eco-friendly device compared to the Carbon Black-based ones. Thanks to the BC porous structure, the parallel-plate capacitor exploits a fractional-order behaviour, broadly characterized both in typical laboratory conditions and in controlled environment (i.e., avoiding temperature and relative humidity influences). Furthermore, its characteristics has been changed by imbibing the membrane with several Ionic Liquids, providing different frequency responses. More specifically, among the analysed ILs, the EMIM-TFMS has shown very interesting frequency responses. Although the device lacks of stability, after the COVID-19 lockdown (March 2020) it has shown a constant-phase response from the low frequency, covering about four decades and maintaining this behaviour for more than three months. Also in this case, results are very encouraging because this class of devices can be realized without wasting too much energy and employing less pollutant compared to the standard electronics. Future possible developments of the conducted research could be the possibility of substituting the copper electrodes, exploiting other eco-friendly ILs, studying a possible engineerization process for the physical phenomena that have make the device a CPE, trying also to overcame the stability issues and the sensitivity to external agents.

Appendix A

Investigated Ionic Liquids

In this Appendix, the other Ionic Liquids in which the BC membrane has been immersed will be presented. Several proofs have been done by changing the cation or the anion of the investigated ILs in order to understand how the frequency response of the realized device varies. Unfortunately, no significant results have been achieved.

For each presented device, the same realization procedure described in the Ch. 4 has been fulfilled. Furthermore, they have been stored inside the temperature-controlled chamber at 10 °C and investigated in the same working conditions. After the measurement, they have been restored inside the chamber.

A.1 EMIM-BF4

The first tested ILs is made of 1-Ethyl-3-Methylimidazolium tetrafluoroborate (EMIM-BF4). These ILs have been chosen in order to analyze how the BC-based device changes its frequency response by varying the anion (BF4 instead of TFMS) of the already studied EMIM-TFMS. Twenty-eight measurements have been performed from September 2019 to September 2020 for the same device. For sake of clarity, only one measurement for each campaign will be reported. Also in this case, the frequency response that derives over time, without obtaining any flat phase zone. Furthermore, also the degradation process has been observed for this device, as depicted in Fig. A.2.

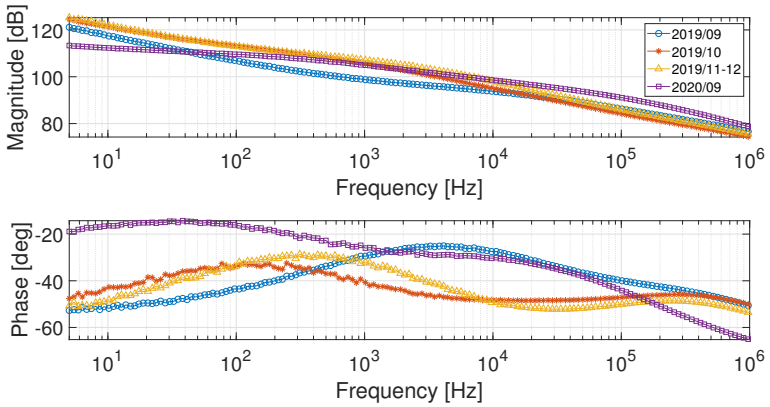

FIGURE A.1: Bode diagrams of the BC-EMIM-BF4-based device

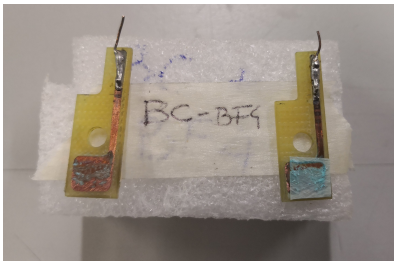

FIGURE A.2: BC-EMIM-BF4 degraded membrane

A.2 EMIM-BF4-TFMS

Another device has been realized by a proper mixture of the EMIM-TFMS and EMIM-BF4. Twenty-two measurements have been performed from October 2019 to September 2020 for the same device. For sake of clarity, only one measurement for each campaign will be reported. As for the EMIM-BF4, the device response derives over time, without obtaining any flat phase zone. Furthermore, also the degradation process can be detected after its opening one year after its assembly, as depicted in Fig. A.4.

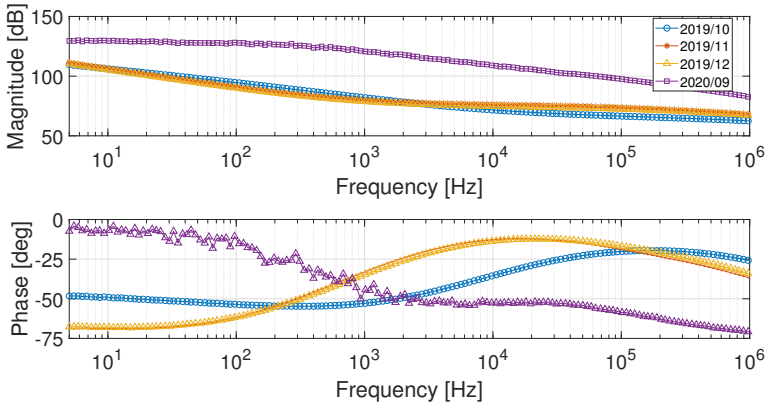

FIGURE A.3: Bode diagrams of the BC-EMIM-TFMS-BF4-based device

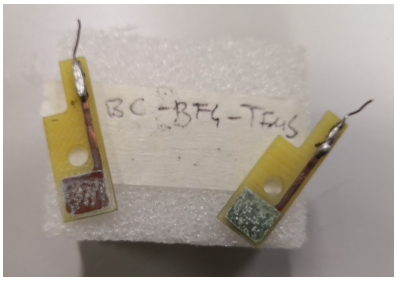

FIGURE A.4: BC-EMIM-TFMS-BF4 degraded membrane

A.3 HEXYL-CL

With the aim of testing other ILS, the Hexyl chloroformate (HEXYL-CL) has been diffused inside the BC membrane. In particular, the employed membrane (cut as roughly square of about 6 mm) has a thickness slightly higher than the one employed in Ch. 4 ($\sim 0.51\,\mu m$). The device has been mounted in September 2019 and only seven measurements have been taken because, as reported in Fig. A.5, it shows a more resistive behaviour (the phase approaches the zero value). Therefore, one month after it has been opened, showing a degradation process, see Fig. A.6. In this case, the greenish colour is due to the different nature of the diffused ILs.

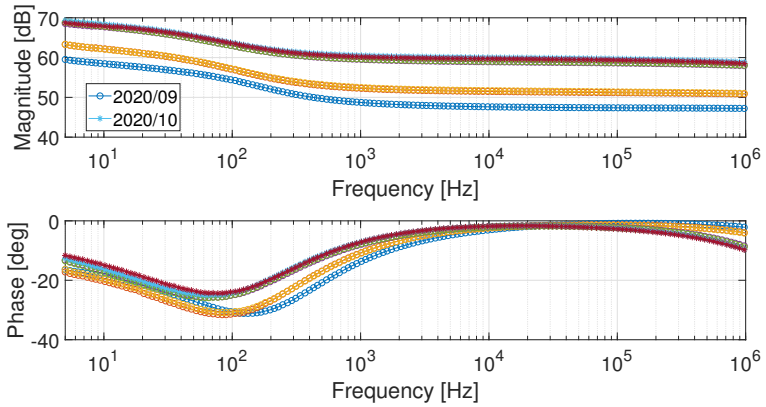

FIGURE A.5: Bode diagrams of the BC-HEXYL-CL-based device

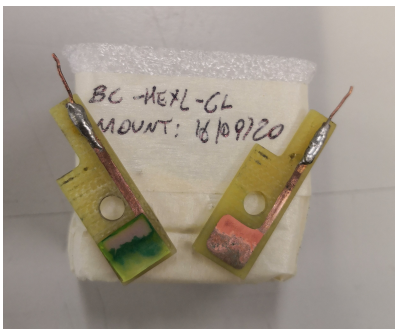

FIGURE A.6: BC-HEXYL-CL degraded membrane

A.4 EMIM-CL

The 1-Ethyl-3-Methylimidazolium Chloroformate (EMIM-CL) has been tested in order to understand how a different cation (i.e., EMIM or HEXYL) can influence the BC-based device behaviour. So, from the same BC matrix, a part of the membrane has been imbibed with the EMIM-CL. The obtained Bode diagrams are depicted in Fig. A.7, after sixteen performed measurements from September 2020 to November 2020. It can be noticed that the high frequencies behaviour of the BC-HEXYL-CL and BC-EMIM-CL is qualitative quite similar (although the magnitude intensities assume different values), while in the low frequencies the two phase responses are different.

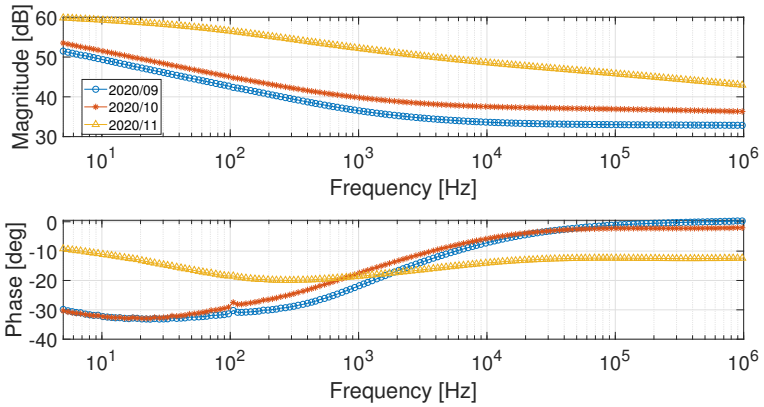

FIGURE A.7: Bode diagrams of the BC-EMIM-CL-based device

A.5 CHMAL

The last tested ILs are based on Carboxydothermus hydrogenoforomans 3-methylaspartate ammonia lyase (ChMal). Seven measurements have been tested from September to October 2020. Due to its complete different nature with respect to the other ILs, all the seven measurements are depicted in Fig. A.8. It can be obseverd that the device was not stable in the first month. After, a stability has been reached, even if the response does not belong to the CPEs cluster. After the month of investigation, the device has been opened and, also in this case, a degradation of the membrane can be identified (a region of the membrane is more glossy).

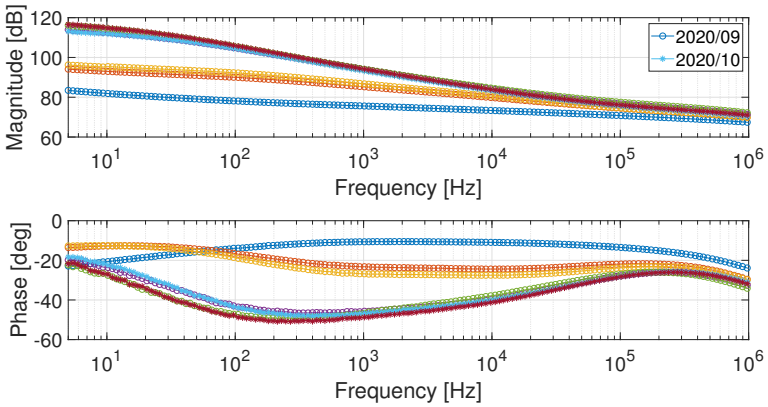

FIGURE A.8: Bode diagrams of the BC-Ch-Mal-based device

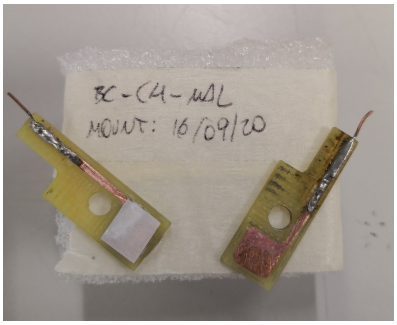

FIGURE A.9: BC-Ch-Mal degraded membrane

Bibliography

[1] K. B. Oldham and J. Spanier, *The Fractional Calculus: Theory and Applications of Differentiation and Integration to Arbitrary Order*, 1st ed., ser. Mathematics in science and engineering 111. Academic Press, 1974.

[2] A. Atangana and D. Baleanu, "New fractional derivatives with non-local and non-singular kernel: Theory and application to heat transfer model," *Therm Sci*, vol. 20, pp. 763 –769, 2016. DOI: 10.2298/TSCI160111018A.

[3] M. Caputo and M. Fabrizio, "A new definition of fractional derivative without singular kernel," *Prog Fract Differ Appl*, vol. 1, no. 2, pp. 73 –85, 2015.

[4] R. A. Askey and R. Roy, *Gamma function*, Accessed on the 22th June 2021. [Online]. Available: https://dlmf.nist.gov/5.2.

[5] A. L. Cauchy, "Trente-cinquième leçon," in *Résumé des leçons données à l'Ecole royale polytechnique sur le calcul infinitésimal*, Reprint: Œuvres complètes II(4), Gauthier-Villars, Paris, pp. 5–261., Imprimerie Royale, 1823.

[6] C. A. Monje, Y. Chen, B. M. Vinagre, D. Xue, and V. Feliu, *Fractional-order Systems and Controls: Fundamentals and Applications*, 1st ed., ser. Advances in Industrial Control. Springer-Verlag London, 2010.

[7] R. Caponetto, G. Dongola, L. Fortuna, and I. Petráš, *Fractional Order Systems*. World Scientific, 2010. DOI: 10.1142/7709.

[8] J. Sabatier, C. Farges, and J.-C. Trigeassou, "Fractional systems state space description: Some wrong ideas and proposed solutions," *Journal of Vibration and Control*, vol. 20, no. 7, pp. 1076–1084, 2014. DOI: 10.1177/1077546313481839.

[9] A. Charef, H. Sun, Y. Tsao, and B. Onaral, "Fractal system as represented by singularity function," *IEEE Transactions on Automatic Control*, vol. 37, no. 9, pp. 1465–1470, 1992. DOI: 10.1109/9.159595.

[10] A. Oustaloup, "Fractional order sinusoidal oscillators: Optimization and their use in highly linear fm modulation," *IEEE Transactions on Circuits and Systems*, vol. 28, no. 10, pp. 1007–1009, 1981. DOI: 10.1109/TCS.1981.1084917.

[11] K. Matsuda and H. Fujii, "H(infinity) optimized wave-absorbing control - Analytical and experimental results," *Journal of Guidance, Control, and Dynamics*, vol. 16, pp. 1146–1153, 1993. DOI: 10.2514/3.21139.

[12] R. Caponetto, J. T. Machado, E. Murgano, and M. G. Xibilia, "Model order reduction: A comparison between integer and non-integer order systems approaches," *Entropy*, vol. 21, no. 9, 2019. DOI: 10.3390/e21090876.

[13] V. E. Tarasov and V. V. Tarasova, "Criterion of existence of power-law memory for economic processes," *Entropy*, vol. 20, no. 6, 2018. DOI: 10.3390/e20060414.

[14] D. A. Benson, M. M. Meerschaert, and J. Revielle, "Fractional calculus in hydrologic modeling: A numerical perspective," *Advances in Water Resources*, vol. 51, pp. 479–497, 2013, 35th Year Anniversary Issue. DOI: 10.1016/j.advwatres.2012.04.005.

[15] C. Vastarouchas, G. Tsirimokou, T. J. Freeborn, and C. Psychalinos, "Emulation of an electrical-analogue of a fractional-order human respiratory mechanical impedance model using ota topologies," *AEU - International Journal of Electronics and Communications*, vol. 78, pp. 201–208, 2017. DOI: 10.1016/j.aeue.2017.03.021.

[16] H. Sun, Y. Zhang, D. Baleanu, W. Chen, and Y. Chen, "A new collection of real world applications of fractional calculus in science and engineering," *Communications in Nonlinear Science and Numerical Simulation*, vol. 64, pp. 213–231, 2018, ISSN: 1007-5704. DOI: 10.1016/j.cnsns.2018.04.019.

[17] I. Podlubny, "Fractional-order systems and $PI^{\lambda}D^{\mu}$-controllers," *IEEE Transactions on Automatic Control*, vol. 44, no. 1, pp. 208–214, 1999. DOI: 10.1109/9.739144.

[18] A. Oustaloup, O. Cois, P. Lanusse, P. Melchior, X. Moreau, and J. Sabatier, "The CRONE approach: Theoretical developments and major applications," *IFAC Proceedings Volumes*, vol. 39, no. 11, pp. 324–354, 2006, 2nd IFAC Workshop on Fractional Differentiation and its Applications. DOI: 10.3182/20060719-3-PT-4902.00059.

[19] G. W. Bohannan, "Analog fractional order controller in temperature and motor control applications," *Journal of Vibration and Control*, vol. 14, no. 9-10, pp. 1487–1498, 2008. DOI: 10.1177/1077546307087435.

[20] R. De Keyser, C. I. Muresan, and C. M. Ionescu, "A novel autotuning method for fractional order pi/pd controllers," *ISA Transactions*, vol. 62, pp. 268–275, 2016, SI: Control of Renewable Energy Systems. DOI: 10.1016/j.isatra.2016.01.021.

[21] A. Tepljakov, B. B. Alagoz, C. Yeroglu, E. Gonzalez, S. H. HosseinNia, and E. Petlenkov, "Fopid controllers and their industrial applications: A survey of recent results," *IFAC-PapersOnLine*, vol. 51, no. 4, pp. 25–30, 2018, 3rd IFAC Conference on Advances in Proportional-Integral-Derivative Control PID 2018. DOI: 10.1016/j.ifacol.2018.06.014.

[22] I. Birs, C. Muresan, I. Nascu, and C. Ionescu, "A survey of recent advances in fractional order control for time delay systems," *IEEE Access*, vol. 7, pp. 30 951–30 965, 2019. DOI: 10.1109/ACCESS.2019.2902567.

[23] R. De Keyser, C. I. Muresan, and C. M. Ionescu, "Autotuning of a robust fractional order pid controller," *IFAC-PapersOnLine*, vol. 51, no. 25, pp. 466–471, 2018, 9th IFAC Symposium on Robust Control Design ROCOND 2018. DOI: 10.1016/j.ifacol.2018.11.181.

[24] Z. Wu, D. Li, Y. Xue, T. He, and S. Zheng, "Tuning for fractional order pid controller based on probabilistic robustness," *IFAC-PapersOnLine*, vol. 51, no. 4, pp. 675–680, 2018, 3rd IFAC Conference on Advances in Proportional-Integral-Derivative Control PID 2018. DOI: 10.1016/j.ifacol.2018.06.179.

[25] F. Padula and A. Visioli, "Tuning rules for optimal pid and fractional-order pid controllers," *Journal of Process Control*, vol. 21, no. 1, pp. 69–81, 2011. DOI: 10.1016/j.jprocont.2010.10.006.

[26] A. Tepljakov, B. B. Alagoz, C. Yeroglu, E. A. Gonzalez, S. H. Hosseinnia, E. Petlenkov, A. Ates, and M. Cech, "Towards industrialization of fopid controllers: A survey on milestones of fractional-order control and pathways for future developments," *IEEE Access*, vol. 9, pp. 21 016–21 042, 2021. DOI: 10.1109/ACCESS.2021.3055117.

[27] C. Reece, *An introduction to Electrochemical Impedance Spectroscopy (EIS)*, Accessed on 25th June 2021. [Online]. Available: https://www.jlab.org/conferences/tfsrf/Thursday/Th2_1-EIS%20intro%20Reece.pdf.

[28] V. Encinas-Sánchez, M. de Miguel, M. Lasanta, G. García-Martín, and F. Pérez, "Electrochemical impedance spectroscopy (eis): An efficient technique for monitoring corrosion processes in molten salt environments in csp applications," *Solar Energy Materials and Solar Cells*, vol. 191, pp. 157–163, 2019. DOI: 10.1016/j.solmat.2018.11.007.

[29] P. Leuaa, D. Priyadarshani, D. Choudhury, R. Maurya, and M. Neergat, "Resolving charge-transfer and mass-transfer processes of vo2+/vo2+ redox species across the electrode/electrolyte interface using electrochemical impedance spectroscopy for vanadium redox flow battery," *RSC Adv.*, vol. 10, pp. 30 887–30 895, 51 2020. DOI: 10.1039/D0RA05224H.

[30] M. Lacey, *The constant phase element*, Accessed on 25th June 2021. [Online]. Available: http://lacey.se/science/eis/constant-phase-element/.

[31] E. W. Weisstein, *Euler formula*, From MathWorld–A Wolfram Web Resource, Accessed on 25th June 2021. [Online]. Available: https://mathworld.wolfram.com/EulerFormula.html.

[32] M. E. Orazem and B. Tribollet, "Constant-phase elements," in *Electrochemical Impedance Spectroscopy*, 2nd ed., John Wiley & Sons, Inc, 2017, ch. 14, pp. 395–419.

[33] J. Jean, "The phasance concept: A review," *Current Topics in Electrochemistry*, vol. 4, pp. 127 –136, 1997.

[34] Y. Sudhakar, M. Selvakumar, and D. K. Bhat, "Chapter 3 - Biopolymer Electrolyte for Supercapacitor," in *Biopolymer Electrolytes*, Y. Sudhakar, M. Selvakumar, and D. K. Bhat, Eds., Elsevier, 2018, pp. 53–116. DOI: 10.1016/B978-0-12-813447-4.00003-0.

[35] J. López-García, J. Horno, and C. Grosse, "Differential capacitance of the diffuse double layer at electrode-electrolyte interfaces considering ions as dielectric spheres: Part i. binary electrolyte solutions," *Journal of Colloid and Interface Science*, vol. 496, pp. 531–539, 2017, ISSN: 0021-9797. DOI: 10.1016/j.jcis.2017.02.043.

[36] R. De Levie, "The influence of surface roughness of solid electrodes on electrochemical measurements," *Electrochimica Acta*, vol. 10, no. 2, pp. 113–130, 1965, ISSN: 0013-4686. DOI: 10.1016/0013-4686(65)87012-8.

[37] W. Mulder, J. H. Sluyters, T. Pajkossy, and L. Nyikos, "Tafel current at fractal electrodes: Connection with admittance spectra," *Journal of Electroanalytical Chemistry*, vol. 285, pp. 103–115, 1990.

[38] L. Nyikos and T. Pajkossy, "Fractal dimension and fractional power frequency-dependent impedance of blocking electrodes," *Electrochimica Acta*, vol. 30, no. 11, pp. 1533–1540, 1985. DOI: 10.1016/0013-4686(85)80016-5.

[39] S. M. Rezaei Niya and M. Hoorfar, "On a possible physical origin of the constant phase element," *Electrochimica Acta*, vol. 188, pp. 98–102, 2016, ISSN: 0013-4686. DOI: 10.1016/j.electacta.2015.11.142.

[40] J.-B. Jorcin, M. E. Orazem, N. Pébère, and B. Tribollet, "CPE analysis by local electrochemical impedance spectroscopy," *Electrochimica Acta*, vol. 51, no. 8, pp. 1473–1479, 2006. DOI: 10.1016/j.electacta.2005.02.128.

[41] G. Brug, A. van den Eeden, M. Sluyters-Rehbach, and J. Sluyters, "The analysis of electrode impedances complicated by the presence of a constant phase element," *Journal of Electroanalytical Chemistry and Interfacial Electrochemistry*, vol. 176, no. 1, pp. 275–295, 1984. DOI: 10.1016/S0022-0728(84)80324-1.

[42] P. Ushakov, A. Shadrin, D. Kubanek, and J. Koton, "Passive fractional-order components based on resistive-capacitive circuits with distributed parameters," in *2016 39th International Conference on Telecommunications and Signal Processing (TSP)*, 2016, pp. 638–642. DOI: 10.1109/TSP.2016.7760960.

[43] S. Westerlund and L. Ekstam, "Capacitor theory," *IEEE Transactions on Dielectrics and Electrical Insulation*, vol. 1, no. 5, pp. 826–839, 1994. DOI: 10.1109/94.326654.

[44] A. Allagui, T. J. Freeborn, A. S. Elwakil, M. E. Fouda, B. J. Maundy, A. G. Radwan, Z. Said, and M. A. Abdelkareem, "Review of fractional-order electrical characterization of supercapacitors," *Journal of Power Sources*, vol. 400, pp. 457–467, 2018. DOI: 10.1016/j.jpowsour.2018.08.047.

[45] K. S. Cole and R. H. Cole, "Dispersion and absorption in dielectrics i. alternating current characteristics," *J. Chem. Phys.*, vol. 9, no. 341, pp. 341 –351, 1941. DOI: 10.1063/1.1750906.

[46] Z. M. Shah, M. Y. Kathjoo, F. A. Khanday, K. Biswas, and C. Psychalinos, "A survey of single and multi-component Fractional-Order Elements (FOEs) and their applications," *Microelectronics Journal*, vol. 84, pp. 9–25, 2019. DOI: 10.1016/j.mejo.2018.12.010.

[47] B. Ross, "The development of fractional calculus 1695–1900," *Historia Mathematica*, vol. 4, no. 1, pp. 75–89, 1977. DOI: 10.1016/0315-0860(77)90039-8.

[48] S. Darlington, "Realization of a constant phase difference," *The Bell System Technical Journal*, vol. 29, no. 1, pp. 94–104, 1950. DOI: 10.1002/j.1538-7305.1950.tb00934.x.

[49] D. C. Douglas, "A method of designing constant-phase networks," Accessed on 26th June 2021, Master's thesis, Deptt. Electrical Engg., Georgia Institute of Technology, Atlanta, USA, 1961. [Online]. Available: https://smartech.gatech.edu/bitstream/handle/1853/14877/douglas_donald_c_196105_ms_69822.pdf.

[50] R. Morrison, "RC constant-argument driving-point admittances," *IRE Transactions on Circuit Theory*, vol. 6, no. 3, pp. 310–317, 1959. DOI: 10.1109/TCT.1959.1086554.

[51] R. Lerner, "The Design of a Constant-Angle or Power-Law Magnitude Impedance," *IEEE Transactions on Circuit Theory*, vol. 10, no. 1, pp. 98–107, 1963. DOI: 10.1109/TCT.1963.1082094.

[52] G. E. Carlson, "Simulation of the fractional derivative operator $\sqrt{s}$ and the fractional integral operator $1/\sqrt{s}$," Accessed on 26th June 2021, Master's thesis, Dept. Electrical Engineering, Kansas State University, Kansas, USA, 1961. [Online]. Available: https://krex.k-state.edu/dspace/handle/2097/16007.

[53] G. Carlson and C. Halijak, "Approximation of fractional capacitors $(1/s)^{(1/n)}$ by a regular Newton process," *IEEE Transactions on Circuit Theory*, vol. 11, no. 2, pp. 210–213, 1964. DOI: 10.1109/TCT.1964.1082270.

[54] S. C. Dutta Roy and B. Shenoi, "Distributed and lumped rc realization of a constant argument impedance," *Journal of the Franklin Institute*, vol. 282, no. 5, pp. 318–329, 1966. DOI: 10.1016/0016-0032(66)90260-2.

[55] K. B. Oldham, "Semiintegral electroanalysis. analog implementation," *Analytical Chemistry*, vol. 45, no. 1, pp. 39–47, 1973. DOI: 10.1021/ac60323a005.

[56] M. Sugi, Y. Hirano, Y. F. Miura, and K. Saito, "Frequency behavior of self-similar ladder circuits," *Colloids and Surfaces A: Physicochemical and Engineering Aspects*, vol. 198-200, pp. 683–688, 2002. DOI: 10.1016/S0927-7757(01)00988-8.

[57] A. Djouambi, A. Charef, and A. Besançon, "Optimal approximation, simulation and analog realization of the fundamental fractional order transfer function," *International Journal of Applied Mathematics and Computer Science*, vol. 17, no. 4, pp. 455–462, 2008. DOI: 10.2478/v10006-007-0037-9.

[58] D. Sierociuk and A. Dzielinski, "New method of fractional order integrator analog modeling for orders 0.5 and 0.25," in *2011 16th International Conference on Methods Models in Automation Robotics*, 2011, pp. 137–141. DOI: 10.1109/MMAR.2011.6031332.

[59] A. Adhikary, P. Sen, S. Sen, and K. Biswas, "Design and performance study of dynamic fractors in any of the four quadrants," *Circuits, Systems, and Signal Processing*, vol. 35, pp. 1909–1932, 2016. DOI: 10.1007/s00034-015-0213-3.

[60] B. Mandelbrot, *The Fractal geometry of Nature*. Freeman - San Francisco, 1982.

[61] D. Mondal and K. Biswas, "Packaging of single-component fractional order element," *IEEE Transactions on Device and Materials Reliability*, vol. 13, no. 1, pp. 73–80, 2013. DOI: 10.1109/TDMR.2012.2212020.

[62] R. Martin, J. J. Quintana, A. Ramos, and I. de la Nuez, "Modeling electrochemical double layer capacitor, from classical to fractional impedance," in *MELECON 2008 - The 14th IEEE Mediterranean Electrotechnical Conference*, 2008, pp. 61–66. DOI: 10.1109/MELCON.2008.4618411.

[63] A. Dzielinski, G. Sarwas, and D. Sierociuk, "Comparison and validation of integer and fractional order ultracapacitor models," *Adv Differ Equ*, no. 11, 2011. DOI: 10.1186/1687-1847-2011-11.

[64] N. Nafisah, I. Dino, and A. Roselina, "Modelling of ultracapacitor using a fractional-order equivalent circuit," *International Journal of Renewable Energy Technology*, vol. 6, no. 2, pp. 142 –163, 2015. DOI: 10.1504/IJRET.2015.068595.

[65] I. Dimeas, G. Tsirimokou, C. Psychalinos, and A. Elwakil, "Realization of fractional-order capacitor and inductor emulators using current feedback operational amplifiers," in *Proceedings of International Symposium on Nonlinear Theory and its Applications*, 2015, pp. 237–240. [Online]. Available: https://www.ieice.org/nolta/symposium/archive/2015/articles/A4L-B1-6179.pdf.

[66] G. Tsirimokou, C. Psychalinos, and A. Elwakil, "Emulation of a constant phase element using operational transconductance amplifiers," *Analog Integr Circ Sig Process*, vol. 85, pp. 413 –423, 2015. DOI: 10.1007/s10470-015-0626-8.

[67] G. Tsirimokou, C. Psychalinos, and A. Elwakil, *Design of CMOS Analog Integrated Fractional-Order Circuits: Applications in Medicine and Biology*, 1st ed., S. International, Ed., ser. SpringerBriefs in Electrical and Computer Engineering, 2191-8112. 2017.

[68] T. C. Haba, G. Ablart, and T. Camps, "The frequency response of a fractal photolithographic structure," *IEEE Transactions on Dielectrics and Electrical Insulation*, vol. 4, no. 3, pp. 321–326, 1997. DOI: 10.1109/94.598289.

[69] T. Cisse Haba, G. Ablart, T. Camps, and F. Olivie, "Influence of the electrical parameters on the input impedance of a fractal structure realised on silicon," *Chaos, Solitons & Fractals*, vol. 24, no. 2, pp. 479–490, 2005. DOI: 10.1016/j.chaos.2003.12.095.

[70] T. C. Haba, G. L. Loum, and G. Ablart, "An analytical expression for the input impedance of a fractal tree obtained by a microelectronical process and experimental measurements of its non-integral dimension," *Chaos, Solitons & Fractals*, vol. 33, no. 2, pp. 364–373, 2007. DOI: 10.1016/j.chaos.2006.01.123.

[71] I. Jesus and J. Tenreiro Machado, "Development of fractional order capacitors based on electrolyte processes," *Nonlinear Dyn*, vol. 56, pp. 45–55, 2009. DOI: 10.1007/s11071-008-9377-8.

[72] K. Biswas, S. Sen, and P. Dutta, "Realization of a constant phase element and its performance study in a differentiator circuit," *IEEE Transactions on Circuits and Systems II: Express Briefs*, vol. 53, no. 9, pp. 802–806, 2006. DOI: 10.1109/TCSII.2006.879102.

[73] A. M. Elshurafa, M. N. Almadhoun, K. N. Salama, and H. N. Alshareef, "Microscale electrostatic fractional capacitors using reduced graphene oxide percolated polymer composites," *Applied Physics Letters*, vol. 102, no. 23, p. 232 901, 2013. DOI: 10.1063/1.4809817.

[74] A. Buscarino, R. Caponetto, G. Di Pasquale, L. Fortuna, S. Graziani, and A. Pollicino, "Carbon black based capacitive fractional order element towards a new electronic device," *AEU - International Journal of Electronics and Communications*, vol. 84, pp. 307–312, 2018. DOI: 10.1016/j.aeue.2017.12.018.

[75] A. Adhikary, M. Khanra, S. Sen, and K. Biswas, "Realization of a carbon nanotube based electrochemical fractor," in *2015 IEEE International Symposium on Circuits and Systems (ISCAS)*, 2015, pp. 2329–2332. DOI: 10.1109/ISCAS.2015.7169150.

[76] A. Adhikary, "Characterization, packaging and application of a wide CP zone CNT based fractor," *AEU - International Journal of Electronics and Communications*, vol. 127, p. 153 441, 2020, ISSN: 1434-8411. DOI: 10.1016/j.aeue.2020.153441.

[77] A. Agambayev, K. H. Rajab, A. H. Hassan, M. Farhat, H. Bagci, and K. N. Salama, "Towards fractional-order capacitors with broad tunable constant phase angles: Multi-walled carbon nanotube-polymer composite as a case study," *Journal of Physics D: Applied Physics*, vol. 51, no. 6, p. 065 602, 2018. DOI: 10.1088/1361-6463/aaa4de.

[78] D. A. John, S. Banerjee, G. W. Bohannan, and K. Biswas, "Solid-state fractional capacitor using MWCNT-epoxy nanocomposite," *Applied Physics Letters*, vol. 110, no. 16, p. 163 504, 2017. DOI: 10.1063/1.4981204.

[79] K. Biswas, R. Caponetto, G. Di Pasquale, S. Graziani, A. Pollicino, and E. Murgano, "Realization and characterization of carbon black based fractional order element," *Microelectronics Journal*, vol. 82, pp. 22–28, 2018. DOI: 10.1016/j.mejo.2018.10.008.

[80] D. Goldberg, *Genetic Algorithms in Search, Optimization, and Machine Learning*. Addison-Wesley Professional, 1989. DOI: 10.5555/534133.

[81] A. J. Chipperfield, P. J. Fleming, and C. M. Fonseca, "Genetic algorithm tools for control systems engineering," in *Proc. Adaptive Computing in Engineering Design and Control*, 1994, pp. 123 –128. [Online]. Available: https://citeseerx.ist.psu.edu/viewdoc/download?doi=10.1.1.231.8952\&rep=rep1\&type=pdf.

[82] A. Buscarino, R. Caponetto, S. Graziani, and E. Murgano, "Carbon black based fractional order element: An RC$^{\alpha}$ filter implementation," in *2019 18th European Control Conference (ECC)*, 2019, pp. 4118–4121. DOI: 10.23919/ECC.2019.8795635.

[83] R. Caponetto, S. Graziani, and E. Murgano, "Realization of a fractional-order RLC circuit via constant phase element," *Int. J. Dynam. Control*, 2021. DOI: 10.1007/s40435-021-00778-4.

[84] A. Buscarino, R. Caponetto, S. Graziani, and E. Murgano, "Realization of fractional order circuits by a constant phase element," *European Journal of Control*, vol. 54, pp. 64–72, 2020. DOI: 10.1016/j.ejcon.2019.11.009.

[85] R. Garrappa, "Trapezoidal methods for fractional differential equations: Theoretical and computational aspects," *Mathematics and Computers in Simulation*, vol. 110, pp. 96–112, 2015, 7th edition of the workshop "Structural Dynamical Systems: computational aspects. DOI: 10.1016/j.matcom.2013.09.012.

[86] A. G. Radwan, A. S. Elwakil, and A. M. Soliman, "Fractional-order sinusoidal oscillators: Design procedure and practical examples," *IEEE Transactions on Circuits and Systems I: Regular Papers*, vol. 55, no. 7, pp. 2051–2063, 2008. DOI: 10.1109/TCSI.2008.918196.

[87] A. Buscarino, R. Caponetto, E. Murgano, and M. G. Xibilia, "Carbon black based fractional order element: Wien oscillator implementation," in *2019 6th International Conference on Control, Decision and Information Technologies (CoDIT)*, 2019, pp. 205–209. DOI: 10.1109/CoDIT.2019.8820571.

[88] T. Parker and L. Chua, "Chaos: A tutorial for engineers," *Proceedings of the IEEE*, vol. 75, no. 8, pp. 982–1008, 1987. DOI: 10.1109/PROC.1987.13845.

[89] T. Hartley, C. Lorenzo, and H. Killory Qammer, "Chaos in a fractional order Chua's system," *IEEE Transactions on Circuits and Systems I: Fundamental Theory and Applications*, vol. 42, no. 8, pp. 485–490, 1995. DOI: 10.1109/81.404062.

[90] I. Petráš, "Control of fractional-order chua's system," *J Electr Eng*, vol. 53, pp. 219–222, 2002. [Online]. Available: http://iris.elf.stuba.sk/JEEEC/data/pdf/07-08_102-08.pdf.

[91] A. Buscarino, R. Caponetto, L. Fortuna, and E. Murgano, "Chaos in a Fractional Order Duffing System: A circuit implementation," in *2019 IEEE International Conference on Systems, Man and Cybernetics (SMC)*, 2019, pp. 2573–2577. DOI: 10.1109/SMC.2019.8914007.

[92] F. Gómez, J. Rosales, and M. Guía, "RLC electrical circuit of non-integer order," *Central European Journal of Physics*, no. 11, pp. 1361–1365, 2013. DOI: 10.2478/s11534-013-0265-6.

[93] A. Radwan and M. Fouda, "Optimization of fractional-order RLC filters," *Circuits Syst Signal Process*, no. 32, pp. 2097 –2118, 2013. DOI: 10.1007/s00034-013-9580-9.

[94] A. Tepljakov, E. Petlenkov, and J. Belikov, "A flexible MATLAB tool for optimal fractional-order PID controller design subject to specifications," in *Proceedings of the 31st Chinese Control Conference*, 2012, pp. 4698–4703.

[95] A. Phillips, *We can build 4,500 Eiffel Towers with all the e-waste we made last year*, Accessed on 5th July 2021, 2018. [Online]. Available: https://gizmodo.com/global-e-waste-just-grew-8-percent-in-two-years-1821253806.

[96] WEEE Forum, *International e-waste day*, Accessed on 5th July 2021, 2021. [Online]. Available: https://weee-forum.org/iewd-about/.

[97] C. Babbitt and S. Althaf, *Mounting e-waste is harming the planet. Here's how we solve the problem*, Accessed on 5th July 2021, 2021. [Online]. Available: https://www.weforum.org/agenda/2021/01/consumer-electronics-managing-e-waste/.

[98] Press Release, *Apple adds Earth Day donations to trade-in and recycling program*, Accessed on 5th July 2021, 2018. [Online]. Available: https://www.apple.com/newsroom/2018/04/apple-adds-earth-day-donations-to-trade-in-and-recycling-program/.

[99] Samsung, *Sustainability*, Accessed on 5th July 2021. [Online]. Available: https://www.samsung.com/uk/sustainability/environment/resource-efficiency/.

[100] R. M. Brown, "The biosynthesis of cellulose," *Food Hydrocolloids*, vol. 1, no. 5, pp. 345–351, 1987, Special issue: 2nd International Workshop on Plant Polysaccharides. DOI: 10.1016/S0268-005X(87)80024-3.

[101] M. Shoda and Y. Sugano, "Recent advances in bacterial cellulose production," *Biotechnol. Bioprocess Eng.*, vol. 10, no. 1, pp. 261 –270, 2005. DOI: 10.1007/BF02931175.

[102] C. Trigona, S. Graziani, G. Di Pasquale, A. Pollicino, R. Nisi, and A. Licciulli, "Green energy harvester from vibrations based on bacterial cellulose," *Sensors*, vol. 20, no. 1, 2020. DOI: 10.3390/s20010136.

[103] M. Moniri, A. Boroumand Moghaddam, S. Azizi, R. Abdul Rahim, A. Bin Ariff, W. Zuhainis Saad, M. Navaderi, and R. Mohamad, "Production and status of bacterial cellulose in biomedical engineering," *Nanomaterials*, vol. 7, no. 9, 2017. DOI: 10.3390/nano7090257.

[104] M. Iguchi, S. Yamanaka, and A. Budhiono, "Bacterial cellulose—a masterpiece of nature's arts," *Journal of Materials Science*, vol. 35, pp. 261 –270, 2000. DOI: 10.1023/A:1004775229149.

[105] S. Kim, J. Jeon, C. Kee, and I. Oh, "Electro-active hybrid actuators based on freeze-dried bacterial cellulose and pedot:pss," *Smart materials and structures*, vol. 22 (8), no. 8, pp. 1 –9, Jul. 2013. DOI: 10.1088/0964-1726/22/8/085026.

[106] Y. Zheng, J. Yang, W. Zheng, X. Wang, C. Xiang, L. Tang, W. Zhang, S. Chen, and H. Wang, "Synthesis of flexible magnetic nanohybrid based on bacterial cellulose under ultrasonic irradiation," *Materials Science and Engineering: C*, vol. 33, no. 4, pp. 2407–2412, 2013. DOI: 10.1016/j.msec.2013.02.007.

[107] R. Caponetto, G. Di Pasquale, S. Graziani, E. Murgano, and A. Pollicino, "Realization of green fractional order devices by using bacterial cellulose," *AEU - International Journal of Electronics and Communications*, vol. 112, p. 152 927, 2019. DOI: 10.1016/j.aeue.2019.152927.

[108] S. Gea, C. T. Reynolds, N. Roohpour, B. Wirjosentono, N. Soykeabkaew, E. Bilotti, and T. Peijs, "Investigation into the structural, morphological, mechanical and thermal behaviour of bacterial cellulose after a two-step purification process," *Bioresource Technology*, vol. 102, no. 19, pp. 9105–9110, 2011. DOI: 10.1016/j.biortech.2011.04.077.

[109] J. Kim, S. Yun, and Z. Ounaies, "Discovery of cellulose as a smart material," *Macromolecules*, vol. 39, no. 12, pp. 4202–4206, 2006. DOI: 10.1021/ma060261e.

[110] P. Brunetto, L. Fortuna, P. Giannone, S. Graziani, and S. Strazzeri, "Static and dynamic characterization of the temperature and humidity influence on ipmc actuators," *IEEE Transactions on Instrumentation and Measurement*, vol. 59, no. 4, pp. 893–908, 2010. DOI: 10.1109/TIM.2009.2026613.

[111] P. Brunetto, L. Fortuna, P. Giannone, S. Graziani, and S. Strazzeri, "Characterization of the temperature and humidity influence on ionic polymer–metal composites as sensors," *IEEE Transactions on Instrumentation and Measurement*, vol. 60, no. 8, pp. 2951–2959, 2011. DOI: 10.1109/TIM.2011.2118870.

[112] R. Caponetto, G. D. Pasquale, S. Graziani, E. Murgano, A. Pollicino, and C. Trigona, "Green fractional order elements based on bacterial cellulose and ionic liquids," in *2020 IEEE International Instrumentation and Measurement Technology Conference (I2MTC)*, 2020, pp. 1–6. DOI: 10.1109/I2MTC43012.2020.9128828.

[113] R. Caponetto, G. di Pasquale, S. Graziani, E. Murgano, A. Pollicino, and C. Trigona, "Investigation of bacterial cellulose-based fractional order element behaviour," in *2021 IEEE International Instrumentation and Measurement Technology Conference (I2MTC)*, 2021, pp. 1–5. DOI: 10.1109/I2MTC50364.2021.9459985.

[114] R. Caponetto, S. Graziani, E. Murgano, C. Trigona, A. Pollicino, and G. Di Pasquale, "Modeling of a fractional order element based on bacterial cellulose and ionic liquids," *ASME. J. Dyn. Sys., Meas., Control*, vol. 143, no. 7, 2021. DOI: 10.1115/1.4049796.

[115] Alfa Aesar, *1-Ethyl-3-methylimidazolium trifluoromethanesulfonate*, 2021. [Online]. Available: https://www.alfa.com/it/catalog/L19764/.

[116] R. C. Remsing, G. Hernandez, R. P. Swatloski, W. W. Massefski, R. D. Rogers, and G. Moyna, "Solvation of carbohydrates in n,n'-dialkylimidazolium ionic liquids: A multinuclear nmr spectroscopy study," *The Journal of Physical Chemistry B*, vol. 112, no. 35, pp. 11 071–11 078, 2008. DOI: 10.1021/jp8042895.

[117] A. K. Arof, S. Amirudin, S. Z. Yusof, and I. M. Noor, "A method based on impedance spectroscopy to determine transport properties of polymer electrolytes," *Phys. Chem. Chem. Phys.*, vol. 16, pp. 1856–1867, 5 2014. DOI: 10.1039/C3CP53830C.

[118] X. Qian, N. Gu, and Z. e. a. Cheng, "Methods to study the ionic conductivity of polymeric electrolytes using a.c. impedance spectroscopy," *J Solid State Electrochem*, vol. 6, pp. 8–15, 2001. DOI: 10.1007/s100080000190.